Modelling the Air-Side of the Intelligent Building Agents Laboratory

by

Adam Kopach

A thesis submitted in partial fulfilment of the requirements for the degree of

Master of Science
(Mechanical Engineering)

at the

University of Wisconsin – Madison

2021

ABSTRACT

As energy initiatives encourage reductions in the energy usage within the commercial sector, strategies to achieve end-greater use energy reduction in commercial buildings are being tested and implemented. One proposed strategy to accomplish this is through the use of intelligent agents to improve building control strategies. In support of this strategy, the National Institute of Standards and Technology (NIST) built the Intelligent Building Agents Laboratory (IBAL) to study the use of intelligent agents within a controllable environment. To simplify the process of testing new control methods, a simulated model of the air-side of NIST's IBAL was developed. The purpose of this simulation model is to accurately simulate the behavior of the key components that comprise the air-side of the system while having the flexibility to test new control schemes and determine their potential for energy savings. This will allow NIST to explore potential control changes and related analyses in a matter of seconds to determine promising strategies that should be implemented and tested within the physical IBAL.

There are several steps in the development of the IBAL simulation. Firstly, dynamic models for the heating coils and cooling coils within the IBAL were developed. This was done with the inclusion of the storage term within the energy balance, thus allowing for the transient behavior of the components to be captured. These models were then tuned with measured data from the IBAL to reflect the actual performance of their physical IBAL counterparts.

The second step in developing the IBAL model was appropriately characterizing the airflow and static pressure at specific points throughout the air system. This model enforces continuity of airflow and static pressure while determining the pressure rise across Air Handling Unit (AHU) fan and the pressure drop across the dampers throughout the air distribution system. These changes in pressure were initially determined from manufacturer curves. Upon comparison to data, the manufacturer's data alone proved insufficient in capturing the behavior of the IBAL airflow and pressure. Because of this, measured data was collected across both the fan and various dampers in the system to determine the new performance curves based on the IBAL itself. When these updated curves are implemented, the predictive capability of this component will be enhanced.

The third aspect of modelling the IBAL involved the creation of three controllers to compose a baseline automated control system. The first controller was created to actuate the zone VAV damper and generate a reheat signal. The second controller was responsible for adjusting the AHU fan to deliver proper airflow to the zones. The final controller makes changes to the mass flow of coolant through the cooling coil to ensure zone comfort.

The final aspect of simulating the IBAL was to develop a method by which a NIST user can easily utilize and tune models into the future. To achieve this goal and to reduce the likelihood of input errors, a standardized data format was established for component models to be tuned. An additional innovation is the development of an automatic signal generator. When provided a few inputs, this component will generate a signal that selects

relevant data to be used in tuning. Thus, reducing the burden placed on a user to manually select periods of data to be used in tuning.

ACKNOWLEDGEMENTS

There are a multitude of factors and people that made this thesis a possibility and I would like to take a moment to acknowledge a few of the important ones.

First, I would like to thank my advisors Gregory Nellis and Douglas Reindl for pushing me in my work, answering my questions (even the dumb ones) and working with me through a pandemic. I never had a question that went unanswered or ever felt like I was without direction and that is largely due to my amazing advisors.

I would also like to thank David Bradley. Without his help, TRNSYS would have defeated me (and thus this thesis) a long time ago. Thank you for:

- The friendship you provided
- The answers to my many TRNSYS questions
- The hours spent debugging and fixing my models after I failed to utilize your answers

I also want to take a moment to thank Amanda Pertzborn for providing all the measured data of the IBAL and for answering all inquiries about the system.

I want to thank my dad as well for always pushing me to be my best and always being there for me. Your passion for science cultivated the same interest within me that pushed

me to where I am today. I will always admire and strive to follow in your footsteps of constantly learning and innovating. To my four younger sisters, thank you for teaching me patience in all aspects of life. Isaac, thank you for being another boy to grow up with in a house of girls; I think I would've lost my mind without you. Most importantly, thank you for your service in the Navy.

The last person to thank is Megan who pushed me to go to grad school even when I was hesitant. I would not be where I am or who I am without you.

Finally, this research would not have been possible without the grant funded by NIST (NIST Award # 70NANB18H203).

LIST OF FIGURES

TABLE OF CONTENTS

CHAPTER I

Introduction

1.1 Commercial Energy Building Consumption

In the United States, there are four sectors that factor towards the total energy consumption of the country. These sectors are: residential, commercial, industrial, and transportation. Figure 1.1.1 depicts the flow of energy in the US including the total consumption and how it is divided between the four sectors.

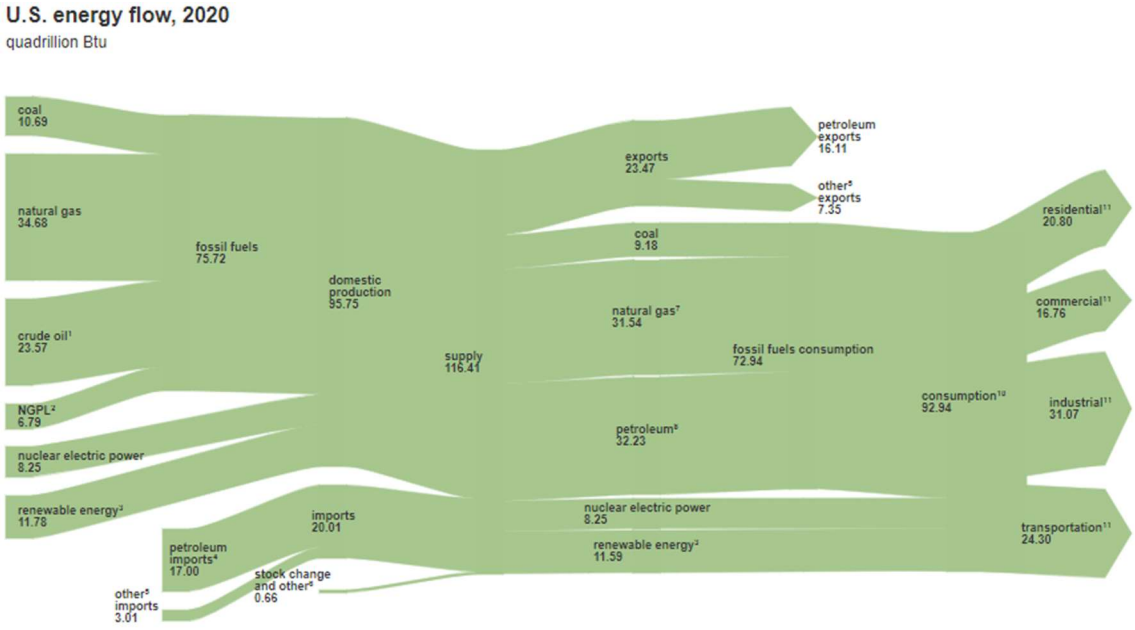

Figure 1. 1. 1: U.S. energy flow from 2020 (EIA, 2020)

According to the most recent statistics, despite having around 4% of the world population, the U.S. energy consumption compared to the total world energy consumption was 17% (EIA, 2020). This yields some perspective on how large the magnitude of U.S. energy consumption is. To reduce usage of primary fuel, regulatory mandates on energy consumption are becoming stricter in the United States, with bills addressing this topic being discussed in congress (GovTrack.us, 2021). To adapt to the

regulations and energy reducing initiatives, there are several sectors that are under renovation through innovation. One of these initiatives involves a transition to net-zero energy commercial buildings. This goal was established by the U.S. Department of Energy (DOE), with the focus of establishing net-zero commercial buildings in all U.S. climate zones by 2025 (NREL, 2009). One of the proposed methods of attaining this goal is through the implementation of intelligent agents.

1.2 Intelligent Agents

The use of intelligent agents is intended to provide a testbed to evaluate control methods that improve upon those currently in use for building heating and cooling systems such as proportional-integral (PI) or proportional-integral-derivative (PID). In general, an intelligent agent "…acquires information about the state of the system, makes an optimal or near-optimal control decision, and communicates that decision to another agent or to an actuator that executes the decision (Pertzborn, 2016)." To examine the feasibility of applying intelligent agents within the scope of heating, ventilating, and air conditioning (HVAC), Kelly and Bushby (2012) performed a study to determine the agents' potential for reducing energy consumption. This proof-of-concept study resulted in a 21% cost savings regarding the test case that was examined. The authors' conclusion consisted of acknowledging the promising results of their study, while stating the need for future studies under both laboratory and real-world scenarios to further validate the use of intelligent agents.

1.3 The Intelligent Building Agents Laboratory

To experimentally verify these promising results, the National Institute of Standards and Technology (NIST) launched the development of the Intelligent Building Agents Laboratory (IBAL). The IBAL contains an air system that is meant to replicate those

typically found in commercial buildings and a hydronic system that allows the system to implement a variety of operating strategies typical of plants found in commercial office buildings. The IBAL can mimic a building having a modern, efficient HVAC system, or a building constrained by an older, more obsolete design. Schematics of the IBAL's air system and the hydronic system are shown in Figure 1.3.1a and Figure 1.3.1b, respectively.

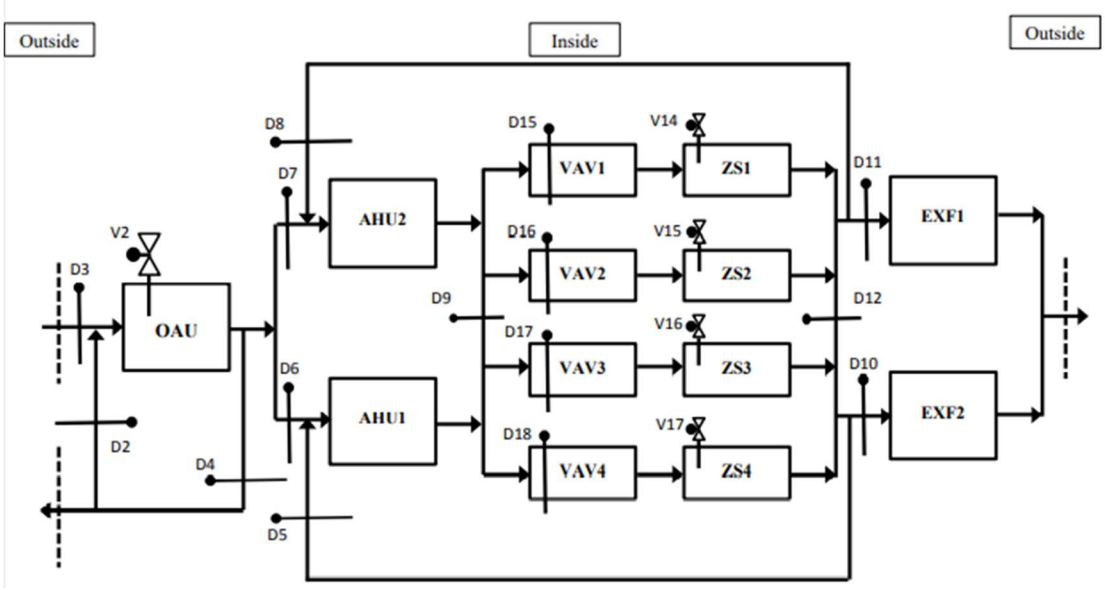

a)

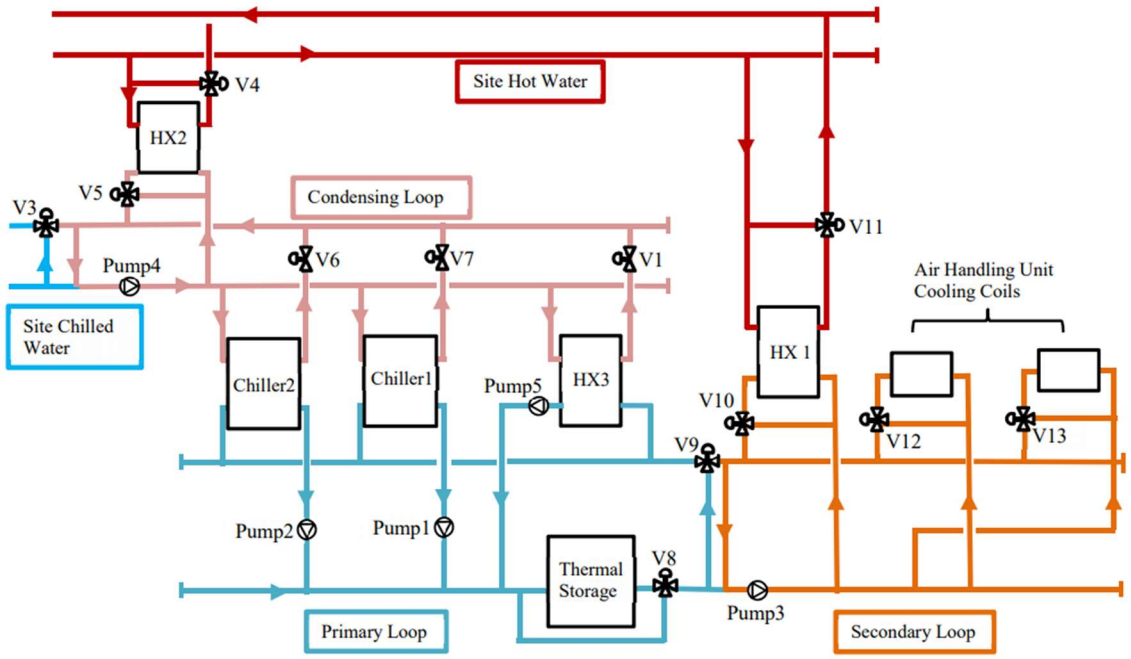

b)

Figure 1. 3. 1: a) Schematic of the IBAL air system (Pertzborn, 2018) b) Schematic of the hydronic system as built (Pertzborn, 2016)

The design and purpose of the air system begins with the intake of outdoor air. At this point, the outdoor air unit (OAU) of the IBAL conditions outside air to simulate any desired combination of temperature and humidity before it passes through the air system.

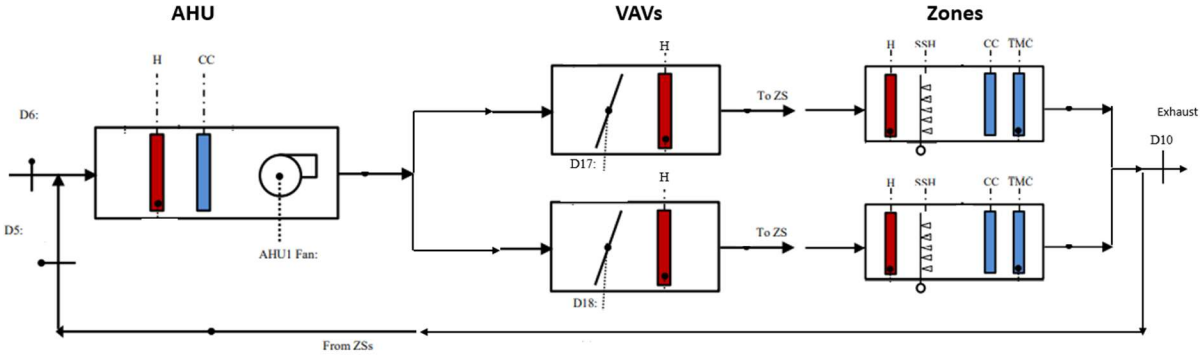

Figure 1. 3. 2: Expanded air system HVAC schematic

Figure 1.3.2 shows a schematic of one of two air handling units (AHUs) within the IBAL along with the two corresponding variable air volume (VAV) boxes and zones connected to the AHU.

1.3.a AHU Design

The inlet conditions to the AHU are the result of mixing that occurs between the "outside" air (AA) that comes from the OAU and the return air (RA) that is recirculated from the zones. There are three functional elements within the AHU of importance. The first conditioning element within the AHU is a pre-heating coil that is used to ensure that the inlet air stream will not freeze the coolant flowing through the cooling coil. This heating coil utilizes 3-phase electric power to sensibly heat the mixed air. The pre-heat coil has a maximum capacity of 9 kW and uses a 0-10 V step controller to modulate the input power to the heating elements to achieve the desired air temperature leaving the pre-heat section. Downstream of the pre-heat coil is the cooling coil which is used to both cool and de-humidify the supply air. The cooling coil is supplied a 30% propylene glycol solution. The glycol supply temperature is adjusted by the chillers while the flow supplied to the coil is adjusted by using a three-way control valve (using a control signal from 0-10 Volts with 0 being fully open and 10 being fully bypassed) as depicted in Figure 1.3.1b. The final component within the AHU is a variable frequency drive (VFD) fan. The fan can operate across a wide range of fan speeds (0 rpm-3600 rpm) via a 0-10 V step controller that modulates the fan speed proportionally, allowing for variable flow rates and pressure rise across the fan. All these components can be seen in the AHU section of figure 1.3.2.

1.3.b VAV Box Design

After going through the AHU, the air passes through two VAV boxes arranged in parallel (one per zone). In the VAV boxes, there are two methods of modifying the air before it is

delivered to the respective zones. The first element encountered is a damper which modulates open and closed to increase and decrease, respectively, the supply air flow rate to each zone. The dampers use a step controller with 0 V resulting in a fully closed damper and 10 V actuating the damper to its fully open position. The other component within each VAV box is the electric reheater. The heaters function to warm the supply air to the zone when the VAV box is at its minimum supply flow and the thermal load in the space decreases; thereby, avoiding overcooling the zone. These heaters have a capacity of 2 kW and are controlled in the same fashion as the preheating component in the AHU.

1.3.c Zone Design

After flowing through the AHU and the VAV boxes, the air is delivered to the zones. The purpose of each zone is to provide a simulated load for the HVAC system to meet. Within each zone, there is a heating coil which is used to simulate sensible cooling loads. This coil is a 5-kW electric heater that is controlled with a step controller. After the electric heater, there is a spray humidifier. This component simulates the latent cooling loads. Next, there is a cooling coil which could be used to provide a heating load. However, the IBAL does not currently use this component as the focus is on designing strategies for cooling loads first. The final component is a thermal mass coil (TMC). These coils add sensible and latent capacitance to the zones by circulating water through the TMC which allows it to conduct heat from the zone and to release it outside the zone. TMCs are used as it better reflects the thermal capacitance that is observed in typical workplace environments.

1.4 Objectives and Research Scope

With the understanding of why the IBAL has been created and what composes it, discussion now turns towards the research that can be done with it. The primary objective of the IBAL is to investigate the use of cutting-edge new control strategies. To help accomplish this, a simulated version of the IBAL has been developed and is described in this thesis. An accurate simulation will allow for testing and implementations of different control strategies in a simple and time efficient manner in a framework that is consistent with the IBAL hardware. The Transient Systems Simulation Program (TRNSYS) is used for this work. This program was selected as it efficiently performs simulations of transient systems. The scope of the modelling within TRNSYS described in this thesis is limited to simulating the effect that the components within the AHUs and VAV boxes have on the system. To accomplish this, models for the components that condition the air were developed and verified against data from the IBAL. This includes models for the heating coils and cooling coils as well as a component to calculate the airflow and pressure throughout the system. In conjunction with these models, several baseline controllers were developed so that the aggregate IBAL model can behave in an autonomous fashion. The controllers are designed so that updated control logic can be implemented easily by a user. This allows for different control strategies to be tested by NIST. An additional benefit of a simulation is that flaws such as air leakage or faulty sensors within the IBAL may be discovered by comparing the results of the model to what the sensors detect using the same inputs.

CHAPTER II

Heating Coil Models

2.1 Introduction

The first step towards modelling the IBAL through TNSYS involves developing and testing heating coil models that replicate the performance of the physical components that are installed in the AHUs and VAV boxes. The standard TRNSYS library contains a built-in library of thermal components including heating coils and cooling coils. A limitation of these standard component models was their application assumed quasi-steady operation. To be functional within the overall model of the IBAL system, it was necessary to incorporate thermal capacitance to properly capture its transient response, including behavior at small time steps.

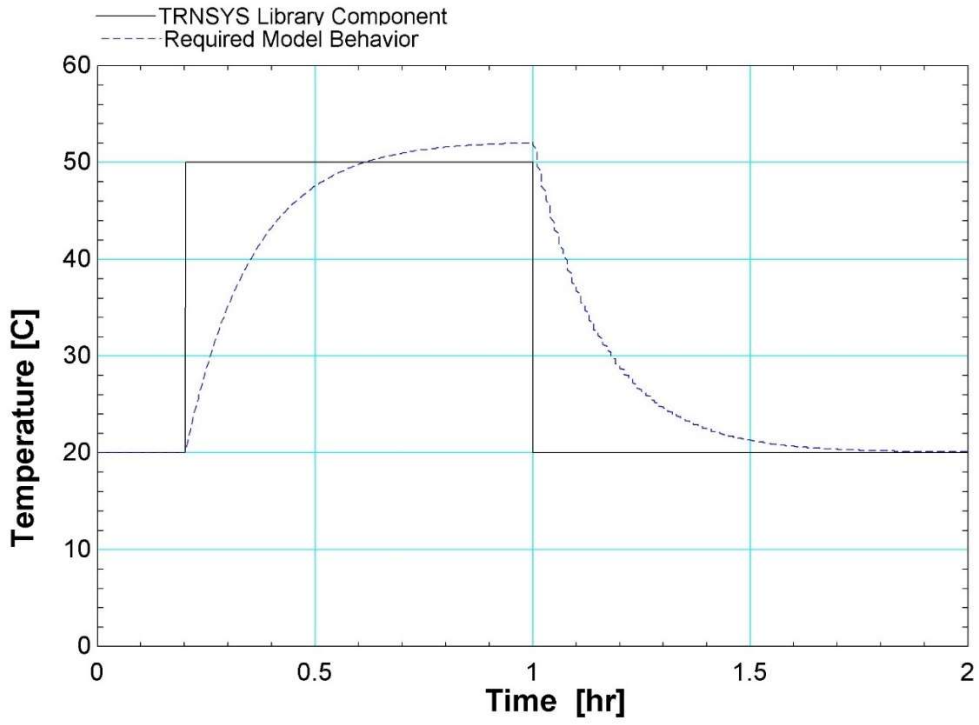

Figure 2. 1. 1: Outlet temperature of a TRNSYS library coil versus the developed coil

To accurately simulate the behavior of the IBAL, the heating coil model must reflect the thermal mass of those within the AHUs and VAV boxes. Figure 2.1.1 shows how the Type 930 heating coil from the TRNSYS library (black line) behaves as a forcing function as it instantly solves for the steady state behavior of the coil. This is directly compared to the type of response that is required of the model (blue line). Noticeably, the TRNSYS model is clearly not sophisticated enough to reflect the transient behavior of the IBAL heating coils. As a result, it was necessary to create a new model within TRNSYS that allowed the transient behavior to be captured.

2.2 Derivation

The method of modelling the heating coils was based on the concept of an effectiveness. Figure 2.2.1 shows the energy balance on the heating coil.

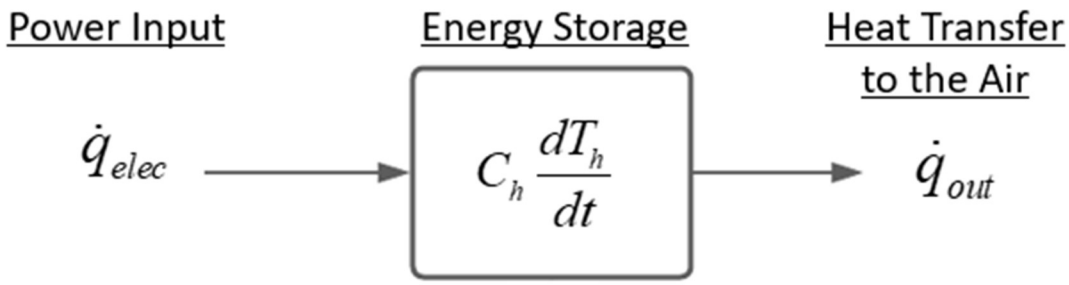

Figure 2. 2. 1: Heating coil energy balance

An unsteady energy balance on the heating coil leads to:

$$C_h \frac{dT_h}{dt} = \dot{q}_{elec} - \dot{q}_{out} \tag{2.2.1}$$

where C_h is the thermal capacitance of the electric heater, T_h is the average temperature of the heater, and $\dot{q}_{elec}$ is the electric power supplied to the heater. Finally, $\dot{q}_{out}$ is the heat transfer to the air. The heat transfer rate to the air is equal to the maximum possible heat

transfer rate (which occurs when the air leaves at the heater temperature) multiplied by the effectiveness:

$$\dot{q}_{out} = \varepsilon\ \dot{m}\ c\ \left(T_h - T_{in}\right) \tag{2.2.2}$$

where $\dot{m}$ is the mass flow of the air, c is the specific heat of the air, and T_{in} is the inlet air temperature. The effectiveness is obtained using the solution for a heat exchanger with an infinite capacitance ratio:

$$\varepsilon = 1 - e^{\left(-\frac{UA}{\dot{m}\ c}\right)} \tag{2.2.3}$$

where UA is the conductance of the heater. Substituting equation (2.2.2) into equation (2.2.1) leads to:

$$\frac{dT_h}{dt} = \frac{\dot{q}_{elec} - \varepsilon\ \dot{m}\ c\ \left(T_h - T_{in}\right)}{C_h} \tag{2.2.4}$$

To use the differential equation solver within TRNSYS, the differential equation must be expressed in the form:

$$\frac{dT_h}{dt} = aT_h + b \tag{2.2.5}$$

where a and b are both constants. Equation (2.2.4) is placed in this form:

$$\frac{dT_h}{dt} = \left(-\frac{\varepsilon\ \dot{m}\ c}{C_h}\right)\ T_h + \left(\frac{\varepsilon\ \dot{m}\ c\ T_{in} + \dot{q}_{elec}}{C_h}\right) \tag{2.2.6}$$

so that $a = -\dfrac{\varepsilon\ \dot{m}\ c}{C_h}$ and $b = \dfrac{\varepsilon\ \dot{m}\ c\ T_{in} + \dot{q}_{elec}}{C_h}$

The differential equation solver function within TRNSYS then solves for T_h as a function of time within any time step. The air outlet temperature is obtained according to:

$$T_{out} = T_{in} + \varepsilon\left(T_h - T_{in}\right) \tag{2.2.7}$$

2.3 TRNSYS Interface

With the derivation of the heating coil model complete, it is important to understand how the model is implemented into TRNSYS so that the parameters used for tuning can be established.

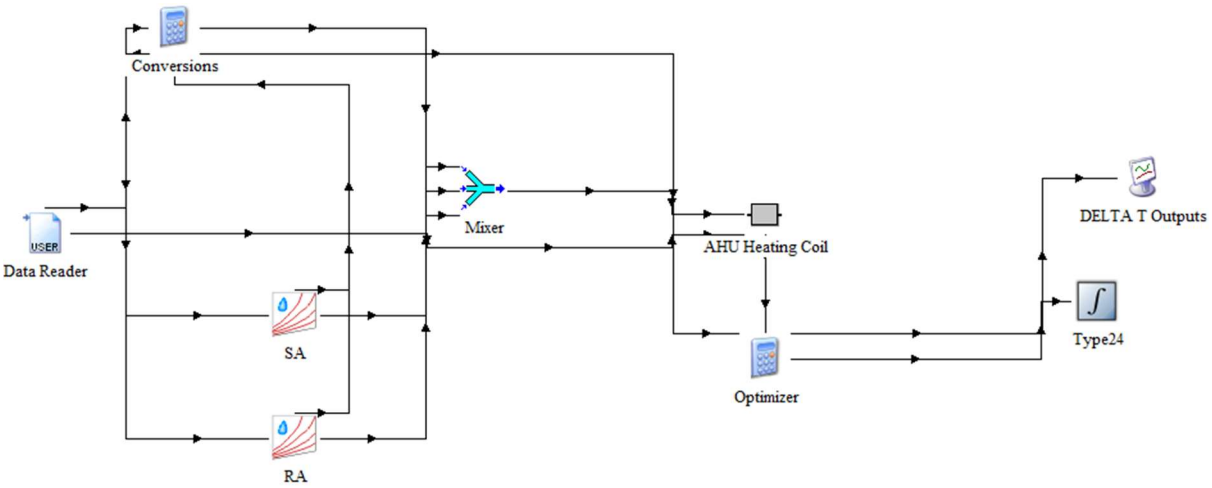

Figure 2. 3. 1:Schematic of AHU heating coil optimization

Figure 2.3.1 shows an example of how TRNSYS projects are created and linked. Additionally, there are arrows that go into and come out of the AHU Heating Coil. These arrows indicate inputs and outputs related to the heating coil, respectively. If a user selects the coil from the project (double-click), a menu will pop up with 3 tabs of importance as shown in Figure 2.3.2a-c.

Parameter | Input | Output | Derivative | Comment

		Name	Value	Unit	More	Macro
1		Heater Capacitance	Capacitance	variable name	More...	☑
2		UA	heat_transfer_coeff	variable name	More...	☑
3		air specific heat	1	kJ/kg	More...	☑

a)

Parameter | Input | Output | Derivative | Comment

		Name	Value	Unit	More	Macro
1		Inlet air mass flow rate	0	kg/hr	More...	☑
2		Inlet air temperature	0	C	More...	☑
3		Inlet air relative humidity	0	-	More...	☑
4		Heater Power	0	W	More...	☑
5		Pressure	1	atm	More...	☑

b)

Parameter | Input | Output | Derivative | Comment

		Name	Unit	More	Macro	Print
1		Outlet Air flow	kg/hr	More...	☑	☐
2		Outlet Air Temperature	C	More...	☑	☐
3		Heater Temperature	C	More...	☑	☐
4		Volumetric Flow	cfm	More...	☑	☐
5		Outlet Relative Humidity	-	More...	☑	☐

c)

Figure 2. 3. 2: a) Electric heater parameters b) Electric heater inputs c) Electric heater outputs

Figure 2.3.2a depicts the *parameters* associated with the electric heater model. This is the tab where a user would change the characteristics of the model by adjusting the capacitance and/or the overall conductance. The adjustment of these parameters is what allows the model to be tuned to simulate different heater models/sizes. Figure 2.3.2b lists the inputs that are used by the model, including inlet air conditions and the inlet power. The inputs for this model are typically read from data or come from the outputs of upstream component. However, if the text of the input is blue, that indicates no direct input from either the data reader or an upstream component. In those situations, the model uses the number located in the corresponding row of the 'Value' column. A user may set this default value before simulation, or can connect a data input to be read in. In this scenario, the pressure of the air for psychrometric purposes is not included in the data

and thus a user determined value was used by the model. By default, this value is set to atmospheric pressure but can be adjusted by a user, as necessary. Figure 2.3.2c displays the outputs of the heating coil. The outlet airflow and relative humidity are the most important in addition to the outlet air temperature. These allow for full definition of psychometrics and maintains continuity of mass to components that will use the heater model outputs as inputs. The units of conductance and air flow rate are on an hourly rate as TRNSYS operates using a time step on an hourly basis. In the case of the IBAL, data is sampled every ten seconds which is implemented into TRNSYS as a fraction of an hour by:

$$\tau = (10\ \text{s}) \Big/ \left(3600\ \frac{\text{s}}{\text{hr}} \right) \tag{2.3.1}$$

2.4 Heating Coil Tuning

2.4.a TRNOPT Overview

The TRNSYS optimization routine, TRNOPT, is used for tuning parameters for a given component which allows TRNSYS to calibrate component model parameters to match experimental data. To operate TRNOPT, an error term is defined and integrated over time to obtain an average error. This error is typically defined as the difference between the measured data and the simulated result. The user then prescribes the parameters that TRNOPT can adjust or tune as it attempts to reduce the overall error throughout the entirety of the data set being tested. Further description of how to operate TRNOPT is detailed in chapter VI.

2.4.b Air Handling Unit Heating Coil Tuning

In the case of the heating coils, the two parameters used for tuning include C_h and *UA*. To tune the AHU heating coil model, a wide range of data was collected by NIST (Pertzborn, 2021). This data included the heating coil response to varying airflow rates and heating power inputs.

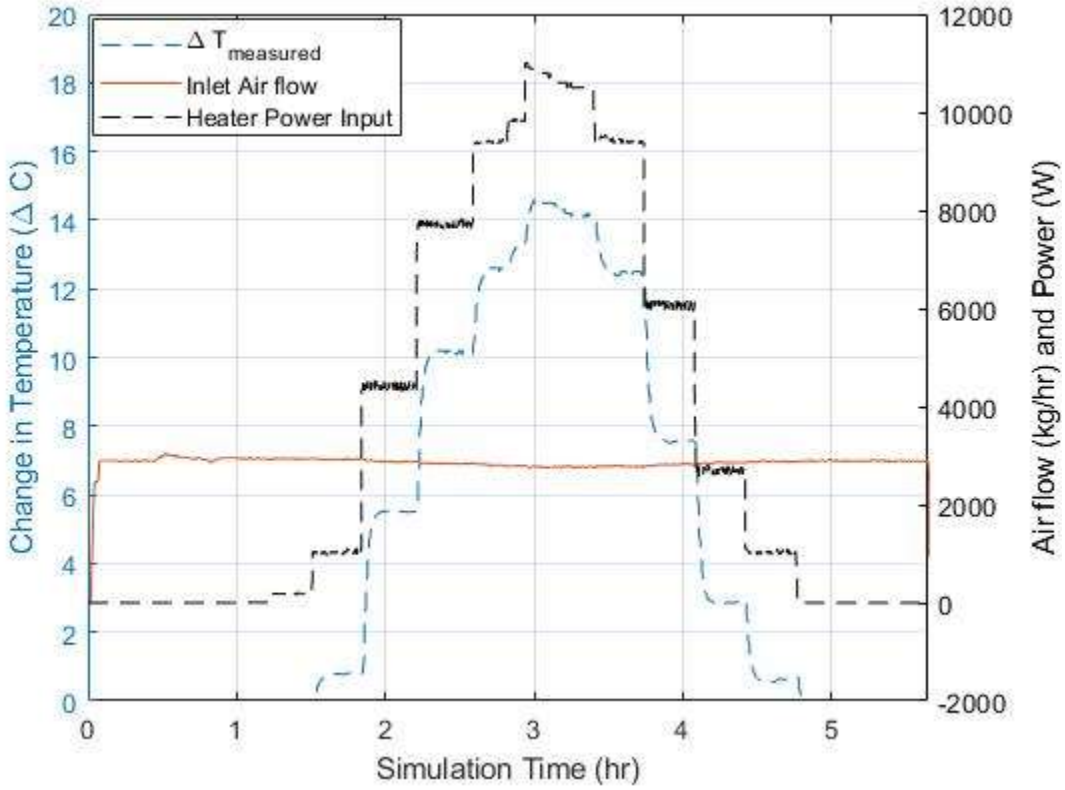

Figure 2. 4. 1: Example of test used to tune the AHU heating coil

Figure 2.4.1 gives an example of the measured inputs that include airflow and power to the AHU heating coil within the IBAL and the corresponding measured air-side temperature rise. These data are used to tune the TRNSYS model to accurately predict transient response of the heating coil. This figure shows that whenever an input is adjusted, the IBAL heating coil enters a transient state that eventually reaches a steady state condition. Overall, 4 tests were used to tune the TRNSYS model, with

approximately 2,000 data points per test. These tests contain the measured heating coil response to both constant flow and varying heater power, along with the converse scenario. This was done to tune the model across a wide spectrum of airflow and heater power combinations, ensuring that it works across large span of inputs. The complete description of each test used in the AHU heater tuning is in Appendix A1.

TRNOPT was used in conjunction with these data sets to determine the best set of values for C_h and UA. This was accomplished by reducing the error defined as:

$$e_{HC} = \left(\Delta T_{measured} - \Delta T_{sim}\right)^2 \tag{2.4.1}$$

This resulted in values of 20 kJ/K and 1100 kJ/hr-K, respectively. Figure 2.4.2 updates provides an update from Figure 2.4.1 to show how the model performs relative to the data at these parameters across the varying inputs.

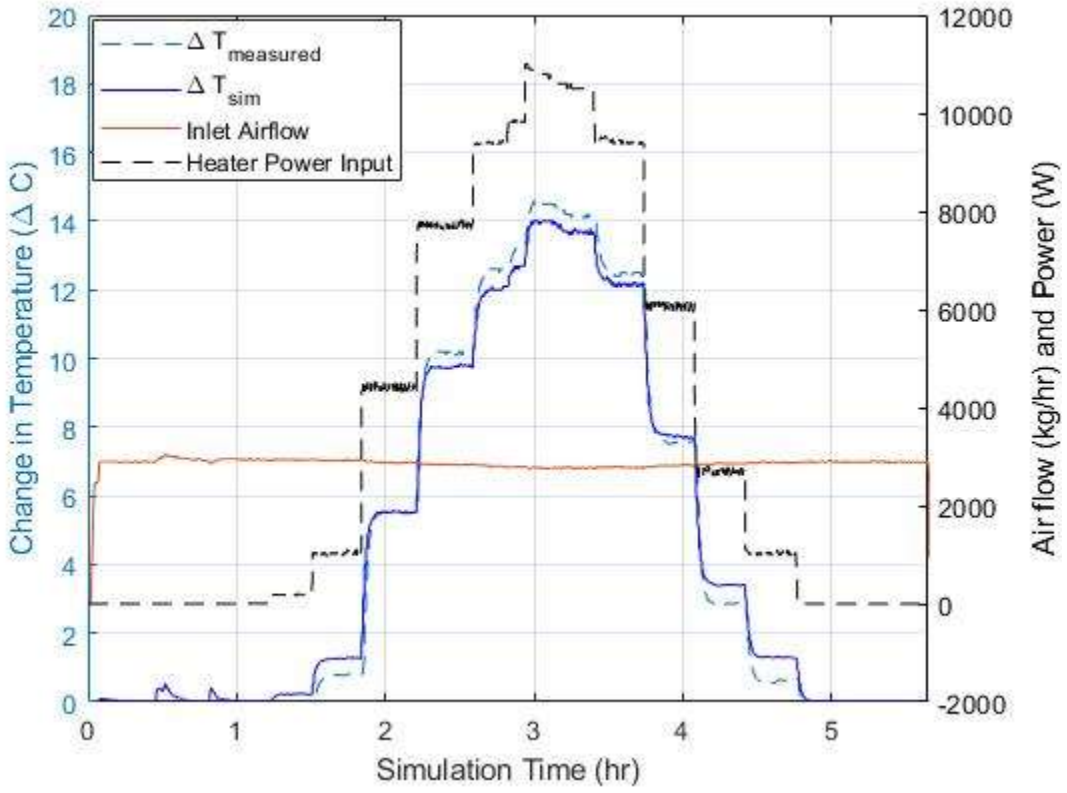

Figure 2. 4. 2: AHU heater test case results

Notably, the transient behavior is captured throughout this test and the steady state temperature rise between the measured data and the model is the same to within about 0.5°C in most periods.

The results of air temperature rise predicted by the tuned model and the actual measured air temperature rise for the totality of all measured data are shown in Figure 2.4.3.

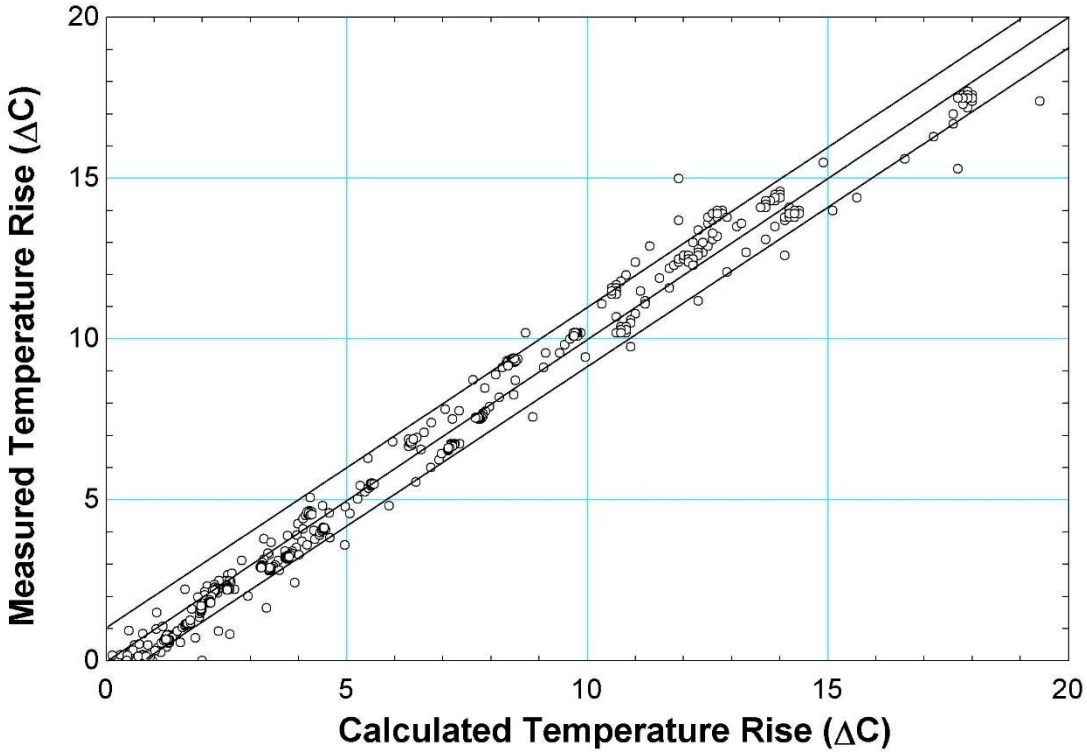

Figure 2. 4. 3: Compiled AHU Heater Data Compared to Simulated Model Output

Overall, the results indicate that the model can predict the behavior of the coil to within approximately 1°C under most conditions. This holds true for 95% of the measured data tested with the model. While these results are within an acceptable range, a couple potential solutions that may be explored in the future to increase the accuracy of this model. One possible solution involves adapting *UA* so that it is a function of heater power. The other possible improvement involves the development of a heat loss term to be included in the model.

As a final step towards validating this coil model, the average energy balance from every steady state period of data for the AHU1 heating coil was created. The uncertainty of the IBAL measurements are included in this energy balance and is depicted in Figure 2.4.4

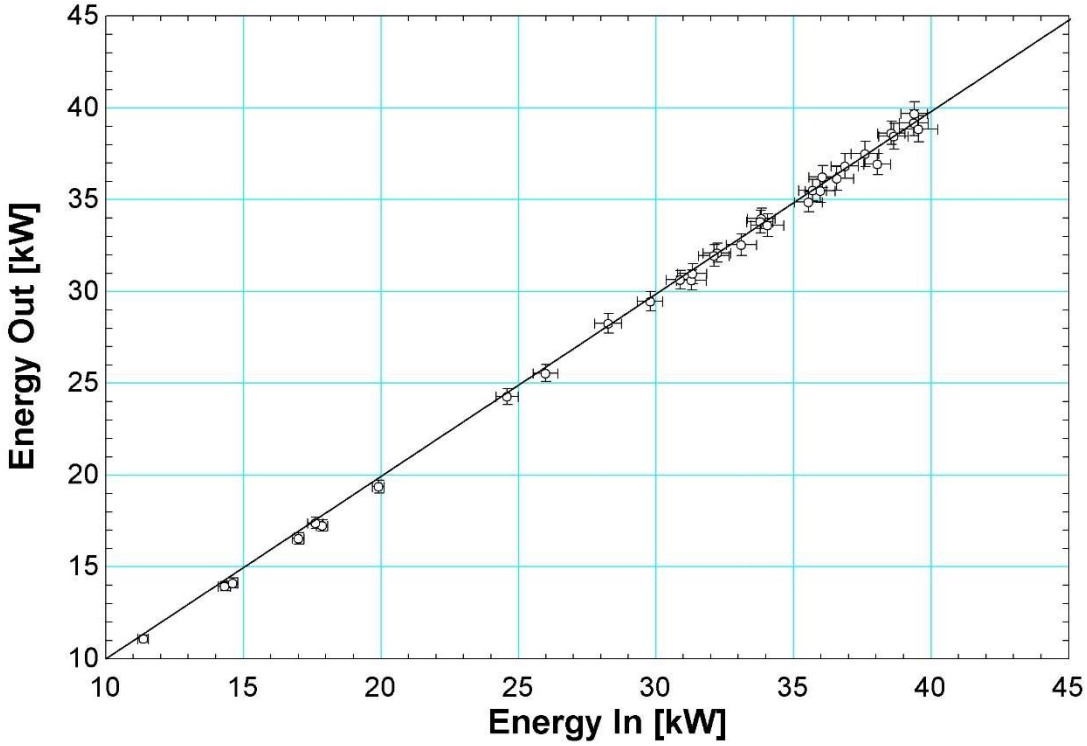

Figure 2. 4. 4: AHU1 steady state energy balance with measurement uncertainty

Figure 2.4.4 shows how the measured data balances energy very well across the steady state periods. Most of the measured energy imbalances are to a small enough degree that sensor uncertainty explains them. Thus, the outlier temperatures shown in Figure 3.4.3 are likely representative of the variation that can occur when complete data sets are used rather than averaged data which would smooth out some of the outlying data that is measured.

2.4.c Variable Air Volume Box Heating Coil Tuning

The VAV heating coil tuning was performed in the same manner as the AHU coil. Since the VAV coil is smaller relative to the AHU coil, it is expected that the values of C_h and

UA will be smaller as well. For this coil, only one test was performed which consisted of 3,500 data points. The inlet conditions for the test are shown in Figure 2.4.5. A wide range of power and airflow combinations are used to accumulate a rich set of data to tune the model.

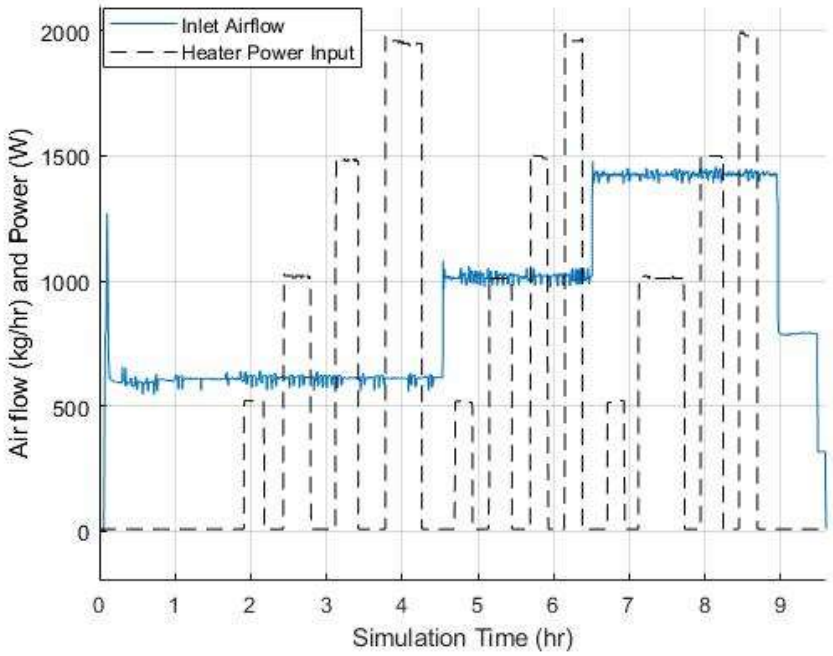

Figure 2. 4. 5: VAV heater test inputs

After running this test through TRNOPT, the values of C_h and *UA* were determined to be 1.2875 kJ/K and 48.125 kJ/hr-K, respectively.

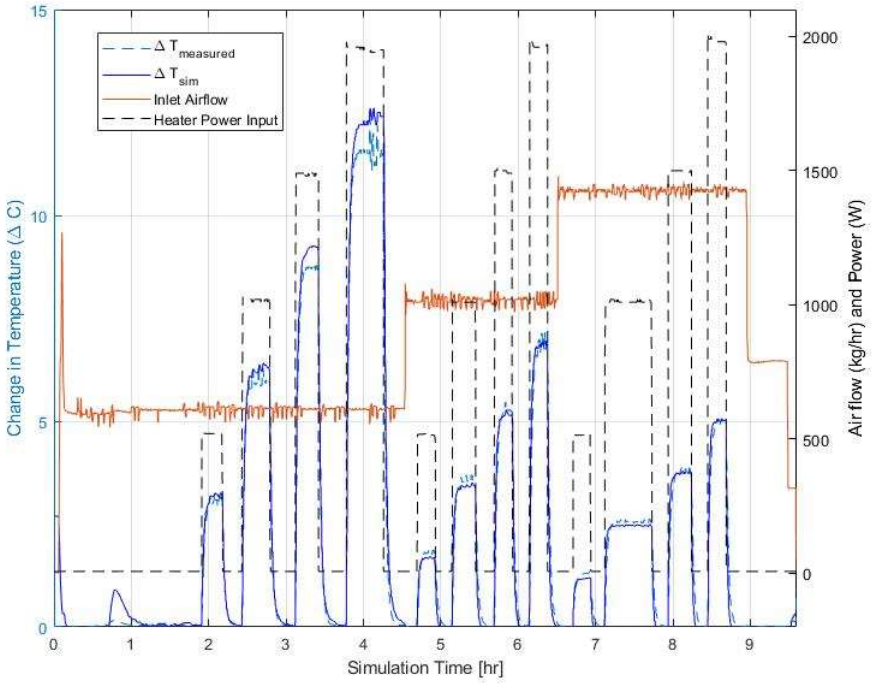

Figure 2. 4. 6: VAV heater test results

Figure 2.4.6 shows the response of the model compared to the measured data at the parameters as determined by the TRNOPT. The result of this test is consistent with the behavior that was noticed in the AHU tuning; the measured temperature rise was within a 1°C margin in comparison to the IBAL data for the VAV heater. At the combination of larger heater powers (1000-2000 W) and smaller airflow (600 kg/hr), the model deviates towards the 1°C differential. However, throughout the other combinations of power and airflow, the VAV model operates within a 0.2°C accuracy compared to the measured data.

2.5 Summary

Overall, the heating coil derivation shows how the model adds thermal capacitance to capture the transient behavior of the coils used in the IBAL by performing an energy balance with the inclusion of an energy storage term. To tune the transient heating coil model, measured data were collected for both the AHU and VAV coils. These data were

utilized by TRNOPT to determine the combination of values for C_h and UA that minimize the error between the predicted air temperature rise from transient model and actual air temperature rise from measured data recorded by the IBAL instruments. After tuning, both the AHU and the VAV models matched the performance of their IBAL counterparts to a 1°C level of accuracy.

CHAPTER III

Cooling Coil Model

3.1 Introduction

The next step in preparing a system simulation model for the IBAL is to develop a cooling coil model that accurately simulates the behavior of both the air-side and coolant-side. Like the heating coil model, a base cooling coil model is available in TRNSYS (Type 508) and this model assumes quasi-steady state behavior as shown in Figure 3.1.1. To adapt Type 508 for use in modeling the IBAL, modifications are required to enable its use for predicting transient behavior. The main modification will be to incorporate thermal capacitance by utilizing an energy storage term within the model.

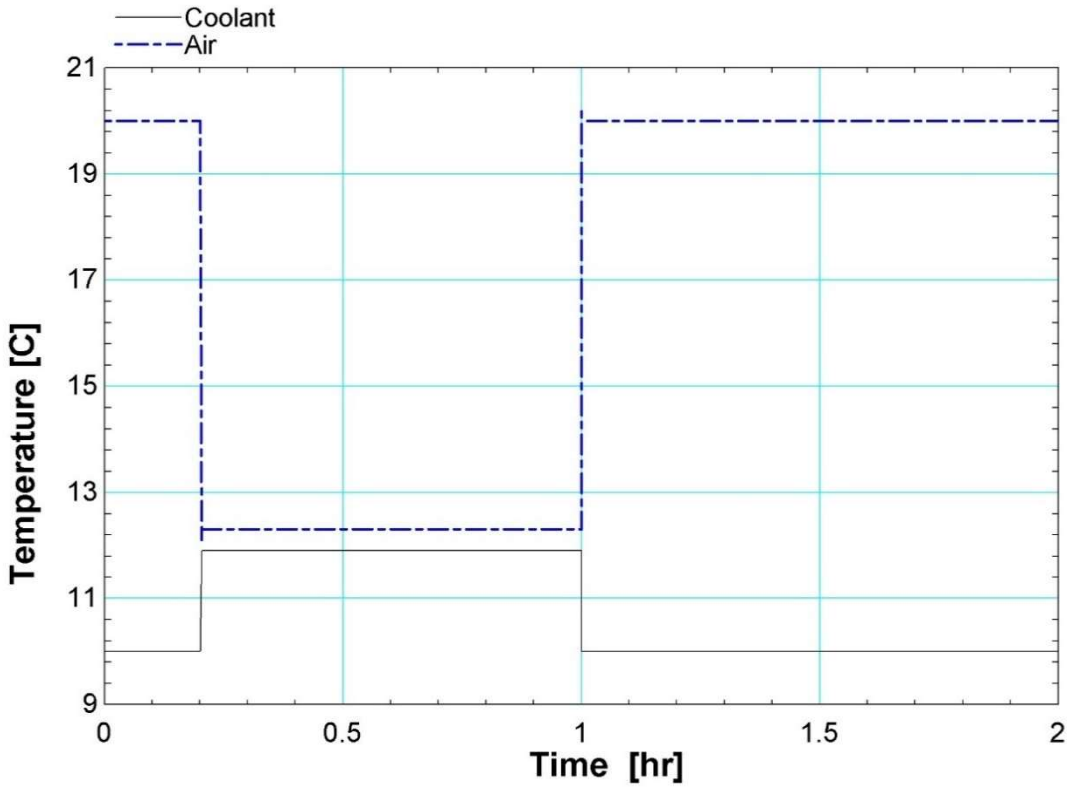

Figure 3. 1. 1: Outlet temperatures of coolant and air for TRNSYS library cooling coil

3.2 Derivation

Figure 3.2.1 shows a schematic of a "bypass model" (Stanke, 2000) that provides a framework for simulating the cooling coil.

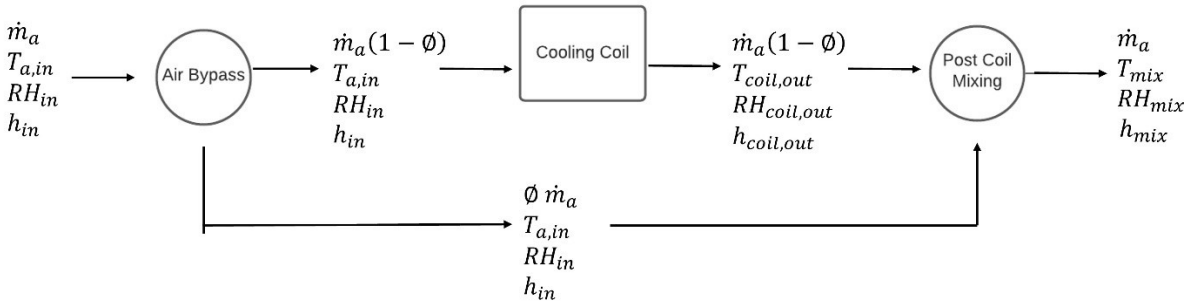

Figure 3. 2. 1: Schematic of the air-side of the Cooling Coil bypass model

Conceptually, the bypass model assumes some fraction of the total air flow will pass through the cooling coil (face) and leave saturated at the coil temperature ($T_{coil,out} = T_C$) while the balance of air flows around the coil without a reduction in temperature or moisture content (bypass). The coil temperature is determined by solving an unsteady energy balance on the coil. The two streams, face and bypass, mix downstream yielding a mixed air condition that mimics the actual cooling coil's leaving air temperature and moisture content.

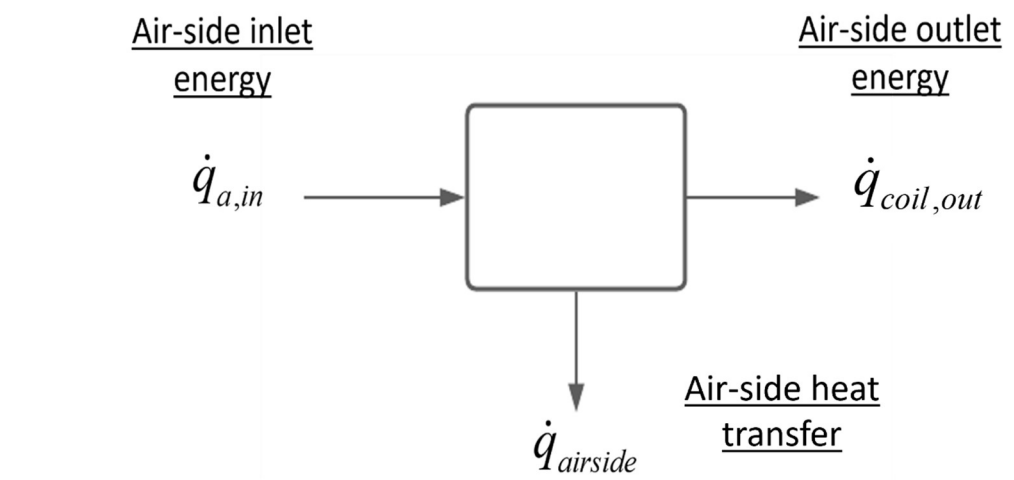

a)

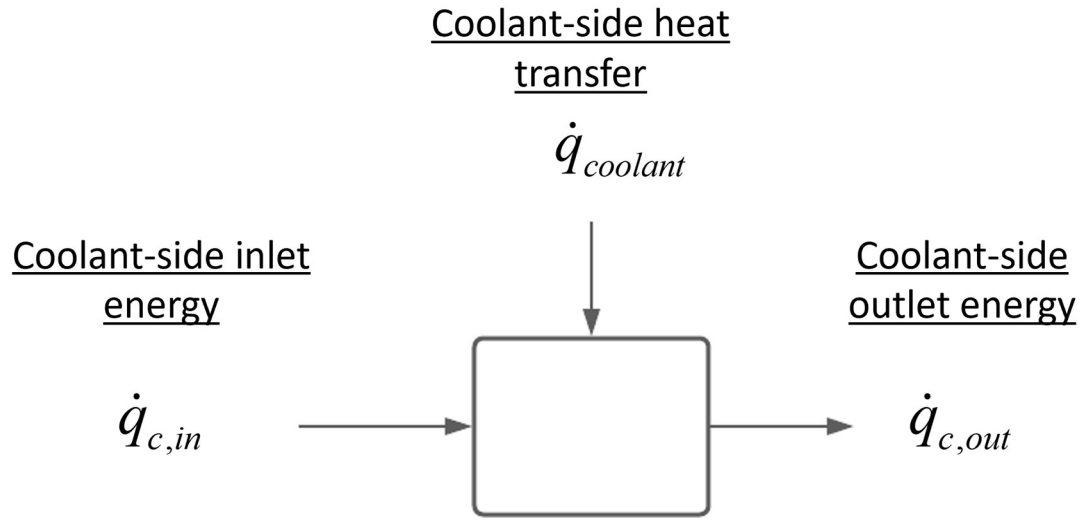

b)

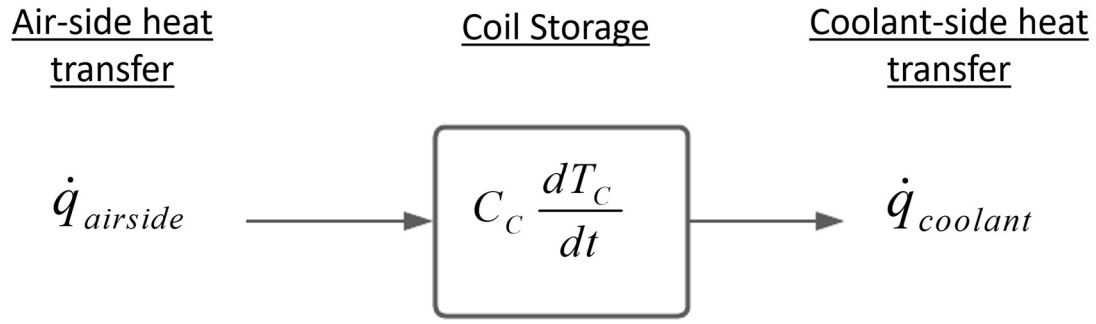

c)

Figure 3. 2. 2: a) Energy balance on the air-side b) Energy balance on the coolant-side c) Cooling coil energy balance

Figure 3.2.2a depicts the air-side energy balance that is expressed as:

$$\dot{q}_{airside} = \dot{q}_{a,in} - \dot{q}_{coil,out} \tag{3.2.1}$$

where $\dot{q}_{a,in}$ is the energy of the inlet airstream as determined by the inlet enthalpy and the mass flow rate of air that interacts with the coil and $\dot{q}_{coil,out}$ is the energy of the air immediately after interacting with the coil as determined by the outlet enthalpy of the air. Substituting the definitions for these terms and simplifying, the air-side energy balance is re-written as:

$$\dot{q}_{airside} = \dot{m}_a \left(1-\phi\right)\left(h_{in} - h_{coil,out}\right) \tag{3.2.2}$$

where $\dot{m}_a \left(1-\phi\right)$ is the mass flow of air that goes through the coil determined by the enthalpy-based bypass factor , h_{in} is the inlet enthalpy of the air as determined by $T_{a,in}$ and RH_{in} , and $h_{coil,out}$ is the enthalpy of the air saturated at the coil temperature.

The coolant-side of the coil energy balance is presented in Figure 3.2.2b. This energy balance is expressed by:

$$\dot{q}_{coolant} = \dot{q}_{c,out} - \dot{q}_{c,in} \tag{3.2.3}$$

where $\dot{q}_{c,out}$ is the energy associated with the coolant leaving the coil as determined by its outlet temperature and $\dot{q}_{c,in}$ is the energy of the coolant entering the coil as determined by the inlet coolant temperature. Substituting these definitions into equation (3.2.3) yields:

$$\dot{q}_{coolant} = \dot{m}_{liquid}\ c_{liquid}\ \left(T_{liquid,out} - T_{liquid,in}\right) \tag{3.2.4}$$

where $\dot{m}_{liquid}$ is the mass flow of the coolant, c_{liquid} is the specific heat of the coolant, $T_{liquid,in}$ is the inlet temperature of the coolant, and $T_{liquid,out}$ is the outlet temperature. Figure 3.2.2c includes the thermal mass associated with the cooling coil itself as well as the coupling of the air-side and coolant-side across the cooling coil. This unsteady energy balance becomes:

$$C_C \frac{dT_C}{dt} = \dot{q}_{airside} - \dot{q}_{coolant} \tag{3.2.5}$$

where C_C is the capacitance of the cooling coil. Substituting Equation (3.2.2) and Equation (3.2.4) into Equation (3.2.5) gives:

$$C_C \frac{dT_C}{dt} = \dot{m}_a (1-\phi)\left(h_{a,in} - h_{coil,out}\right) - \dot{m}_{liquid}\ c_{liquid}\ \left(T_{liquid,out} - T_{liquid,in}\right) \tag{3.2.6}$$

In this equation, it is necessary to solve for T_C as this value impacts both $h_{coil,out}$ and $T_{liquid,out}$. The determination of the value of $h_{coil,out}$ depends on whether the coil temperature is above or below the dew point temperature (i.e., whether condensation occurs or not). If the dewpoint temperature of the air entering cooling coil is greater than the coil temperature, then no condensation will occur. The following inequality provides a corresponding quantitative test:

$$T_C > T_{dp,in} \tag{3.2.7}$$

where $T_{dp,in}$ is the dewpoint temperature of the air entering the cooling coil. In this scenario, $h_{coil,out}$ is determined by using psychometric functions with the outlet state defined by T_C and $\omega_{a,in}$ (inlet humidity ratio). If the coil temperature is equal to or less than the entering air dew point temperature, condensation of moisture from the air will

occur on the coil surfaces and $h_{coil,out}$ is defined by T_C and a saturated relative humidity ($RH_{coil,out}=1$).

To solve for $T_{liquid,out}$ an effectiveness is used:

$$T_{liquid,out} = T_{liquid,in} + \varepsilon_{coolant} \left(T_C - T_{liquid,in}\right) \tag{3.2.8}$$

with the effectiveness ($\varepsilon_{coolant}$) is calculated according to:

$$\varepsilon_{coolant} = 1 - e^{\left(-\frac{UA_{coolant}}{\dot{m}_{liquid}\ c_{liquid}}\right)} \tag{3.2.9}$$

where $UA_{coolant}$ is the overall conductance of the coolant.

To solve the differential equation presented by Equation (3.2.6), the TRNSYS model uses an iterative Euler integration:

$$T_{C,new} = T_C + (1/n)\ \tau \left(\frac{\dot{q}_{airside} - \dot{q}_{coolant}}{C_C}\right) \tag{3.2.10}$$

where $T_{C,new}$ is the new coil temperature and n is the user-defined number of sub-timesteps used in the Euler integration.

After solving for $T_{C,new}$, the model then successively substitutes and utilizes the new coil temperature in Eqs. (3.2.6)-(3.2.10) to find the convergent value for T_C which ensures that all the outlet states have converged as well.

The last step for the model is to mix the bypass air with the portion of air (face) that is assumed to closely contact the coil. This is done by calculating the mixed air enthalpy:

$$h_{mix} = \phi\ h_{a,in} + (1-\phi)\ h_{coil,out} \tag{3.2.11}$$

and the mixed air humidity ratio:

$$\omega_{mix} = \phi\ \omega_{a,in} + (1-\phi)\ \omega_{coil,out} \tag{3.2.12}$$

Using the psychrometric tables, the program then determines the outlet air temperature (T_{mix}) at h_{mix} and ω_{mix}.

3.3 TRNSYS Interface

With the derivation of the cooling coil model complete, the next step is to look at the parameters, inputs, and outputs for the model and how they appear within the TRNSYS UI.

Parameter | Input | Output | Derivative | Comment

		Name	Value	Unit	More	Macro
1		Humidity mode	**1**	-	More...	☑
2		Number of sub timesteps	1000	-	More...	☑
3		Coil capacitance	**C**	**variable name**	More...	☑
4		Liquid specific heat	**3.83**	kJ/kg.K	More...	☑
5		Coil overall heat transfer coefficient	**CHT**	**variable name**	More...	☑
6		Coil Bypass Fraction	**bypass**	**variable name**	More...	☑
7		Low airflow UA	**5000**	kJ/hr.K	More...	☑
8		Low coolant flow UA	**14000**	kJ/hr.K	More...	☑

a)

Parameter | Input | Output | Derivative | Comment

		Name	Value	Unit	More	Macro
1		Inlet liquid temperature	6.67	C	More...	☑
2		Inlet liquid flow rate	0	kg/hr	More...	☑
3		Inlet air temperature	26	C	More...	☑
4		Inlet air humidity ratio	0.005	-	More...	☑
5		Inlet air relative humidity	50.	% (base 100)	More...	☑
6		Inlet air mass flow rate	0	kg/hr	More...	☑
7		Inlet air pressure	1	atm	More...	☑
8		Air side pressure drop	0	atm	More...	☑

b)

Parameter | Input | Output | Derivative | Comment

		Name	Unit	More	Macro
1		Outlet liquid temperature	C	More...	☑
2		Outlet liquid flow rate	kg/hr	More...	☑
3		Outlet air temperature	C	More...	☑
4		Outlet air humidity ratio	-	More...	☑
5		Outlet air relative humidity	% (base 100)	More...	☑
6		Outlet air mass flow rate	kg/hr	More...	☑
7		Outlet air pressure	atm	More...	☑
8		Coil temperature	C	More...	☑
9		Total air side energy transfer	kJ/hr	More...	☑
10		Sensible air side energy transfer	kJ/hr	More...	☑
11		Latent air side energy transfer	kJ/hr	More...	☑
12		Liquid side energy transfer	kJ/hr	More...	☑
13		Energy balance	% (base 100)	More...	☑

c)

Figure 3. 3. 1: a) Cooling coil parameters b) Cooling coil inputs c) Cooling coil outputs

Figure 3.3.1a shows the parameters of the cooling coil model. The humidity mode parameter will always either be '1' or '2'. The model must choose between using the absolute humidity input or the relative humidity input for psychrometric calculations. '1' corresponds with using absolute humidity while '2' corresponds with relative humidity. This allows for a user to specify which humidity input is being used. Typically, mode 2 will be used since relative humidity is an output of the heating coil model. An additional parameter is the number of sub-timesteps for Euler integration. Rather than calculating the critical timestep for the Euler integration, the parameter is set to an exceptionally large number (1000) to ensure the sub-timesteps are extremely small relative to what the model samples at. When looking at the speed of the model at this number of sub-timesteps, TRNSYS only spends 1% of the simulation time within the cooling coil

component. If TRNSYS spends significant time within the cooling coil component in future tests and projects, a method of calculating the critical timestep within the cooling coil component may be implemented.

A constant specific heat is assumed for the coolant. Between 0 °C and 20°C the solutions specific heat varies from 3.803 kJ/kg-K to 3.857 kJ/kg-K, respectively. Because the variation of specific heat is of a small magnitude, assuming a specific heat at an average value will not lead to significant degradation of the cooling coil model's predictive capability. The propylene-glycol specific heat table generated through EES (Klein, 2020) is in Appendix B.

The last three parameters that will be discussed in this section are the tunable parameters of the cooling coil including coil capacitance, conductance, and the bypass fraction. These parameters are determined within TRNOPT to minimize the error between the model and the measured data. Parameters 7-8 are UA parameters to be used in certain low-flow scenarios and will be discussed further in this chapter. Figure 3.3.1b depicts the inputs of the cooling coil. The airside inputs will come from the output of the AHU heating coil that precedes the AHU cooling coil. The extended hydronic system (chillers and pumps) has not been modelled in the present work as it is outside of the scope of this project and thus, the inputs for the coolant-side of the cooling coil model are currently taken directly from IBAL measurements rather than from any designed model components. Figure 3.3.1c showcases the wide variety of outputs available. The outlet coolant and air conditions are important in the sense that they can be passed to other

models of downstream components, as necessary. Outputs 9-11 are useful in that they quantify all elements of the airside energy balance. Specifically, these outputs report the total airside heat transfer along with the breakdown between sensible and latent components of the cooling load being met. This information can be used to compare the simulated airside heat transfer with the airside heat transfer calculated from the IBAL measurements. Output 12 provides the heat transfer on the coolant-side. This is used to verify that the model is balancing energy with the air-side. This output can also be compared to the calculated heat transfer of the coolant within the IBAL.

3.4 Cooling Coil Tuning

The tuning of the cooling coil consisted of using TRNOPT to discover the best possible combination of coil conductance ($UA_{coolant}$), coil capacitance (C_C), and bypass fraction (ϕ) to minimize the difference between the cooling coil model outputs compared to corresponding measurements from the IBAL. Since the cooling coil model reports both the outlet conditions of the air and the coolant, the error term TRNOPT attempts to reduce is given by:

$$e_{CC} = \left(\left| \Delta T_{cool,sim} - \Delta T_{cool,measured} \right|^2 + \left| \Delta T_{a,sim} - \Delta T_{a,measured} \right|^2 \right)^{\frac{1}{2}} \qquad (3.4.1)$$

where $\Delta T_{cool,sim}$ is the simulated temperature change of the coolant, $\Delta T_{cool,measured}$ is the measured temperature change of the coolant, $\Delta T_{a,sim}$ is the simulated temperature change of the air, and $\Delta T_{a,measured}$ is the measured temperature change of the air.

As Eq. (3.4.1) shows, e_{CC} is an error term that includes the differences between model-predicted temperature differentials and IBAL measured temperature differentials for both

the coolant-side and air-side of the cooling coil. The coolant error term and the airside error term are each squared to force TRNOPT into balancing both the airside error and the coolant error terms.

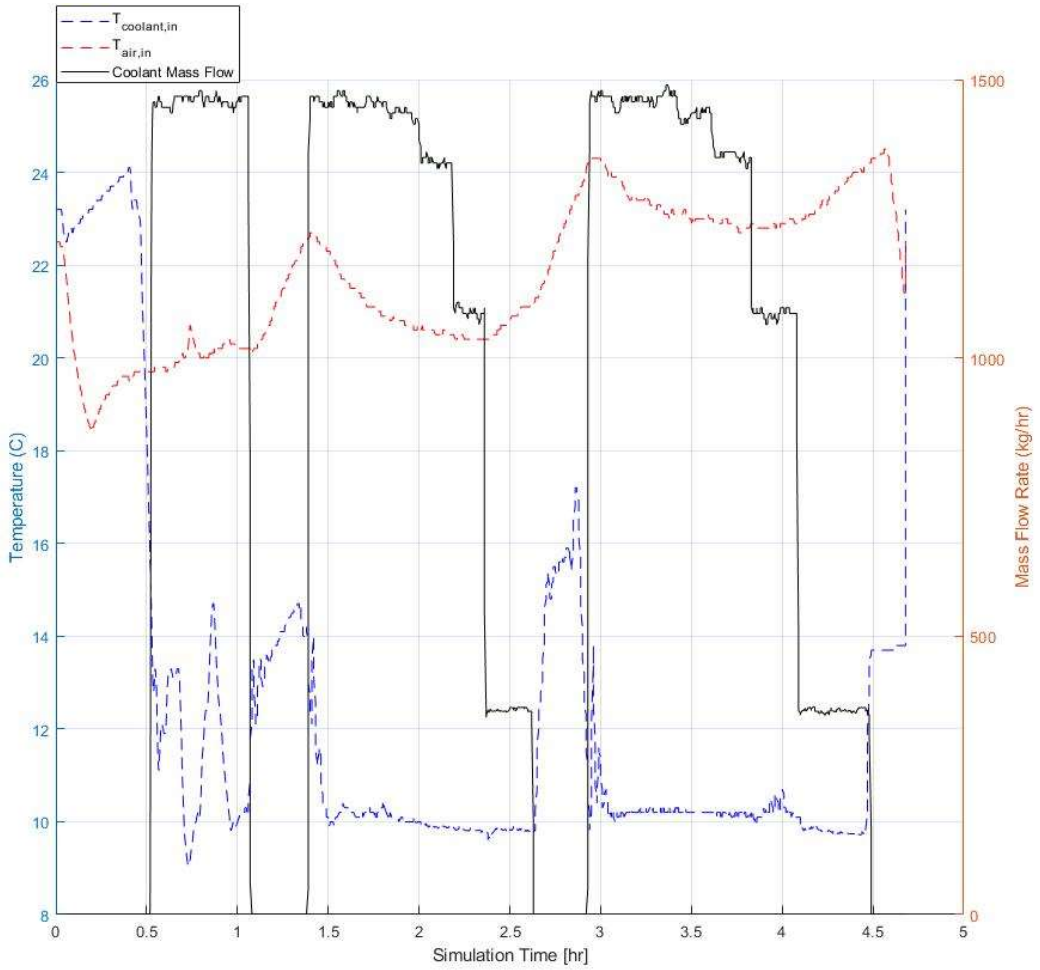

Figure 3. 4. 1: Inlet conditions for cooling coil test

The inlet conditions over a data period used to tune the parameters of the model is shown in Figure 3.4.1. The model was tuned using only those periods where the mass flow of coolant was greater than 0. While it is important to replicate the no flow behavior as best possible, so that the model is faithful in most possible scenarios, the most important aspect of the model is to capture the cooling coil performance over the typical operating

coolant flow range. The result of this optimization gave values of: $C_C = 5.41$ kJ/K, $UA_{coolant} = 14000$ kJ/hr-K, and $\phi = 0$. The biggest anomaly with these parameters is the small bypass value. The reason that the tuning tool optimizes to this value is because to attain maximum accuracy relative to the data, the model needs as much thermal interaction between the air and the cooling coil as possible. When a larger bypass fraction is used, the results on both the air-side and the coolant-side become notably worse, with respect to the measured data.

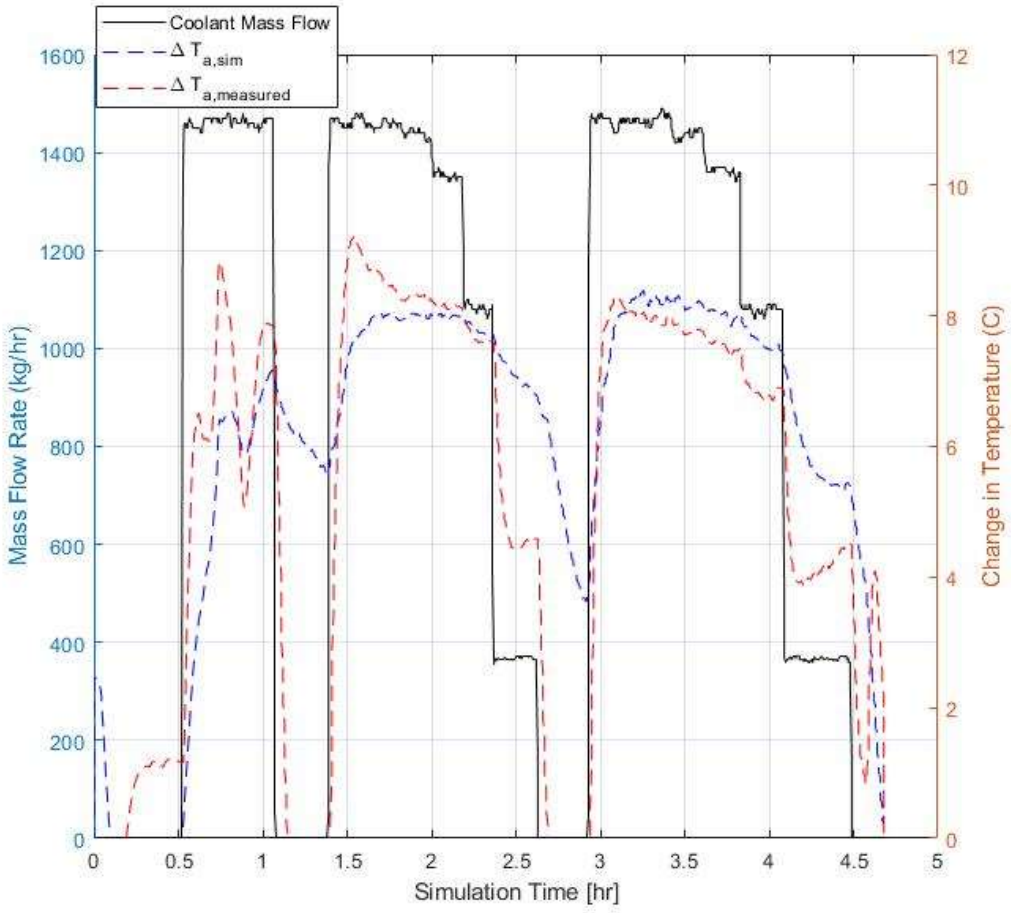

a)

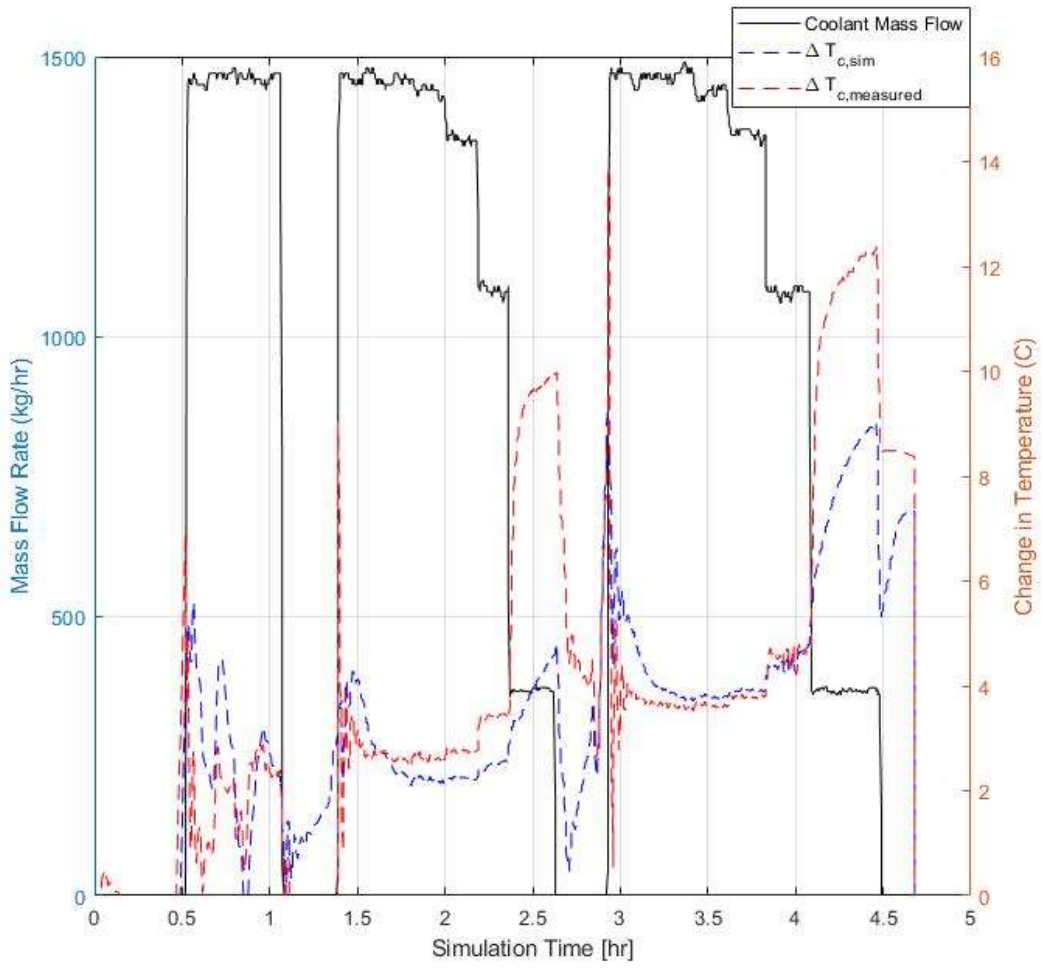

b)

Figure 3. 4. 2: a) Cooling coil airside change in temperature b) Cooling coil coolant change in temperature

Aside from the first hour of data presented in Figure 3.4.2a-b where the hydronic side of the IBAL was being adjusted as evidenced by the large fluctuation of coolant inlet temperatures, the temperature changes on the air-side and the coolant-side tend to remain within 1°C over the range of normal coolant flow rates (1500-1000 kg/hr) with much of the model predictions being within 0.5°C of the IBAL measured data. Additional data that were used to further verify the model can be found in Appendix A3 which show that, under low coolant flow rates (below 500 kg/hr), the air-side temperature rise of the model tends to be within 2°C of the measured data, whereas there is a much larger discrepancy

on the coolant-side temperature rise. Additionally, for all tests, the air-side flow rate was in the range of 700-1000 CFM, thus further work may include tuning the model at lower/higher flow rates to see if there is any substantial change in optimized parameters.

3.5 Variable UA Values

Noticeably, when the coolant flow goes below 500 kg/hr, the IBAL experiences rather large variations in temperature. The coolant temperature rises drastically while the air temperature goes towards zero. One reason as to why the model may not respond well to these low-flow scenarios is that $UA_{coolant}$ was initially set as a constant parameter of the model instead of varying with the flow rate. Since the model was tuned using the nominal flow scenarios, it stands to reason that the value may not reflect the $UA_{coolant}$ that would be observed under potentially laminar flow scenarios. Additionally, the converse scenario must be considered where under stagnant airflow scenarios, the air temperature will drive towards the coolant temperature. To account for these possibilities, an additional 2 parameters were added to the cooling coil model. Parameters 7 and 8 in Figure 3.3.1a depict these additions to the model. Parameter 7, low air flow *UA*, is used when the airflow is in a low-flow scenario. In this case, $UA_{coolant}$ is decreased substantially. This causes the effectiveness to drive towards 0, making $T_{liquid,out} = T_{liquid,in}$. This scenario has not been encountered or tested yet with the model, thus, the actual range where this parameter may be useful has not been established yet. However, the framework is in place if future work requires the model to be adapted to stagnant airflow scenarios. Parameter 8 is a low liquid flow *UA* that can be used if the coolant is in a low flow situation ($\dot{m}_{liquid} < 500$ kg/hr). Regarding the coil at the IBAL, this addition did not prove effective as was hoped. The TRNOPT value for $UA_{coolant}$ of 14000 kJ/hr-K is already so

large that in the low flow scenarios observed, the effectiveness was already at 0.995. This does not leave room for any substantial amount of additional heat transfer. Thus, while these additions make the coil model more dynamic and adaptable, they do not necessarily improve the model regarding its simulation of the AHU cooling coils.

3.6 Low Coolant Flow SS Energy Balance

Since the coil parameters were not explicitly adjusted to replicate the behavior of the IBAL at low coolant flow conditions, the steady state energy balance at low coolant flow based on the IBAL measurements was analyzed.

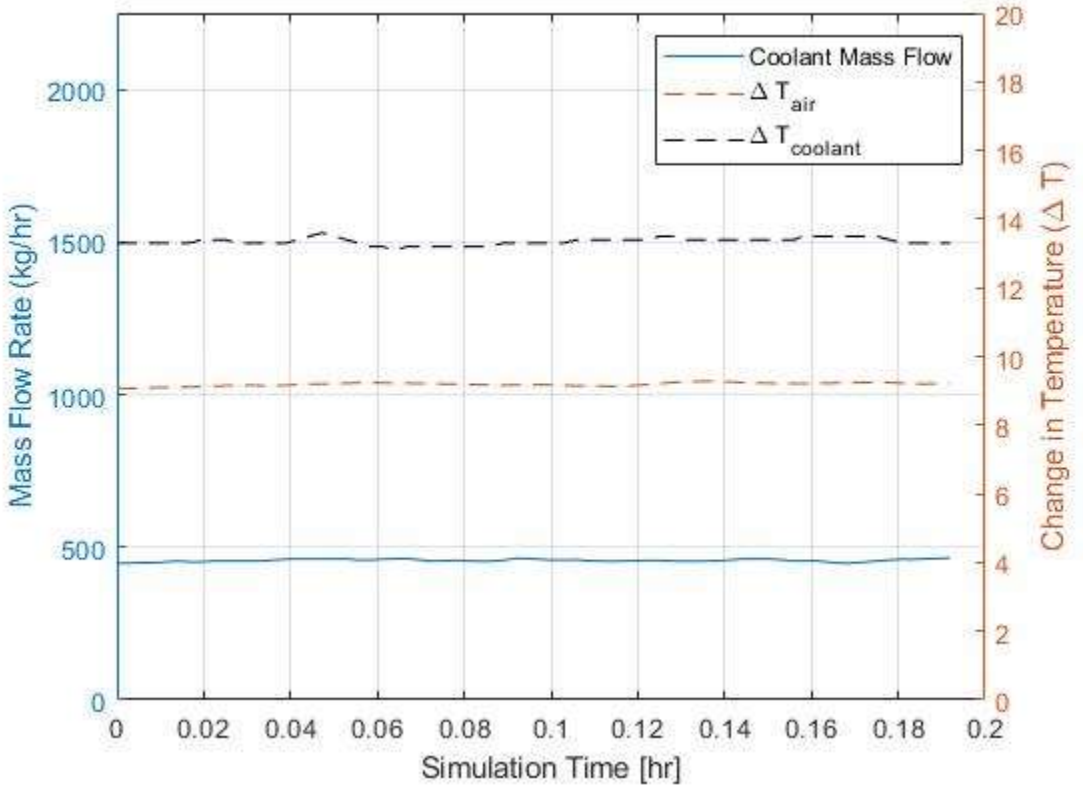

Figure 3. 6. 1: Steady state cooling coil conditions at low coolant flow

Figure 3.6.1 highlights a few important variables in the determination of the steady state period.

EES was then used to perform the steady state energy balance:

$$\dot{m}_{liquid}\ c_{liquid}\ \Delta T_{cool,measured} = \dot{m}_a \left(h_{a,in} - h_{a,out} \right) \tag{3.6.1}$$

where the air enthalpy was calculated using psychrometric tables. The result of this was an imbalance of energy where $\dot{m}_{liquid}\ c_{liquid}\ \Delta T_{cool,measured} = 6.454\,\text{kW}$ and $\dot{m}_a \left(h_{a,in} - h_{a,out} \right) = 5.372\,\text{kW}$. This is a 17% difference between the two energy terms. The effect of ignoring the condensation term was investigated to see if its inclusion would lessen the imbalance. The calculated condensate mass flow rate is $\dot{m}_{cond} = 4.3975\ E^{-4}$ kg/s, based on the calculated change in humidity ratio across the coil, along with the measured airflow across the coil. This results in an energy term two orders of magnitude below the energy terms derived above. Thus, by ignoring the effect of condensation no significant impact on the energy balance occurs. When calculating to see if this energy imbalance could be a result of the uncertainty associated with the measurement instruments, an uncertainty analysis was performed within EES. The uncertainty of each variable ($\dot{m}_{liquid}$, $\Delta T_{cool,measured}$, $\dot{m}_a$, $h_{a,in}$, and $h_{a,out}$) was determined from the Meta Data as provided by IBAL. An example of the relevant meta data uncertainty metrics as used in this analysis is provided in Appendix C. The result of the uncertainty analysis is shown in Figure 3.6.2.

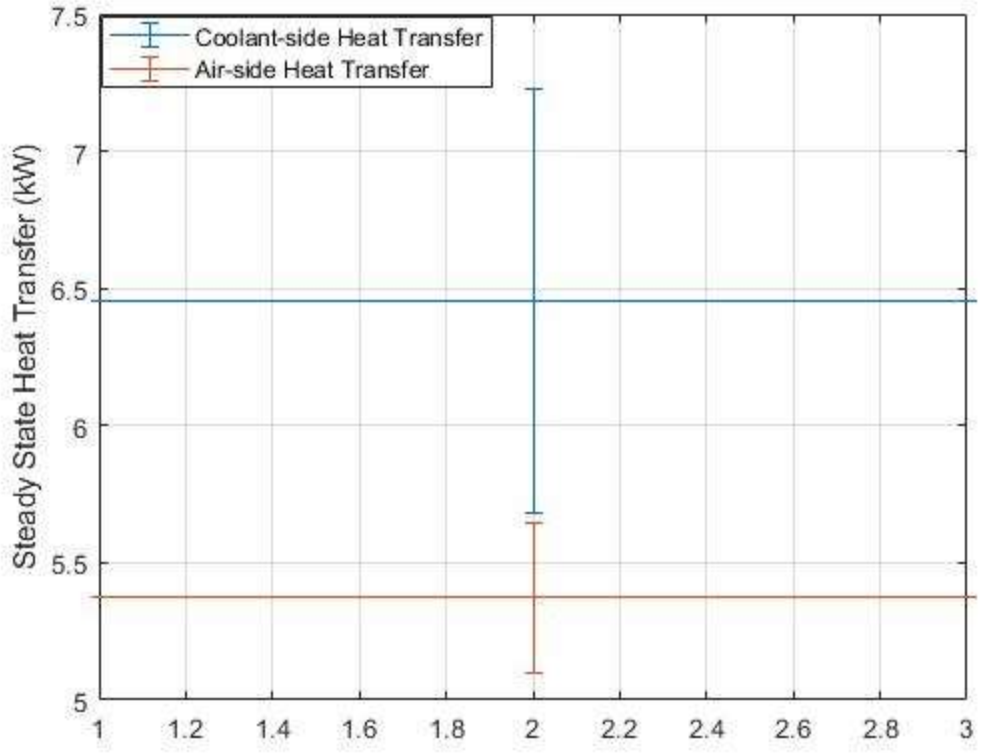

Figure 3. 6. 2: Steady state uncertainty results

While there is no overlap in the uncertainty analysis, it shows that the energy balance can come within a 5% difference. The predominant factor in this error is the uncertainty surrounding the coolant flow. According to the Meta Data, the flowmeter used to measure the volumetric flow of the coolant has an accuracy to within 0.21 gpm. This uncertainty accounts for 99% of the overall uncertainty on the coolant. As the coolant flow is reduced, the impact of this accuracy is magnified. At maximum flow the relative error generated by this accuracy is just 2%. At the lower coolant flows, this relative error increases to 11%. Overall, it appears that the difference between the cooling coil model and the measured data can be largely explained to uncertainty in instrumentation, with the most notable measurement being the glycol flowmeter. An additional heat loss term may be added and tuned in future work to ensure that the measured data better balances

energy, which when implemented into the model will allow the model to better match the data.

3.7 Summary

The standard TRNSYS cooling coil model was adapted to include a thermal storage term to capture the transient performance of the IBAL's actual cooling coil. The transient cooling coil model was tuned using measured data from the IBAL with TRNOPT. The tuning process reduced an error term that was designed to capture both the airside error and the hydronic-side error in a singular term. Upon testing the tuned cooling coil model, the simulated air and coolant outlet temperatures were within 1°C of their measured counterparts during nominal flow operation. As the cooling coil model trends towards low coolant flow scenarios, the model does not mimic the behavior of the IBAL as well leading to a 2 °C difference compared to measured data. To make the model more robust in various low-flow scenarios, additional conductance parameters were added to the model. These were designed to impact the effectiveness of the model depending on the situation (laminar flow or stagnant airflow). While potentially useful in future work, these additions did not prove to lessen the low coolant flow discrepancy that was observed. Instead, an energy balance on the steady state behavior of the coil determined that the measured air-side heat transfer differed from the coolant-side heat transfer by 17%. Looking at the uncertainty of the temperature sensors and the flowmeters, the overall difference between the air-side energy balance and the coolant-side could range between 5%-30%. In the future, further work could be done to reduce the extent of this overall uncertainty within the system. After this is complete, the model may be re-tuned and/or a

heat loss term may be added to ensure performance within an expected range of the measurements.

CHAPTER IV

Airflow and Pressure Component

4.1 Introduction

The previous sections developed the methods of modeling the heating coil and cooling coil. This section describes a component that predicts the effect of the fans and dampers in the IBAL HVAC system. The purpose of this component is to calculate the pressure drop across each damper and the pressure rise generated by the fan, along with the associated flow at the various points of the system. The primary function of this component is that it allows the model to operate without the need for airflow data as input. Instead, the system airflow is predicted as a function of inputs that correspond to the physical parameters that are controlled by the IBAL (e.g., damper position and fan speed).

4.2 Initial Fan and Damper Curve Derivation

This model uses inputs that include the AHU fan speed and the damper positions associated with the various dampers located throughout the IBAL system. Additionally, the model operates with boundary conditions corresponding to the specified upstream pressure and downstream pressure which would be related to the operation of the outdoor air handling unit and the exhaust fans, which are not explicitly included in the present model. Figure 4.2.1 depicts those portions of the air-side of the IBAL as implemented in the TRNSYS component.

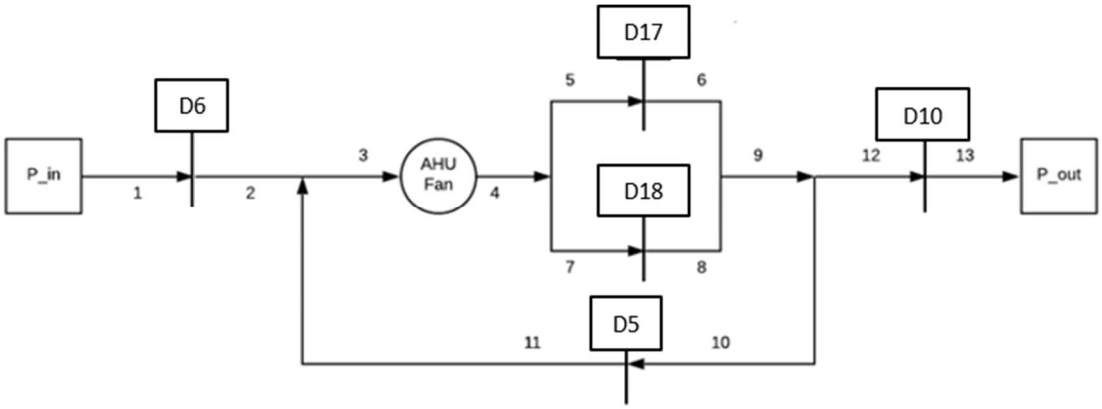

Figure 4. 2. 1: AHU1 air-side airflow and pressure component diagram

Aside from the depiction of the location of the dampers and the fan in the system, the diagram identifies each point where the model calculates the flow and pressure. The model enforces continuity of flow and equalization of pressure at all intersection points. At each damper (D), the pressure drop is calculated based on the position of the damper and the flow of the air passing through the damper. The damper numbering, D5, D6, etc. correspond to the actual damper numbering scheme used in the as-installed IBAL system. The pressure rise across the fan is calculated from the fan speed and the flow of air passing through the fan. The initial relationships used in the model were derived from the manufacturer fan curves that were available (Trane, 2014). The AHU supply fan's static pressure rise as a function of airflow for a variety of fan speeds and damper positions is shown in Figure 4.2.2

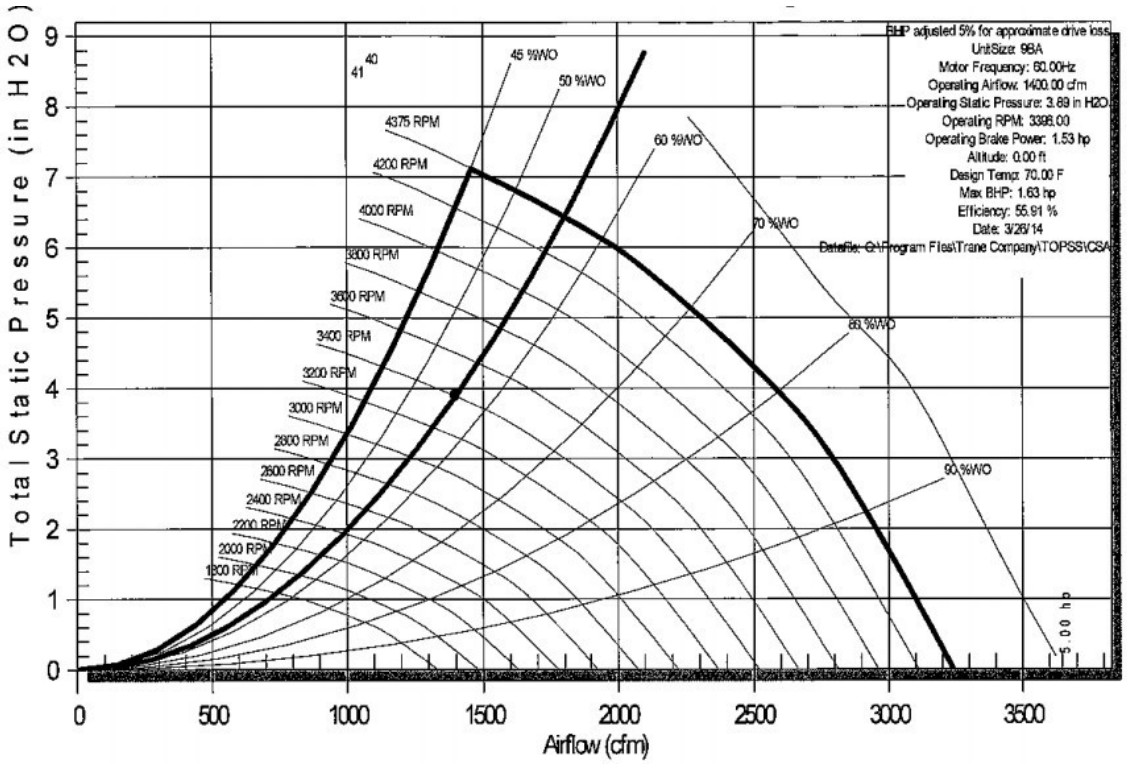

Figure 4. 2. 2: Manufacturer fan and damper performance curves for the IBAL AHU fan.

This chart was digitized and the resulting data loaded into EES, where the fan performance is characterized by normalizing the static pressure rise by the maximum pressure rise and developed air flow normalized by the maximum air flow at a given fan speed. A similar process was followed for the various dampers used in the IBAL. That is, the air flow through the damper at a given damper position was normalized by the maximum air flow and pressure drop at a wide-open damper position Curve fits for normalized fan pressure rise and normalized damper pressure loss as a function of normalized air flow rate were developed based on Figure 4.2.3a and Figure 4.2.3b, respectively.

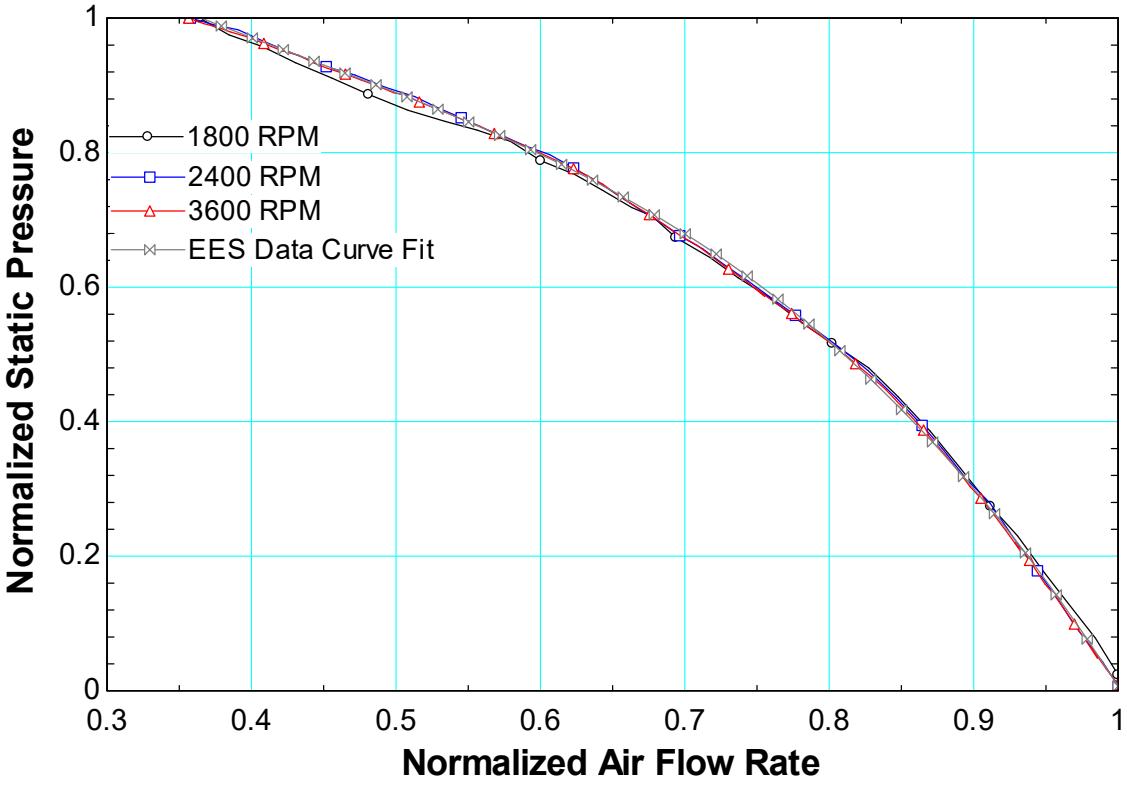

a)

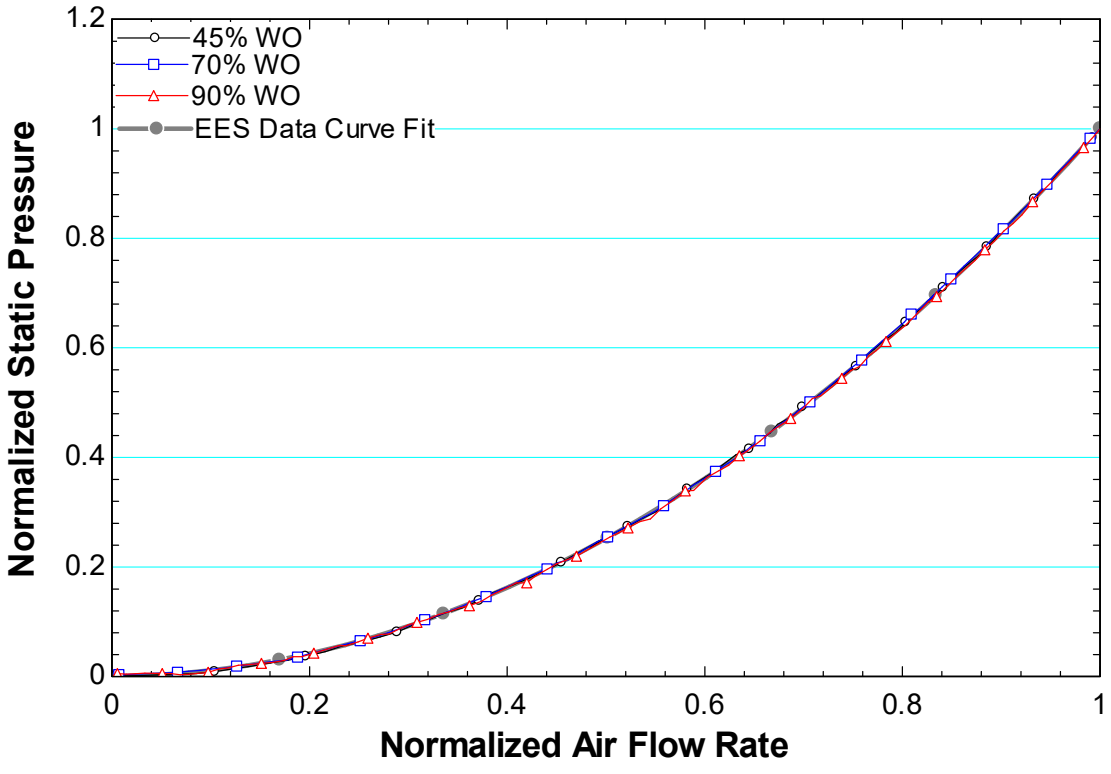

b)

Figure 4. 2. 3: a) Normalized fan performance curve b) Normalized damper performance curve

As Figure 4.2.3a and Figure 7 show, once the fan performance curves and damper performance curves are normalized there is almost no difference between them. The curve fits to these data are shown in Eqs. (4.2.1) and (4.2.2):

$$\overline{P}_{fan} = 1.51 - 2.32\overline{F}_{fan} + 3.49\overline{F}_{fan}{}^{2} - 2.67\overline{F}_{fan}{}^{3} \tag{4.2.1}$$

$$\overline{P}_{damper} = 0.013\overline{F}_{damper} + 0.975\overline{F}_{damper}{}^{2} + 0.014\overline{F}_{damper}{}^{3} \tag{4.2.2}$$

where $\overline{P}_{fan}$ is the normalized pressure for the fan curve in inches of water gauge, $\overline{F}_{fan}$ is the normalized air flow for the fan curve in CFM, $\overline{P}_{damper}$ is the normalized pressure for the damper curve, and $\overline{F}_{damper}$ is the normalized air flow for the damper curve. These terms are defined by the Eqs. (4.2.3)-(4.2.6):

$$\overline{P}_{fan} = \frac{P}{P_{\max,\,fan}} \tag{4.2.3}$$

$$\overline{F}_{fan} = \frac{F}{F_{\max,\,fan}} \tag{4.2.4}$$

$$\overline{P}_{damper} = \frac{P}{P_{\max,damper}} \tag{4.2.5}$$

$$\overline{F}_{damper} = \frac{F}{F_{\max,damper}} \tag{4.2.6}$$

where P is the pressure rise or drop calculated by the model and F is the air flow rate.

Figure 4.2.4 shows the maximum air flow rate and maximum static pressure rise as a function of fan speed. Figure 4.2.4b shows the maximum air flow rate and maximum static pressure drop as a function of damper position.

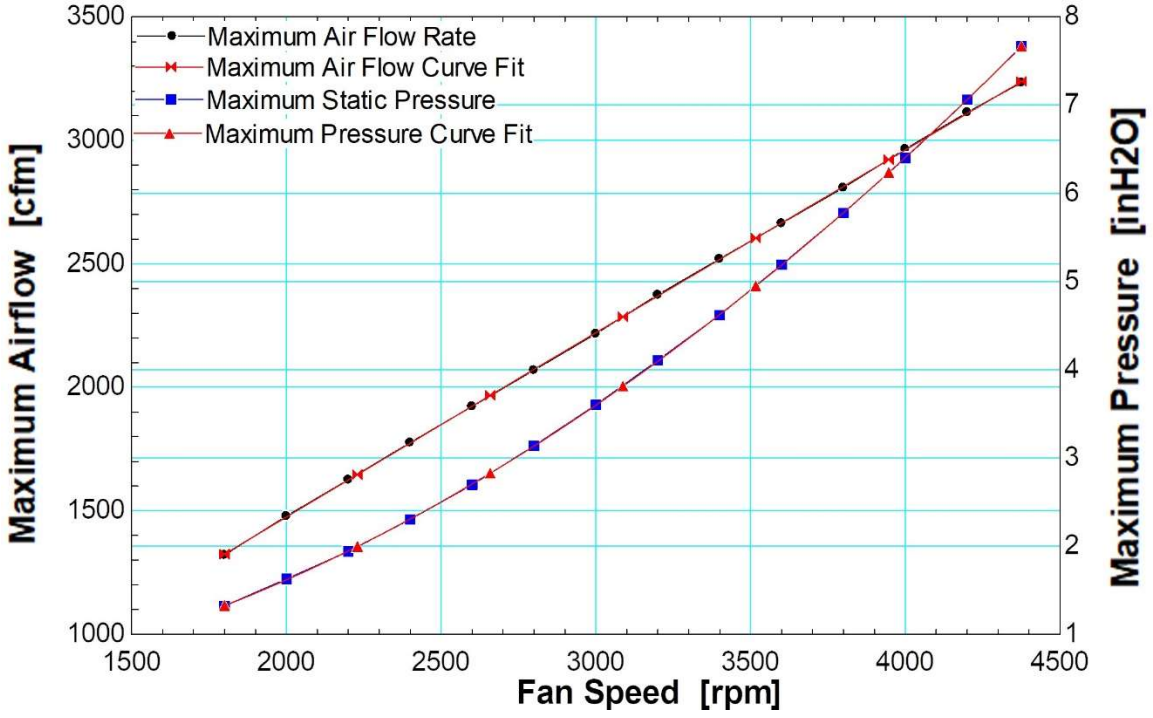

a)

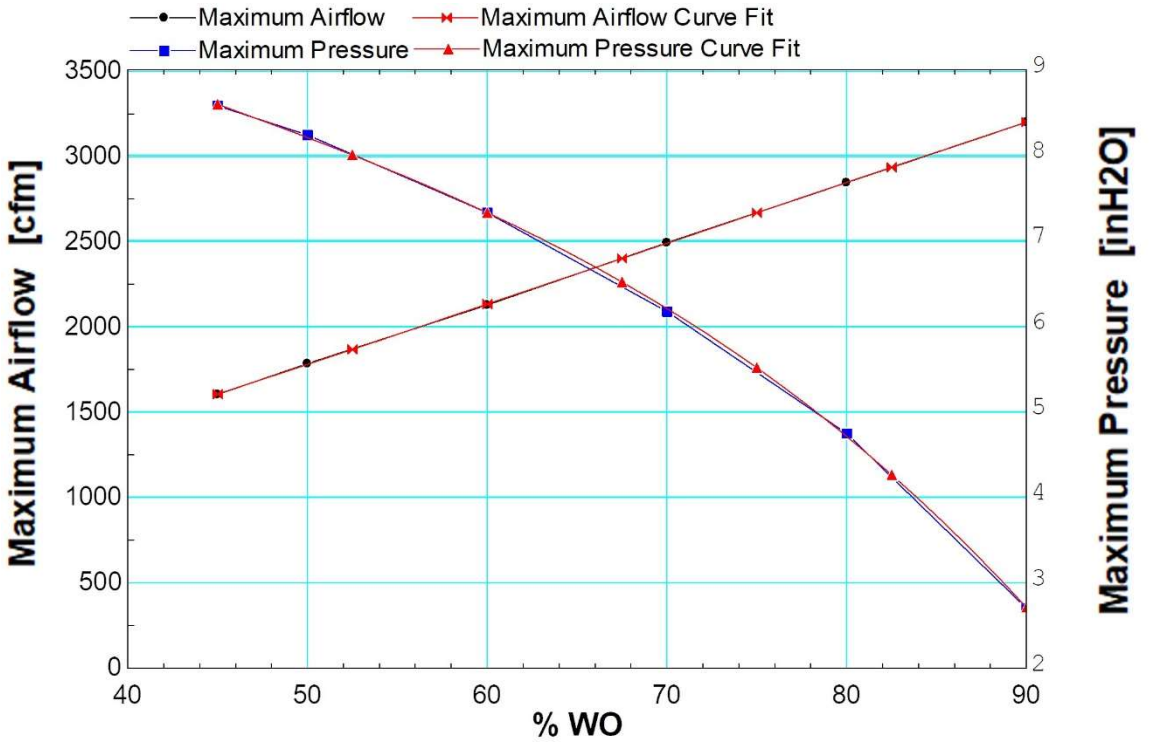

b)

Figure 4. 2. 4: a) Max airflow and max pressure rise as a function of fan speed b) Max airflow and max pressure rise as a function of damper position

The final step in preparation for the creation of the system airflow component was the characterization of the curve fits of each set of data from Figure 4.2.4a and Figure 4.2.4b. These curves are represented by Eqs. (4.2.7)-(4.2.10):

$$F_{\max,\,fan} = -54.707 + 0.782 f - 9.88E^{-6} f^2 + 7.47E^{-10} f^3 \tag{4.2.7}$$

$$P_{\max,\,fan} = 0.321 - 2.86E^{-4} f + 4.82E^{-7} f^2 - 7.64E^{-12} f^3 \tag{4.2.8}$$

$$F_{\max,damper} = 182.861 + 27.445\ WO + 0.119\ WO^2 - 5.65E^{-4}\ WO^3 \tag{4.2.9}$$

$$P_{\max,damper} = 13.520 - 0.187\ WO + 2.70E^{-3}\ WO^2 - 2.18E^{-5}\ WO^3 \tag{4.2.10}$$

where $F_{\max,\,fan}$ is the maximum airflow from the fan speed curve in CFM, $P_{\max,\,fan}$ is the maximum pressure from the fan speed curve in inches of water, f is the fan speed in RPM, $F_{\max,damper}$ is the maximum airflow from the damper curve in CFM, $P_{\max,damper}$ is the maximum pressure from the damper curve in inches of water, and WO is the damper position expressed as a % of its wide open position.

4.3 TRNSYS Implementation

Armed with these equations that describe the fan and damper characteristics, it is possible to use them to simulate the air-side of the IBAL as shown in Figure 4.2.1 in TRNSYS. The air flow at any point is denoted by F_x where *x* is the node number that corresponds to Figure 4.2.1. Similarly, the calculated air-side static pressure at any point will be denoted by P_x where *x* is the node number that corresponds to Figure 4.2.1. The system requires, as inputs, the positions of each of the dampers and the speed of the AHU fan. The system also has two boundary conditions: the inlet pressure (P_{in}) and the outlet pressure (P_{out}). TRNSYS begins with initial guess values for $F_1$and F_{11}. The system then goes node by

node enforcing continuity of flow and pressure. This process begins at node 1 where the first boundary condition is enforced:

$$P_1 = P_{in} \tag{4.3.1}$$

as the next node lies on the other side of a damper (D6), there will be a pressure drop and thus P_2 is calculated as:

$$P_2 = P_1 - \Delta P_{D6} \tag{4.3.2}$$

where ΔP_{D6} is calculated by using F_1 and the physical position of D6. To enforce continuity of flow on both sides of the damper the flow between node 1 and node 2 is the same:

$$F_2 = F_1 \tag{4.3.3}$$

since no components separate node 2 and node 3, there is no pressure rise or drop between these two nodes, thus:

$$P_3 = P_2 \tag{4.3.4}$$

enforcing continuity of flow at node three gives the equation:

$$F_3 = F_2 + F_{11} \tag{4.3.5}$$

at node 4 there will be a pressure rise because of the fan, this is calculated by the equation:

$$P_4 = P_3 + \Delta P_{fan} \tag{4.3.6}$$

where ΔP_{fan} is calculated by using F_3 and the fan speed f. The flow does not change across the fan:

$$F_4 = F_3 \tag{4.3.7}$$

At this point, the air splits between nodes 5 and 7. In order to calculate how the air is split between the two branches, a subroutine runs that uses the positions of D17, D18, the flow F_4, and a fraction ($frac$) that determines how the air is split between the two branches. This function begins with a lower bound value of $frac$ ($frac_{low}$) starting at 0. The pressure drop at D18 is calculated by the position of the damper and $frac_{low}$ F_4 . The pressure drop at D17 is calculated using the position of this damper and the flow rate determined by $\left(1 - frac_{low}\right)$ F_4 . This creates a lower error term (err_{low}) that is defined by the difference between calculated damper pressures of D18 and D17. $frac_{low}$ is then incremented by 0.05 to create $frac_{high}$ and the same process occurs to calculate the damper pressures to create a higher error term (err_{high}). If err_{high} is less than 0, then the process repeats with err_{high} being substituted in for err_{low} . Additionally, the $frac_{high}$ term is substituted into the $frac_{low}$ term. Once the subprogram iterates to a point where err_{high} is above 0, the final output for $frac$ is determined by the equation:

$$frac = frac_{low} + \frac{0.05\ \left(0 - err_{low}\right)}{err_{high} - err_{low}} \tag{4.3.8}$$

With this iteration completed, the flow at node 5 and node 7 is calculated by:

$$F_5 = \left(1 - frac\right)\ F_4 \tag{4.3.9}$$

$$F_7 = frac\ F_4 \tag{4.3.10}$$

additionally, the pressures at nodes 5 and 7 is:

$$P_5 = P_4 \tag{4.3.11}$$

$$P_7 = P_4 \tag{4.3.12}$$

The pressure at node 6 is calculated by using the damper pressure drop equation:

$$P_6 = P_5 - \Delta P_{D17} \tag{4.3.13}$$

where ΔP_{D17} is calculated by using F_5 and the position of D17. Enforcing continuity of flow:

$$F_6 = F_5 \tag{4.3.14}$$

The pressure at node 8 is then found:

$$P_8 = P_7 - \Delta P_{D18} \tag{4.3.15}$$

where ΔP_{D18} is calculated by using F_7 and the position of D18. At node 9, Eqs. (4.3.16) and (4.3.17) represent the pressure and flow:

$$P_9 = P_6 \tag{4.3.16}$$

$$F_9 = F_6 + F_8 \tag{4.3.17}$$

Node 10 maintains continuity through:

$$F_{10} = F_{11} \tag{4.3.18}$$

$$P_{10} = P_9 \tag{4.3.19}$$

The model then calculates the flow and pressure at node 12:

$$F_{12} = F_9 - F_{10} \tag{4.3.20}$$

$$P_{12} = P_9 \tag{4.3.21}$$

the pressure at node 13 is calculated using the pressure drop calculation across D10:

$$P_{13} = P_{12} - \Delta P_{D10} \tag{4.3.22}$$

with ΔP_{D10} being determined by the position of D10 and the flow at F_{12}. Additionally, the flow at point 13 is:

$$F_{13} = F_{12} \tag{4.3.23}$$

At this point an error term (err_2) is determined by comparing P_{13} to P_{out} as shown in Equation (4.3.24):

$$err_2 = P_{13} - P_{out} \tag{4.3.24}$$

The final steps of the main loop involves calculating P_{11} to compare it with P_2:

$$P_{11} = P_{10} - P_{damper} \tag{4.3.25}$$

The final P_{damper} term is found using D5 and F_{11}. The error term that relates P_{11} and P_2 is:

$$err_3 = P_{11} - P_2 \tag{4.3.26}$$

The model then attempts to first reduce err_2. This is done by creating a lower bound on the error ($err_{2,low}$) with an initial $F_{1,low}$ value of 0 by using Eqs. (4.3.1)-(4.3.26). Similarly, a higher bound on the error ($err_{2,high}$) is generated with the same methodology with the only difference being that $F_{1,low}$ is incremented by 10 to create the $F_{1,high}$ term that is used. While $err_{2,high}$ is greater than 0, this process will repeat with $F_{1,high}$ substituting into $F_{1,low}$ and $err_{2,high}$ being placed into $err_{2,low}$. Once $err_{2,high}$ is less than 0, F_1 is determined by:

$$F_1 = F_{1,low} + \frac{10\ \left(0 - err_{2,low}\right)}{\left(err_{2,high} - err_{2,low}\right)} \tag{4.3.27}$$

The last term that requires error reduction is F_{11}. The error involved with this term is reduced as err_3 is lessened. To do this, an initial $F_{11,low}$ term of 1 is used as the input for Eqs. (4.3.1)-(4.3.27). This creates a lower error term ($err_{3,low}$). A higher error term ($err_{3,high}$) is created by incrementing $F_{11,low}$ by 100 to create $F_{11,high}$ and then repeating the process of Eqs. (4.3.1)-(4.3.27) with that input. If the resultant $err_{3,high}$ is greater than 0, the process will repeat with $F_{11,high}$ and $err_{3,high}$ being substituted into $F_{11,low}$ and $err_{3,low}$, respectively. Once the error term is less than 0, F_{11} is calculated by:

$$F_{11} = F_{11,low} + \frac{100\ \left(0 - err_{3,low}\right)}{\left(err_{3,high} - err_{3,low}\right)} \tag{4.3.28}$$

The result of this process is a program that returns the flow at each point shown in Figure 4.2.1 based on the fan speed and the damper positions within the system in conjunction with the inlet and outlet boundary conditions, P_{in} and P_{out}. This entire process described in this section is graphically depicted in figure 4.3.1.

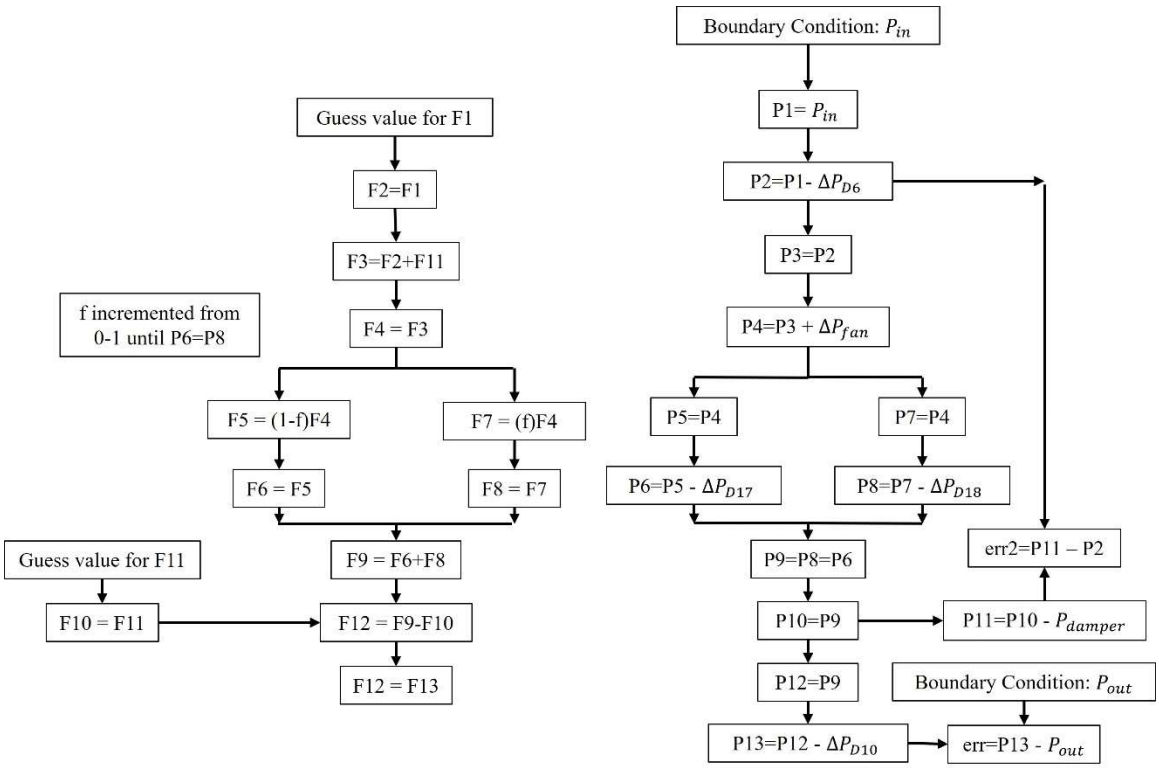

Figure 4. 3. 1: Airflow and pressure calculation flow chart

4.4 Manufacturer Model Verification

To verify the model is working correctly, a few test conditions were simulated. Figure 4.4.1 shows the pressures and flow rates at two locations (nodes 4 and 11 in Figure 4.2.1) for a case where all damper positions are held constant while the fan speed increases from 1800 rpm to 3600 rpm. Referring to Figure 4.4.1, locations 4 and 11 correspond to the location downstream of the AHU fan and the return air branch downstream of Damper 2.

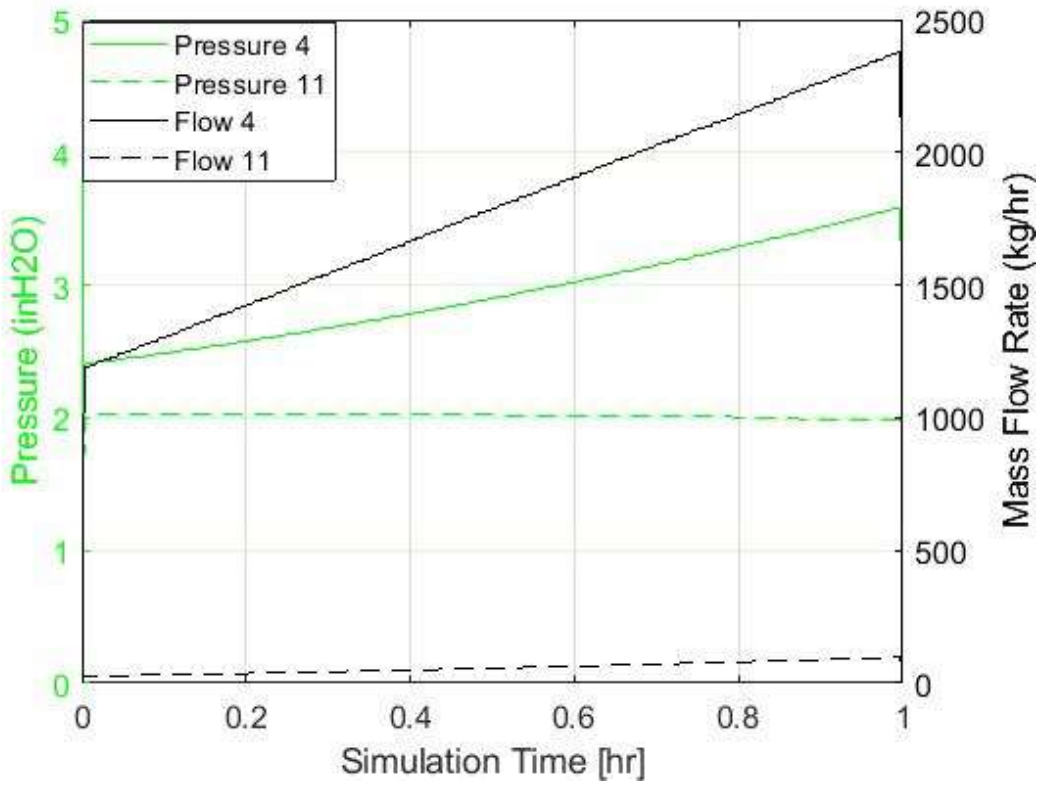

Figure 4. 4. 1: Pressure and flow rate downstream of the AHU (location 4) and in the return branch (location 11) as the fan speed increases.

Note that downstream of the AHU (at node 4), both the flow and pressure increase quickly as the fan speed increases. The flow and pressure at location 11 are also affected by this change in fan speed; the pressure goes down slightly and the flow increases. This behavior follows the expected pattern as the fan speed increases. A larger fan speed should generate a greater pressure rise and associated flow across the fan. Additionally, the behavior across the damper makes sense as the increase in flow across a constant damper configuration will yield a greater pressure drop relative to the decreased flow pressure drop.

4.5 IBAL Comparison

While the behavior of the airflow and pressure calculation component predicts reasonable results as shown in Figure 4.4.1, it is necessary to compare the predictions to the behavior of the IBAL. To do this, data from the IBAL was collected across a wide range of fan speeds and system resistances as shown in Figure 4.5.1. In this case, the dampers were alternately open and shut to their maximum and minimum positions. The minimum position for each damper in the system is varied as the effective operating range is different for each damper. Thus, fully closed for one damper may be around 20%WO while for other dampers it may be closer to 0 %WO. This behavior is analyzed further in section 4.6.c.

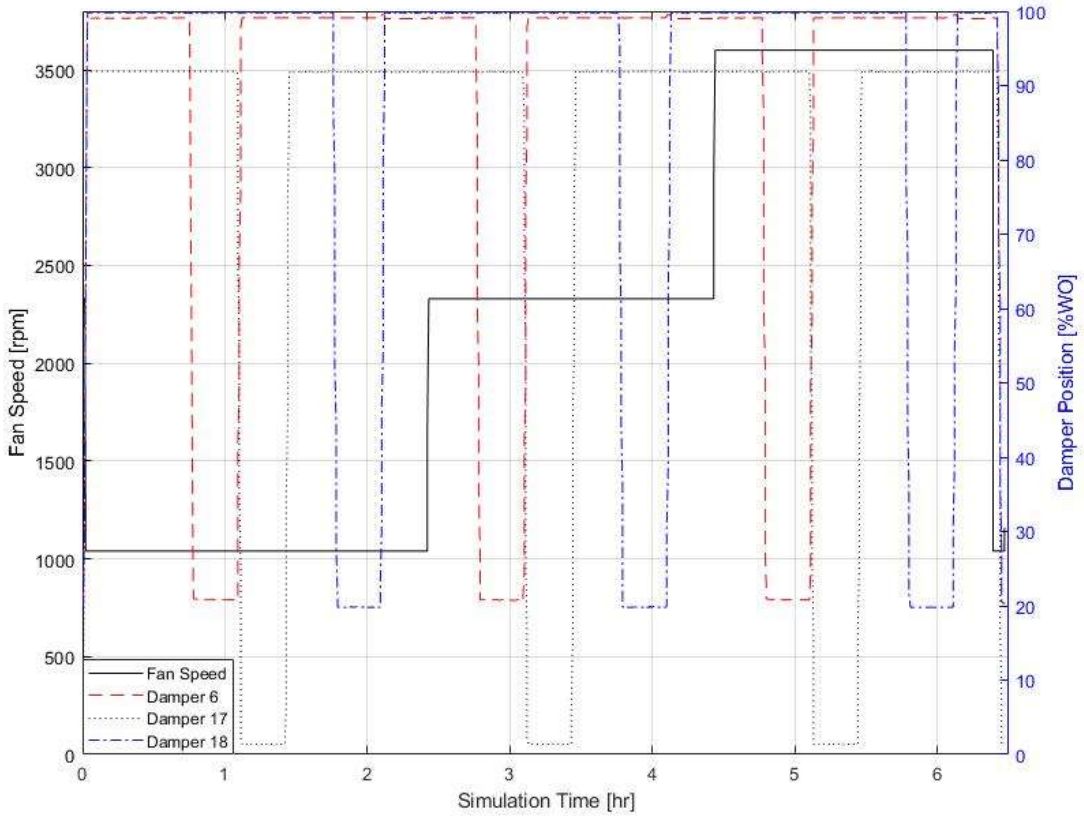

Figure 4. 5. 1: IBAL measurements used as model inputs for comparison

Using these inputs, along with the inputs for damper 5 and damper 10 (which were also alternated in a similar fashion), the model calculated the pressure rise and the flow across the AHU fan. The comparison between these calculated values and the measured airflow and measured pressure rise across the fan is shown in Figure 4.5.2.

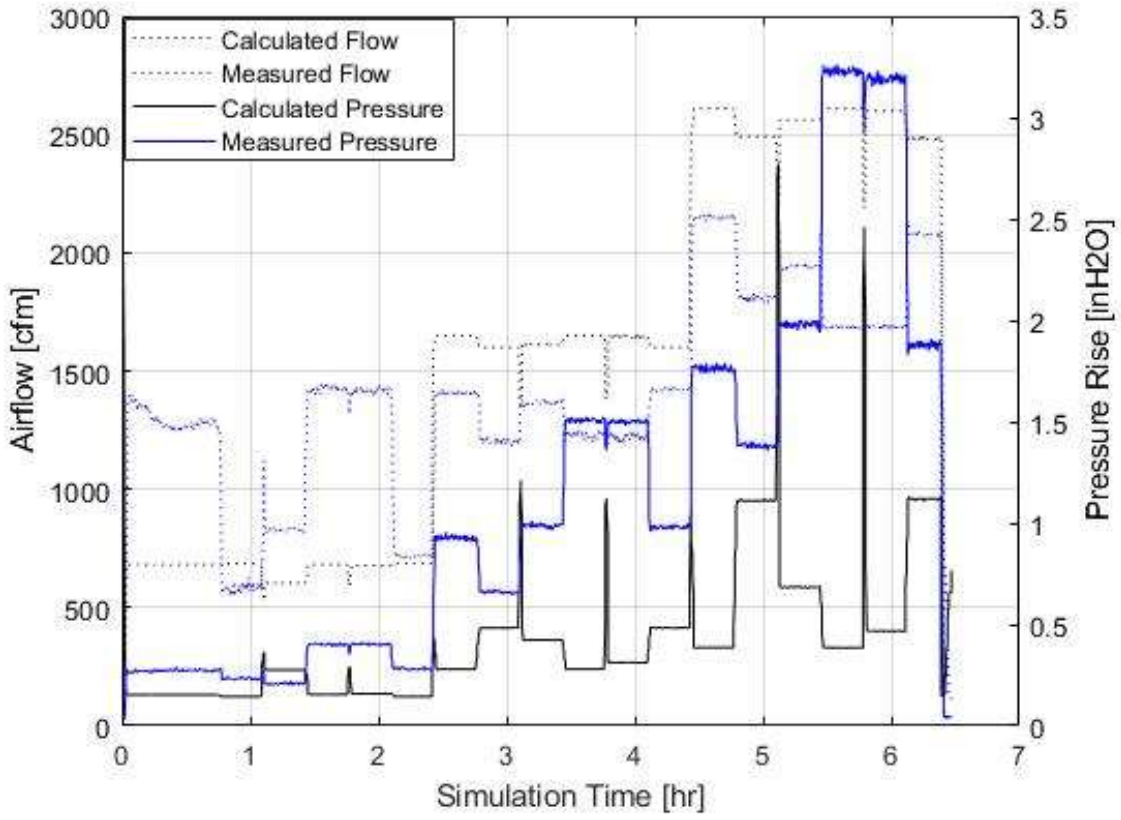

Figure 4. 5. 2: Airflow and pressure comparison using manufacturer-supplied information

Noticeably, when using the IBAL inputs in the model, both the calculated pressure and calculated flow in the system appear to differ dramatically from the measured data. As the model utilizes both the fan and damper curves to arrive at a converged solution for airflow and pressure, it stands to reason that the manufacturer curves that were used in the initial development of the model do not sufficiently capture the behavior of their IBAL counterparts.

4.6 Model Tuning

4.6.a Tuning Overview

In terms of adjusting the model, the primary mechanisms that can be tuned are the fan and damper curves. To understand how these components behave in the IBAL, data was taken in isolation for the fan and specific dampers to characterize their actual in-situ performance. Once these relationships are determined, they can be implemented into the model easily as the model derivation described in section 4.3 will remain the same, but it will use the updated curves instead of the manufacturer curves.

4.6.b AHU Fan Curve Examination

4.6.b (i) Effect of the OAU Fan

The easiest component to examine was the AHU fan. The reason for this is that there are pressure sensors immediately upstream and downstream of the fan, allowing for the measured pressure rise across the fan to be easily ascertained. The flow through the fan was calculated by using the flow sensors of the AA and the RA branches to determine the total flow through the AHU as shown in Figure 4.6.1.

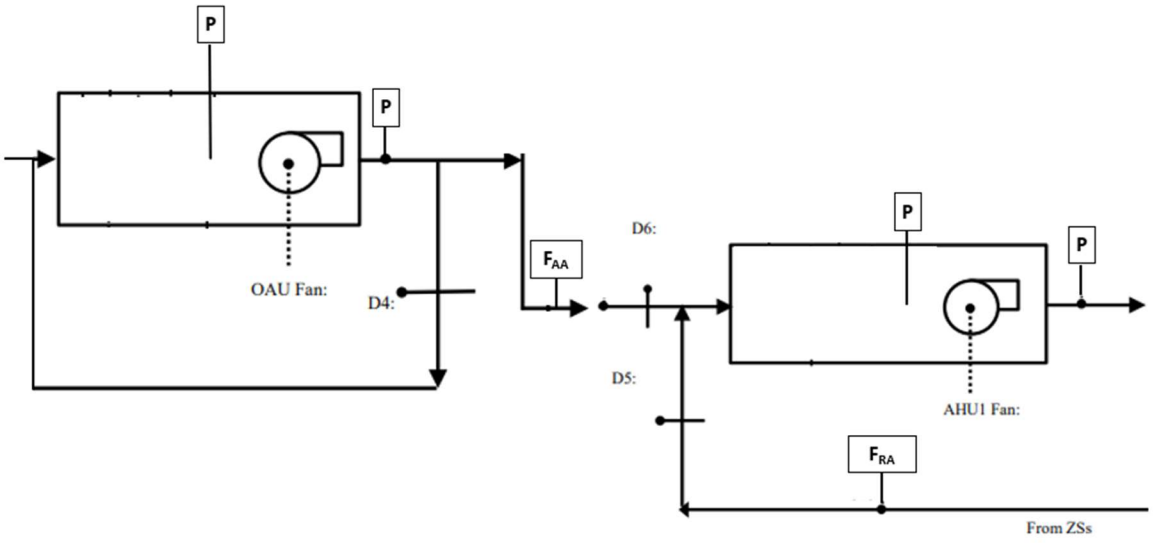

Figure 4. 6. 1: OAU and AHU1 pressure and flow sensor locations

The first aspect of the fan curve that was analyzed is the impact that the OAU fan might have on the fan curve. This was done to ensure that the pressure boundary condition for the AHU successfully accounts for these variations.

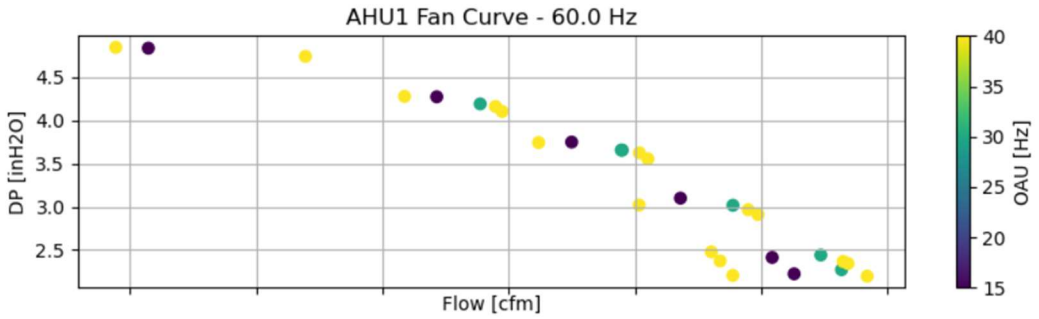

Figure 4. 6. 2: 60 Hz AHU fan curve for varying OAU fan speeds

Figure 4.6.2 shows the measured pressure rise across the AHU fan as a function of the measured flow for an AHU fan speed of 60 Hz (3600 rpm) with the OAU fan speed varying. The OAU fan was set to 3 different fan speeds and the system resistance was varied by closing D17 and D18 in unison to map the AHU fan curve. Overall, when the OAU fan speed is adjusted, there does not appear to be much deviation of the fan curve at higher system resistances (i.e., higher pressure drop). At lower resistances, there is slightly more deviation in the airflow, but this variation is relatively small. Therefore, the Airflow/Pressure component does not need to account for the conditions of the OAU beyond using the inlet pressure boundary condition that is already included in the model.

4.6.b (ii) Effect of Damper 7

Next, the impact of damper 7 on the AHU 1 fan curve was tested. As shown in figure 4.6.3, damper 7 is in the supply air branch of AHU 2. This component was examined to verify that the boundary pressure would be sufficient to handle any variation that would be caused by changes in its position.

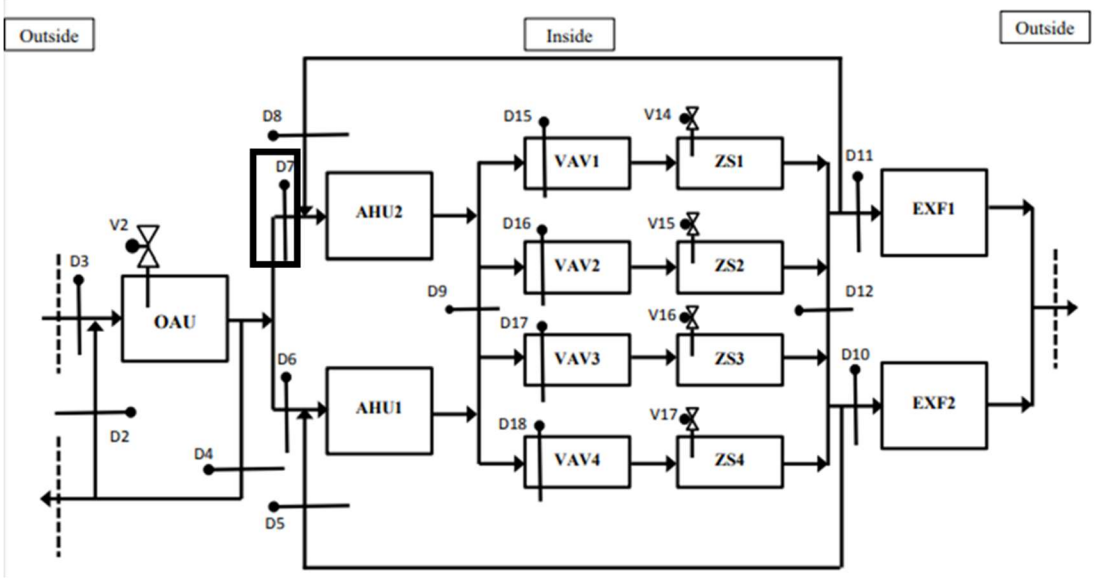

Figure 4. 6. 3: Damper 7 location within the schematic

The Airflow/Pressure component simulates the AHU fan using a fan curve that is not affected by either the OAU speed or the position of AHU branch damper (D7). Thus, it is expected that adding or removing resistance outside of the zone (such as by actuating damper 7) would generate data that follows the same fan curve for any given fan speed.

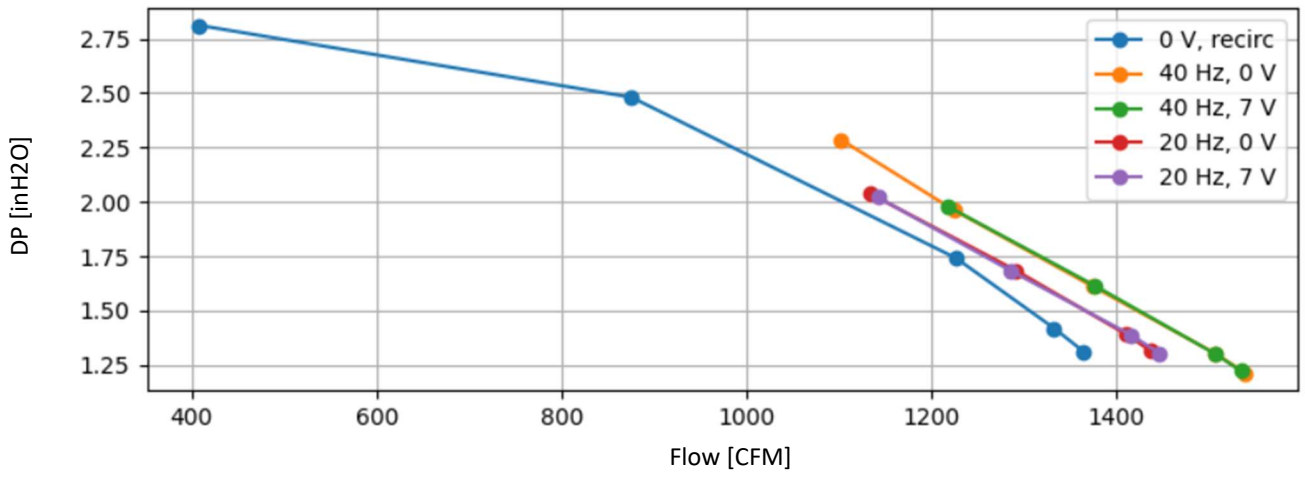

Figure 4. 6. 4: 45 Hz AHU fan curve for varying D7 position and OAU fan speed

Figure 4.6.4 shows the fan curve for the AHU1 fan operating at 45 Hz with the OAU speed being varied between 20-40 Hz while damper D7 is both fully open (7 V) and fully closed (0 V). P_{in} varied between 0-0.12 for the entirety of the data collection. The first observation that can be made is the position of the D7 damper does not shift the fan curves at all. This indicates that D7 should not have any impact on the model that the existing framework cannot handle as it does not shift the fan curves. A second observation regards the impact of the OAU fan. While there is some slight deviation (consistent with what is seen in Figure 4.6.2) at the lower system resistances, the impact of the OAU fan does not seem to significantly impact the fan curve; this further validates the established model framework.

4.6.b (iii) Measured Fan Curves

After verifying that both the OAU fan and the dampers outside the airflow calculator scope were not a source of error, data was collected to determine the actual fan curve of the IBAL AHU fan. This was done by measuring the pressure rise across the fan at two fan speeds across a wide range of system resistances.

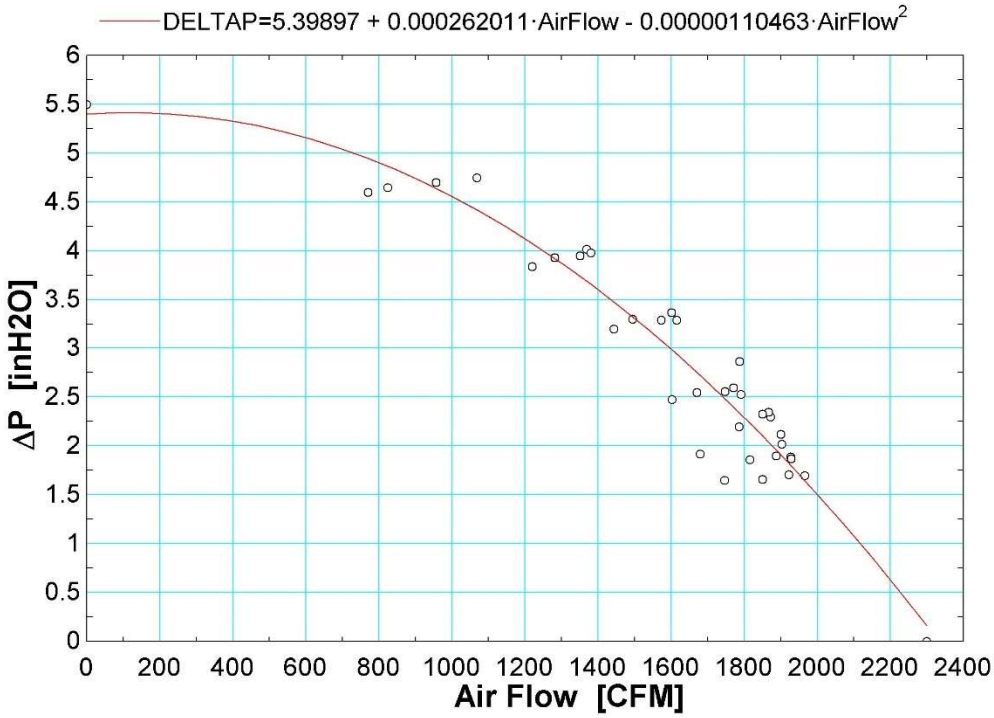

a)

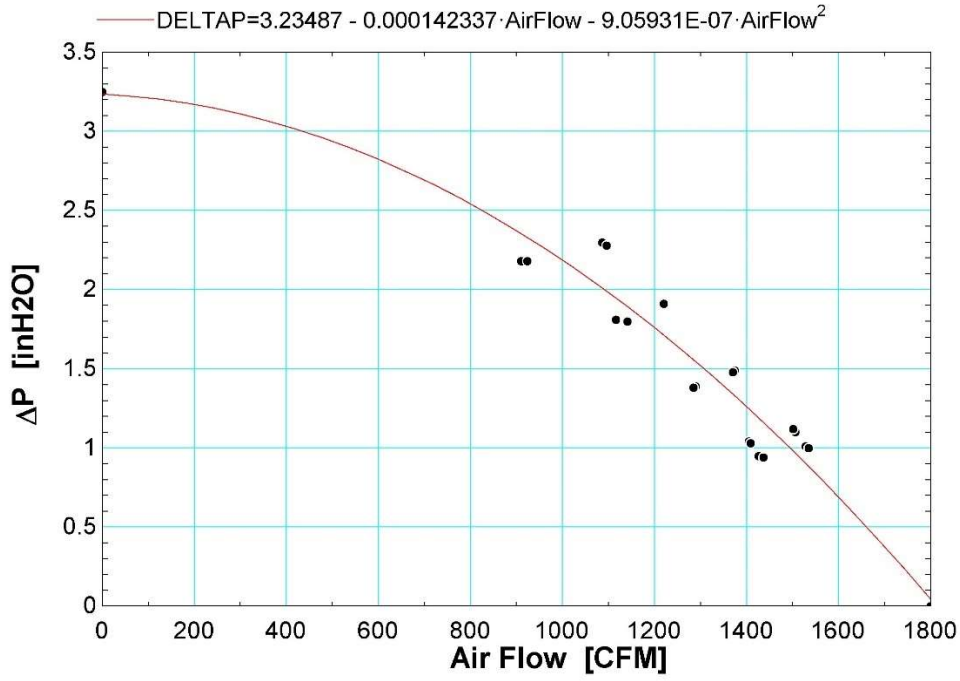

b)

Figure 4. 6. 5: a) Measured AHU1 fan curve for 3600 rpm b) Measured AHU1 fan curve for 2646 rpm

The airflow and pressure rise presented by Figure 4.6.5a and Figure 4.6.5b were then normalized by the estimated points of intersection with the x-axis and the y-axis,

respectively. This was accomplished by establishing a maximum pressure rise curve and a maximum airflow curve based off these points. The maximum pressure rise and maximum airflow curves are in Figure 4.6.6 while the resulting normalized data are shown in Figure 4.6.7.

The maximum airflow as determined by Figure 4.5.5 is:

$$F_{\max,fan} = 15.3846 + 0.675214\, f \tag{4.6.1}$$

and the maximum pressure rise is:

$$P_{\max,fan} = 2.315E^{-4}\, f + 3.601E^{-7}\, f^2 \tag{4.6.2}$$

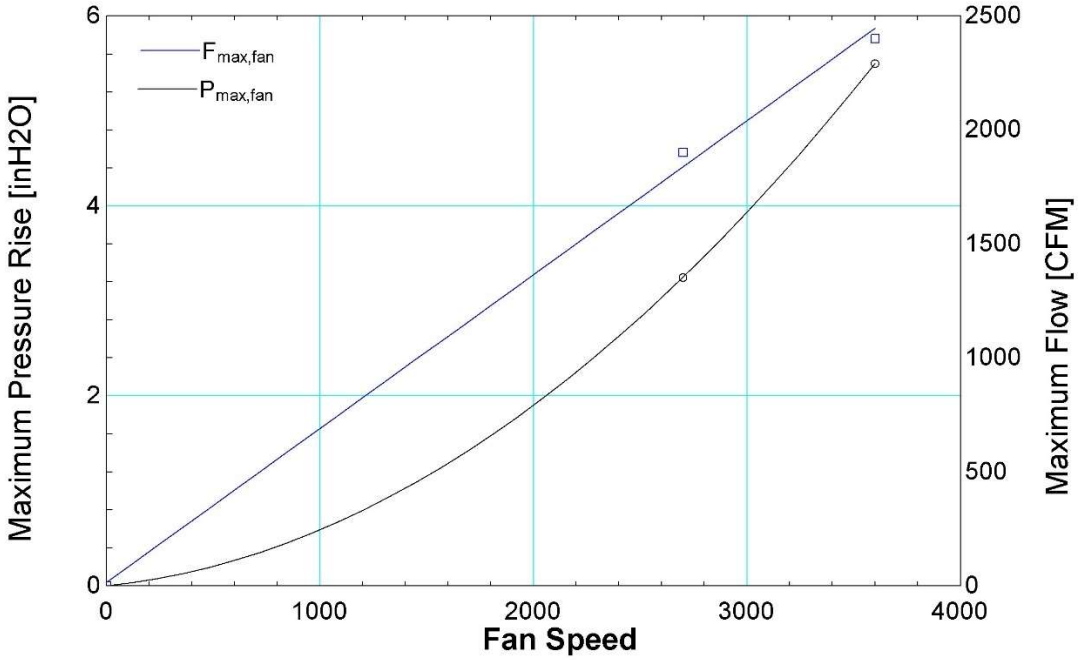

Figure 4. 6. 6: Estimated maximum airflow and pressure curves

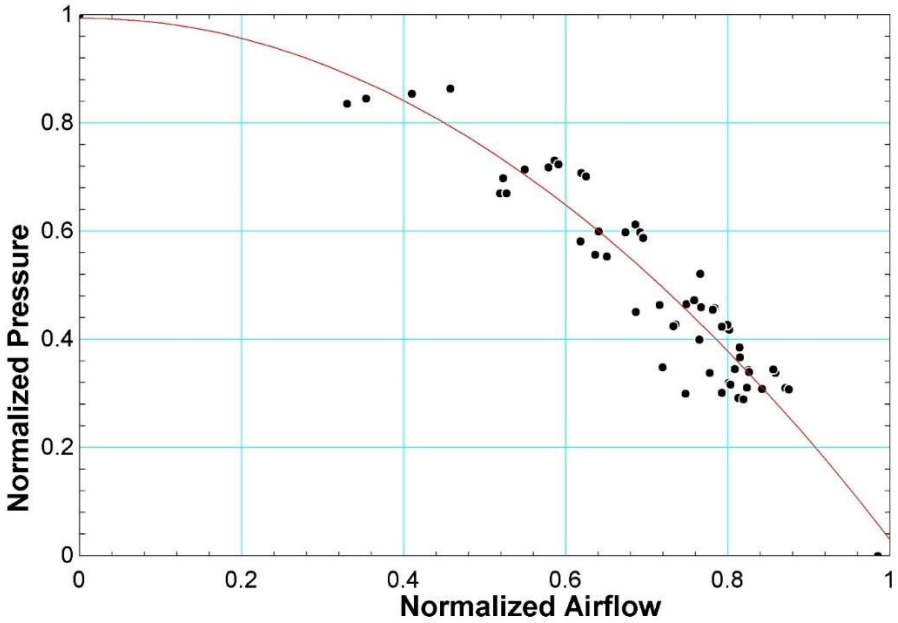

Figure 4. 6. 7: Normalization of measured fan curves

The normalized curve fit in Figure 4.6.6 is represented by:

$$\overline{P}_{fan} = 0.99 + 0.007\ \overline{F}_{fan} - 0.97\ \overline{F}_{fan}{}^{2} \tag{4.6.3}$$

Substituting these new definitions into the normalization process defined by Eqs. (4.2.3)-(4.2.4), allows these as-installed fan curves to be used within the structure of the developed model.

To ensure the revised fan curve was implemented correctly, the measured flow and the measured fan speed from the IBAL data used in the creation of the measured fan curve input to the simulation model. The model-predicted fan pressure rise was then compared to the measured fan pressure rise recorded as displayed in Figure 4.6.8.

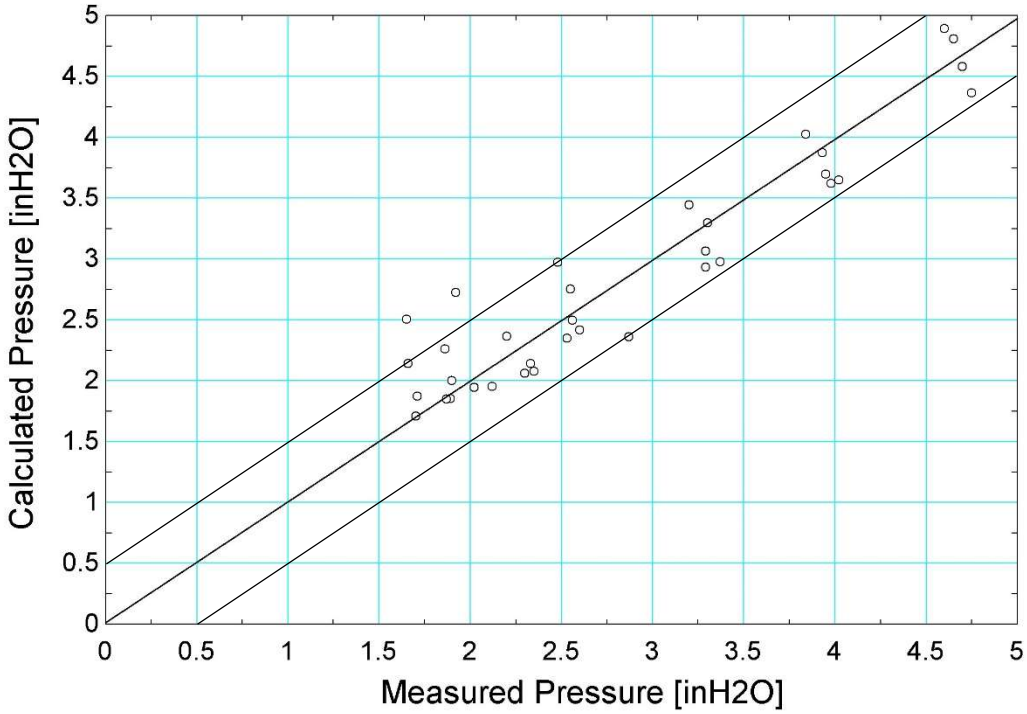

Figure 4. 6. 8: Measured pressure rise across the AHU1 fan compared to the generating data

As expected, the calculated pressure rise follows the measured data as it tends to be within 0.5 inH2O degree of accuracy. This serves as a verification that the process to transition from Figure 4.6.5 to Figure 4.6.7 is correct. To validate the new curve fit, the model was tested against a wide range of data spanning several different fan speed conditions to see how well it performs.

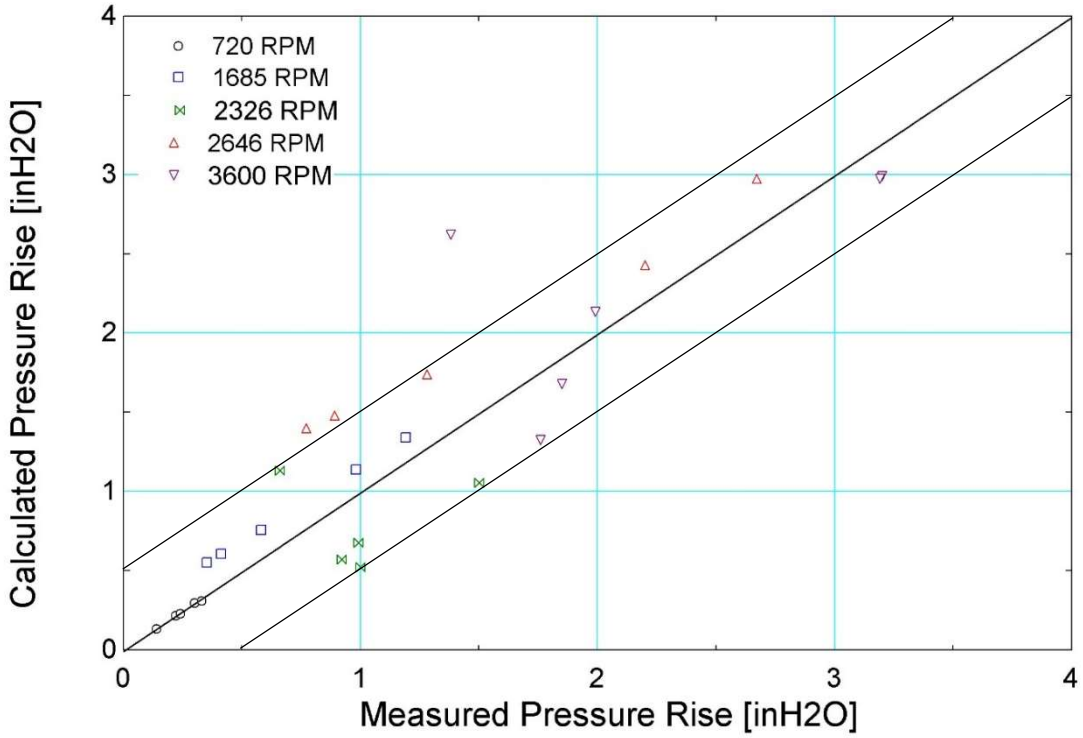

Figure 4. 6. 9: Model verification comparison

Figure 4.6.9 depicts the results of 5 different fan speeds where the airflow and pressure rise were calculated for several different system resistances for each one. For most of the data, the calculated pressure rise was within a 0.5 in of H_2O difference from the measured data with the larger deviance occurring at the higher fan speeds. The final step in the fan model verification involves comparing the new model to the manufacturer curves over the same set of measured data.

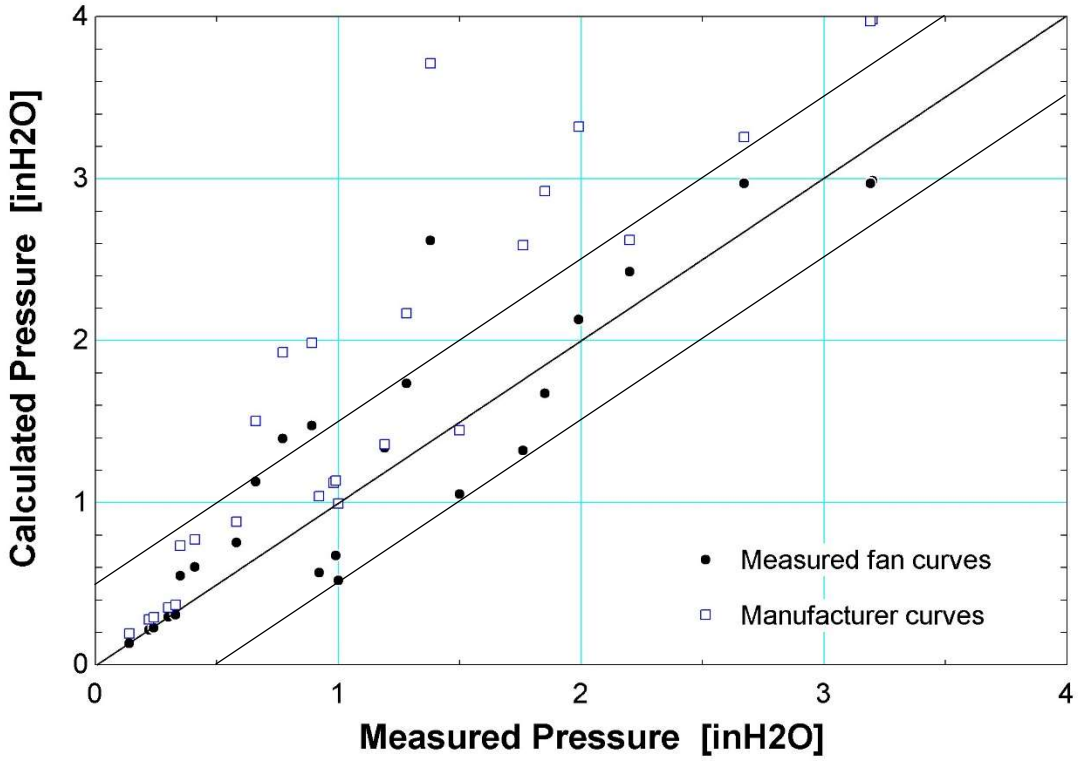

Figure 4. 6. 10: Modified fan curve compared with the manufacturer fan curve

Figure 4.6.10 overlays the calculations of the manufacturer fan curve onto the results from Figure 4.6.9. At lower fan speeds, there is little difference between the two methods. However, at higher fan speeds, the updated model performs much better relative to the manufacturer-based curves. Overall, this data shows that the modified curves capture the behavior of the IBAL to a much greater degree of accuracy than then manufacturer curves.

4.6.c Examination of System Dampers

4.6.c (i) System Dampers Introduction

With the measured fan curves quantified and verified, the error in the airflow/pressure model caused by using a manufacturer-supplied fan curve is mitigated as much as it can be. The last error to be reduced in the model is that which is caused by the damper

curves. The model derived from the manufacturer curves uses a one size fits all perspective on damper performance which is likely a large source of error as there are 5 dampers in the system each of which will behave differently from the manufacturer curves. To quantify the performance of these dampers, pressure differentials must be measured across each damper in the system over a range of flows and positions so that each damper's behavior can be characterized.

4.6.c (ii) Measured D17 Damper Curves

The first damper examined is D17, located in VAV 3. To determine the performance of this damper, flow and pressure sensors were utilized. The locations of these sensors relative to D17 are shown in Figure 4.6.11.

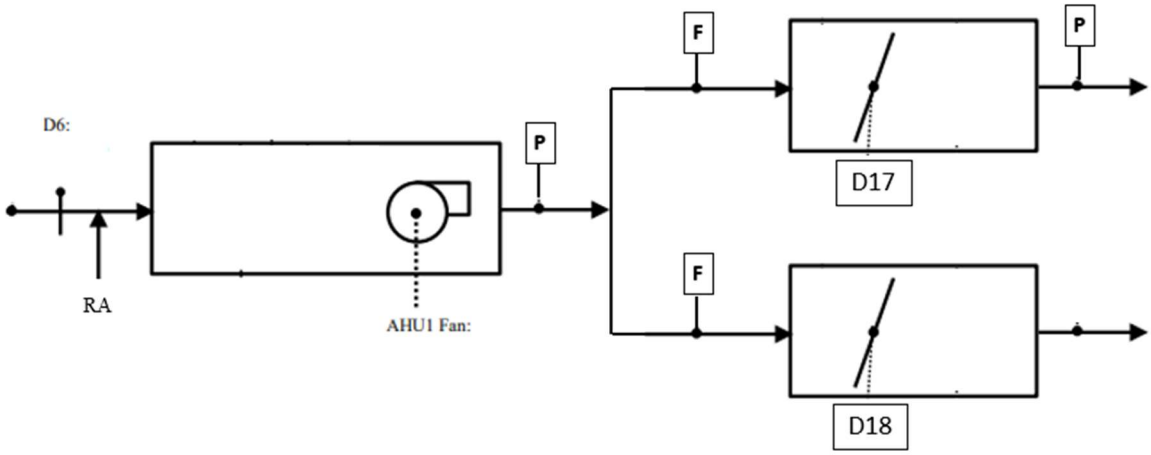

Figure 4. 6. 11: Sensor placement to measure D17 performance curve

The pressure drop across D17 was calculated by taking the difference between a temporary pressure sensor installed by NIST personnel downstream of D17 and the pressure sensor immediately downstream of the AHU1 fan. The flow across the D17 was measured by a flow meter just preceding the VAV box. Data were measured at the IBAL, where D18 was closed and D17 was incrementally closed (starting from 100% wide open and decreasing to 20% wide open). At each damper position tested, a few different fan

speeds were utilized to achieve a wide variety of flow rates across D17. The average values of airflow vs pressure drop across D17 for each position is shown in Figure 4.6.12.

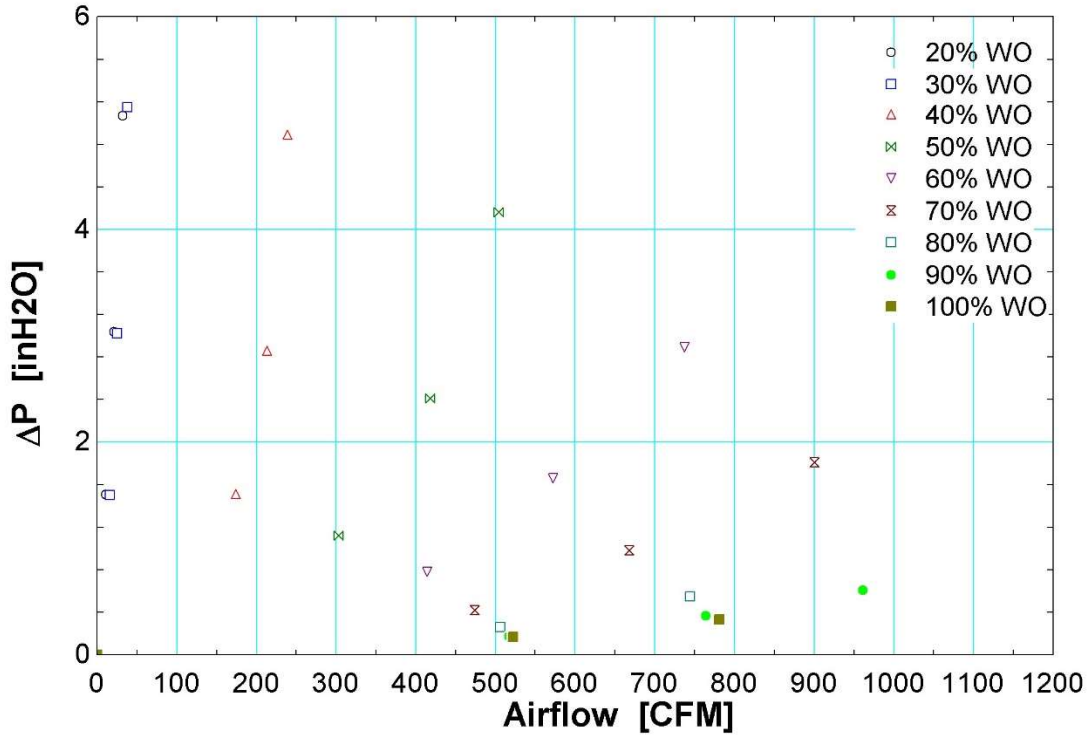

Figure 4. 6. 12: Measured performance curves for D17

For this data set, the highest flow rate at 80%WO and 100%WO resulted in a saturated pressure sensor, and thus these data were discarded in the creation of the measured damper curves. Based on Figure 4.6.12, the effective operating range of D17 is between 30 %WO - 90 %WO. This is important to note and implement into the model as the model assumes an effective damper range between 0%WO - 100%WO.

To adapt the curves from Figure 4.6.12 into something useable by the airflow/pressure model, a curve fit of the maximum airflow and pressure drop as a function of damper position was required. This was accomplished by applying a curve fit to the maximum airflow and maximum pressure drop at each damper position in the effective operating range as shown in Figure 4.6.13

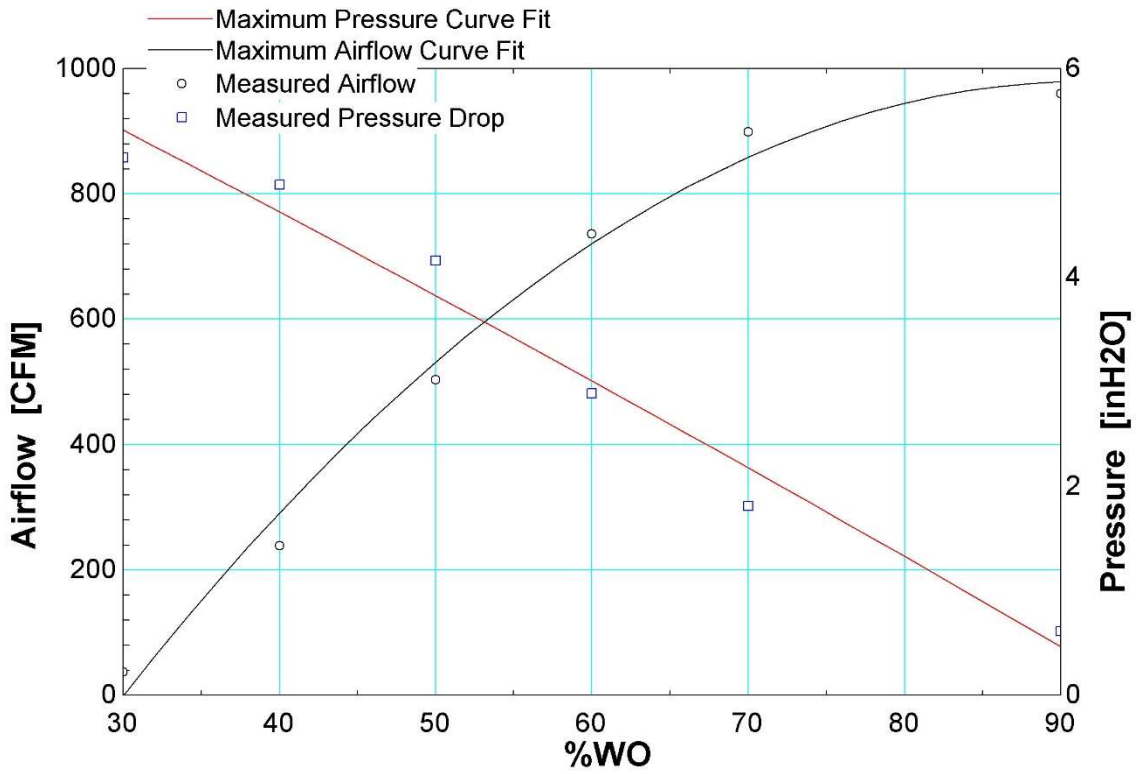

Figure 4. 6. 13: Maximum flow and maximum pressure drop as a function of D17 position

The resulting maximum airflow curves and maximum pressure drop are depicted by the following equations:

$$F_{\max,damper} = -1187.69 + 47.27\ WO - 0.21\ WO^2 \tag{4.6.4}$$

$$P_{\max,damper} = 7.67 - 7.29E^{-2}\ WO - 7.98E^{-5}\ WO^2 \tag{4.6.5}$$

The complete data set was then normalized according to Eqs. (4.2.5)-(4.2.6) using the new definitions for maximum airflow and maximum pressure drop. The result of the normalization on the D17 measured data is shown in Figure 4.6.14.

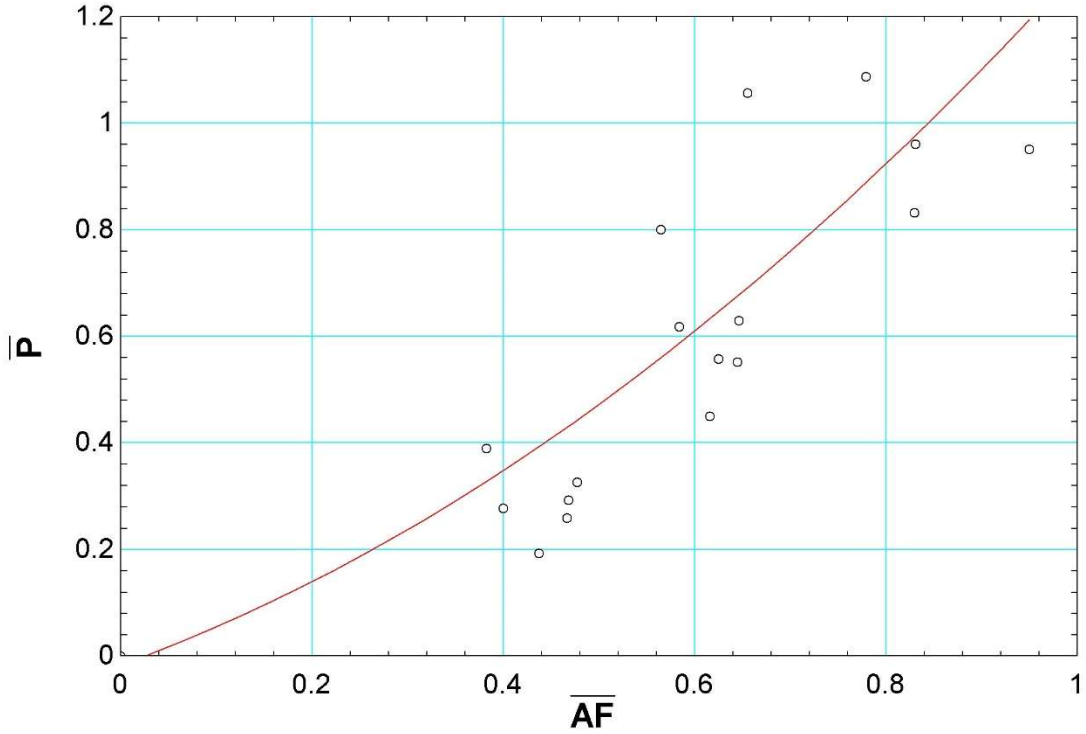

Figure 4. 6. 14: Normalized D17 performance curve

The curve fit for the normalized performance is:

$$\bar{P} = -1.69E^{-2} + 0.65\,\bar{F} + 0.66\,\bar{F}^2 \tag{4.6.6}$$

The normalized curve was then implemented and tested against both the measured pressure drop and the manufacturer curve pressure drop for the data presented in Figure 4.6.12 within the effective damper range. The results of this are shown in Figure 4.6.15.

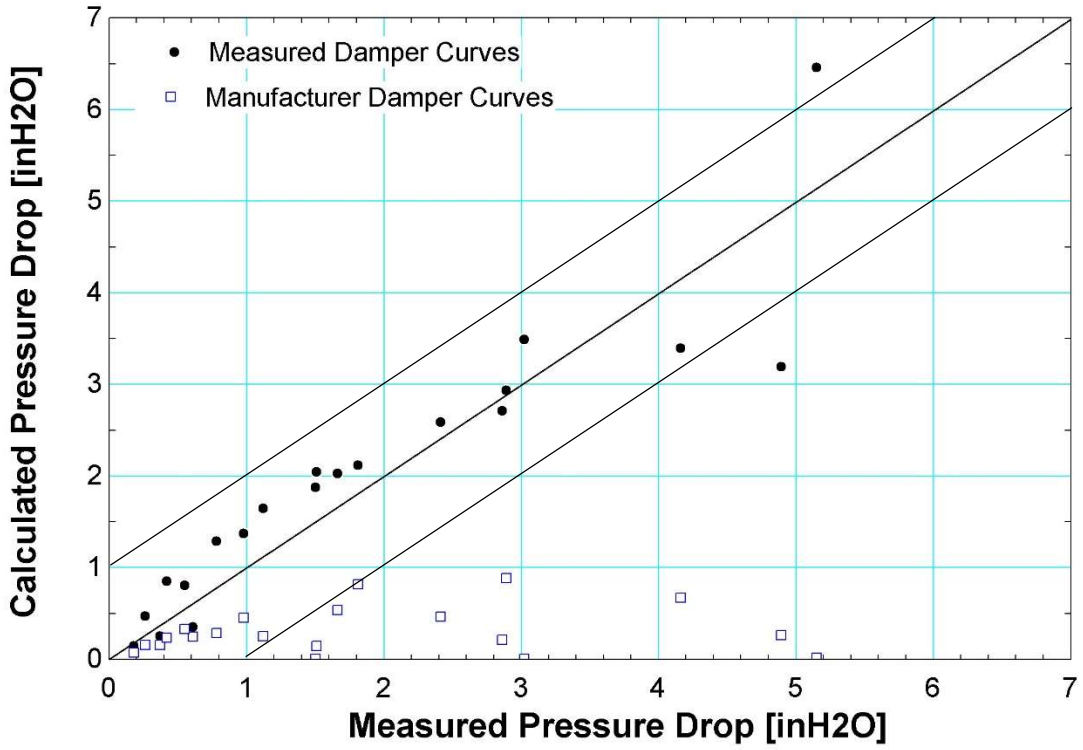

Figure 4. 6. 15: Measured D17 curve compared to data and manufacturer curve compared to data

These results show the drastic improvement in the model with the measured D17 curve. The new damper curve accurately predicts the pressure drop across the damper to within a 1 inH_2O difference relative to the data. In most scenarios this difference is closer to a 0.5 inH_2O difference. The larger differences compared to the measured damper curve occurs close to the effectively shut position (30 %WO-40 %WO) where differences up to 1.5 inH_2O are noticed.

4.6.c (iii) Measured D10 Damper Curves

The second damper analyzed was D10 which corresponds with the damper located after the zone and immediately upstream of the exhaust fan. To measure a pressure differential across D10, the sensor configuration shown in Figure 4.6.16 was utilized.

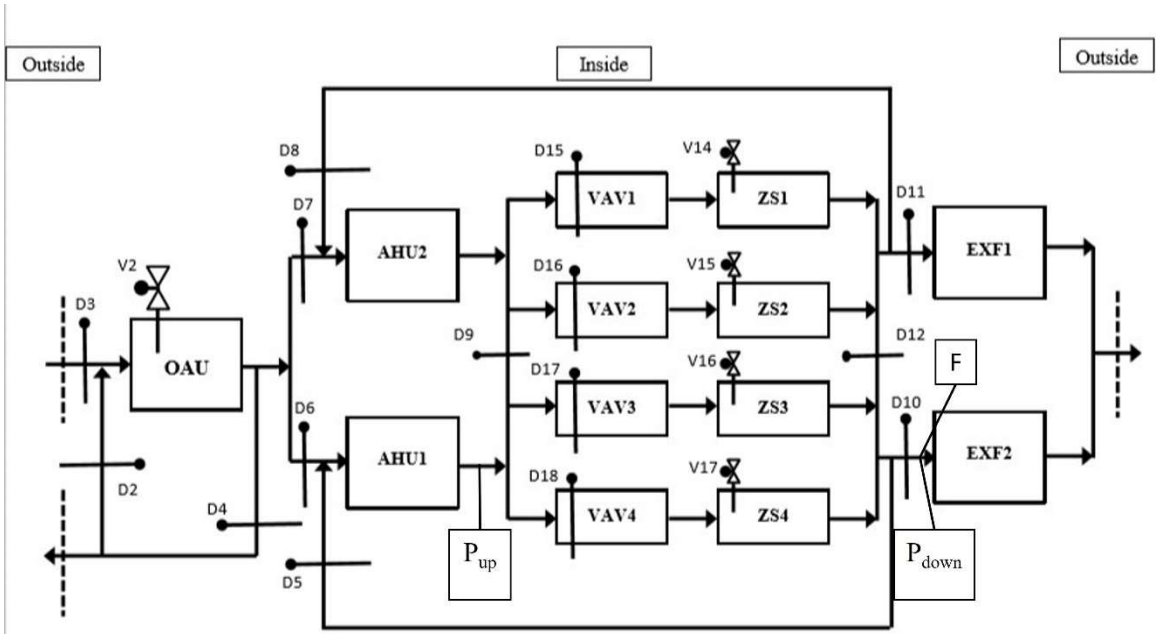

Figure 4. 6. 16: Sensors used to measure the performance of D10

When collecting data for D10, D5 was fully closed while D6, D17, and D18 were fully open to minimize the error associated with the pressure drop across those dampers. P_{up} for these measurements is the pressure transducer immediately downstream of the AHU1 fan while P_{down} is the pressure sensor upstream of the EXF2 component. The flow measurement for D10 is also located upstream of EXF2. The data collected to characterize the damper consisted of measuring the pressure drop defined by $P_{down} - P_{up}$ along with the flow at a range of 5 different damper inputs ranging between 20%WO-100%WO. At each damper position 4 different AHU1 fan speeds from 30 Hz-60 Hz were utilized to generate various flow rates for each damper position. These measured performance curves are shown in Figure 4.6.17

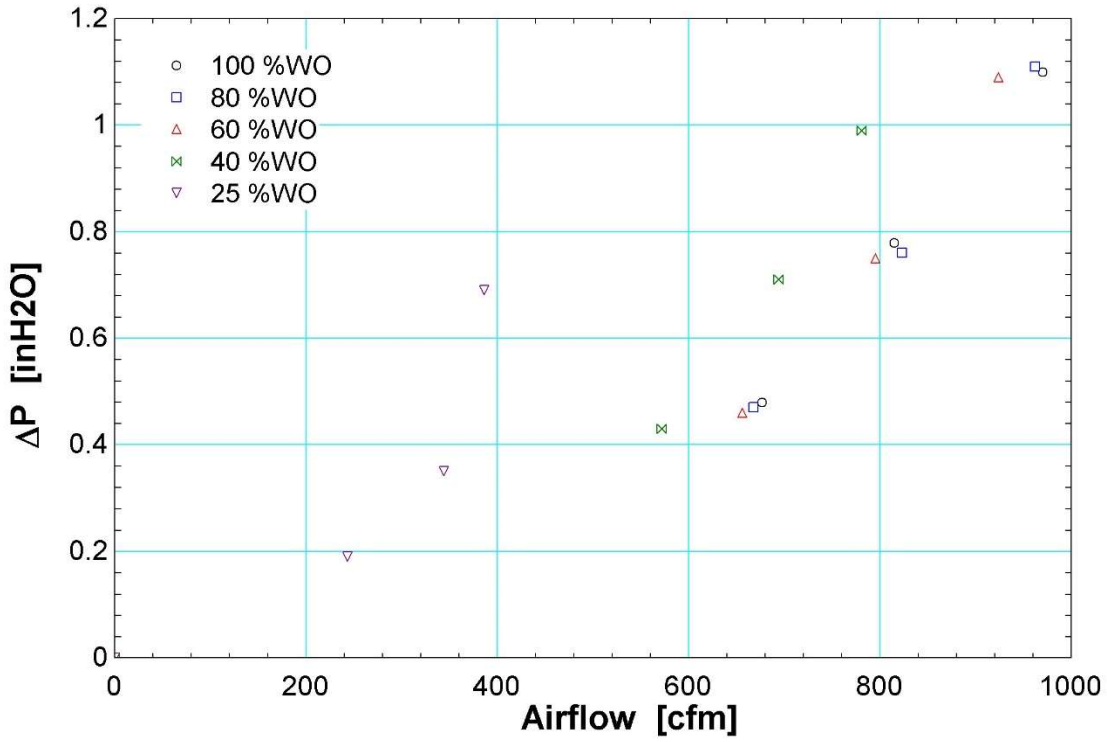

Figure 4. 6. 17: Measured performance curves for D10

This data was noticeably less indicative of a damper curve when compared to the measured curves for D17 shown in Figure 4.6.12. This is in part due to a large section of data being disregarded as P_{down} became saturated. Based on this data set, around 60 %WO and greater, there is no discernable difference in damper performance. The minimum range of damper performance cannot be determined from this data set as the minimum damper position has not been reached. The reason why smaller damper positions were not tested is because the NIST technician performing this test was ensuring a flow path for the air to leave the system. As a result, D10 was not incremented to a completely closed position. Overall, more testing needs to be done on this damper with a focus on the range of effective damper operation to better characterize the actual damper performance. With the data presented in Figure 4.6.17, the useful data for generating the curves appears to span from 25 %WO-60%WO. Using just the three data

series presented above can lead to inaccurate maximum pressure drop and maximum airflow curves and result in a model that does not encapsulate the damper performance. As the current damper curves utilized by the model are very inaccurate, the performance curves for D10 determined using the few damper curves within the effective operating range shown in Figure 4.6.17. The maximum flow and maximum pressure drop curves are depicted by Figure 4.6.18.

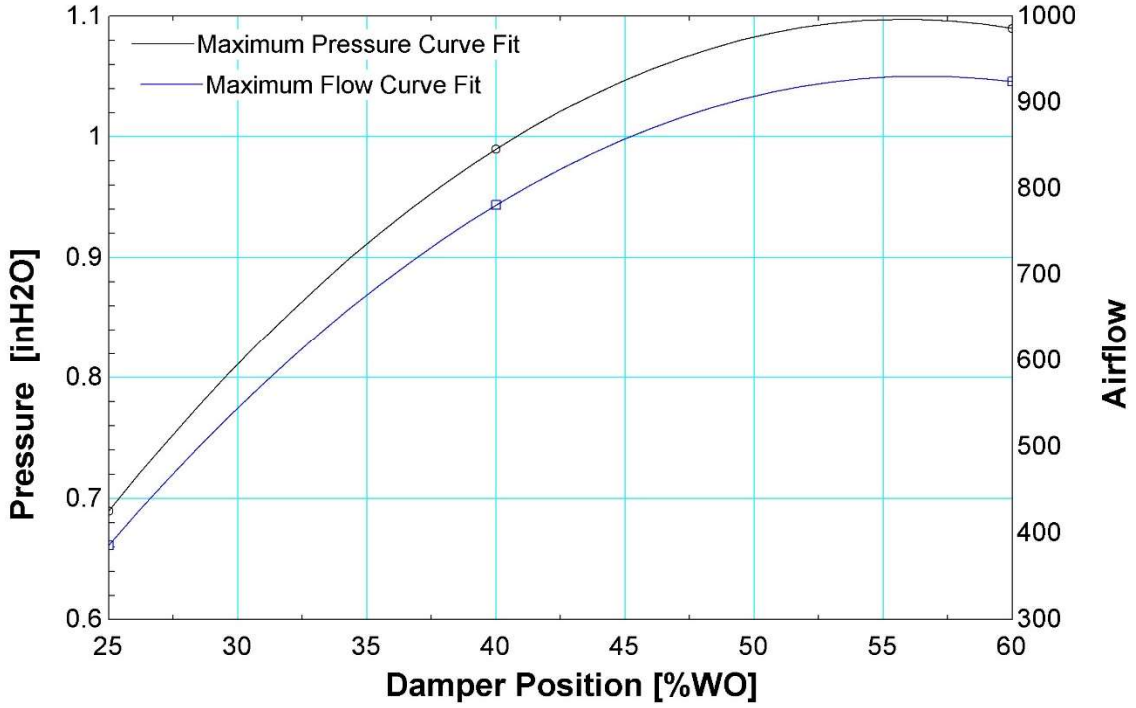

Figure 4. 6. 18: Maximum flow and maximum pressure drop as a function of D10

The equations representing the curve fits shown in Figure 4.6.18 are:

$$P_{\max,damper} = -0.24 + 4.79E^{-2}\ WO - 4.29E^{-4}\ WO^2 \tag{4.6.7}$$

$$F_{\max,damper} = -820.43 + 61.96\ WO - 0.55\ WO^2 \tag{4.6.8}$$

Eqs. (4.6.7)-(4.6.8) were then used to normalize the data within the effective damper range. The result of this is in Figure 4.6.19.

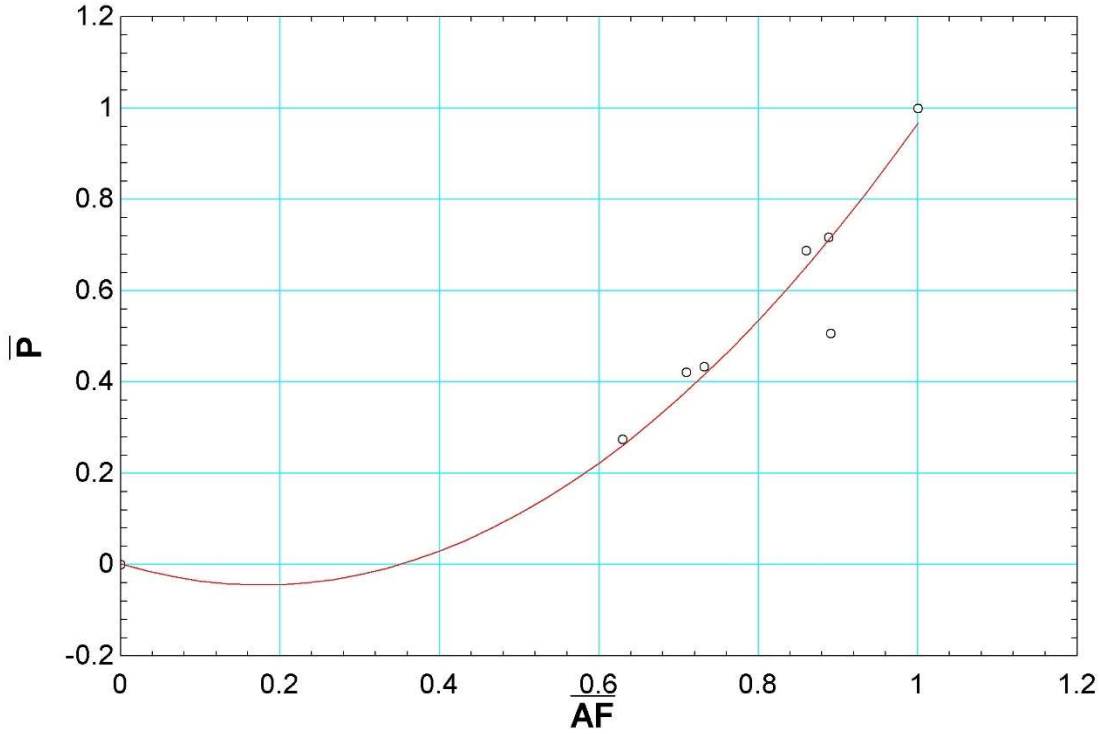

Figure 4. 6. 19: Normalized curve fit for D10

This curve fit is depicted by the equation:

$$\overline{P} = 1.69E^{-3} - 0.53\,\overline{F} + 1.49\,\overline{F}^{2} \tag{4.6.9}$$

The normalized curve and the manufacturer curve were then tested against the measured data from Figure 4.6.17. The results of this are displayed in Figure 4.6.20.

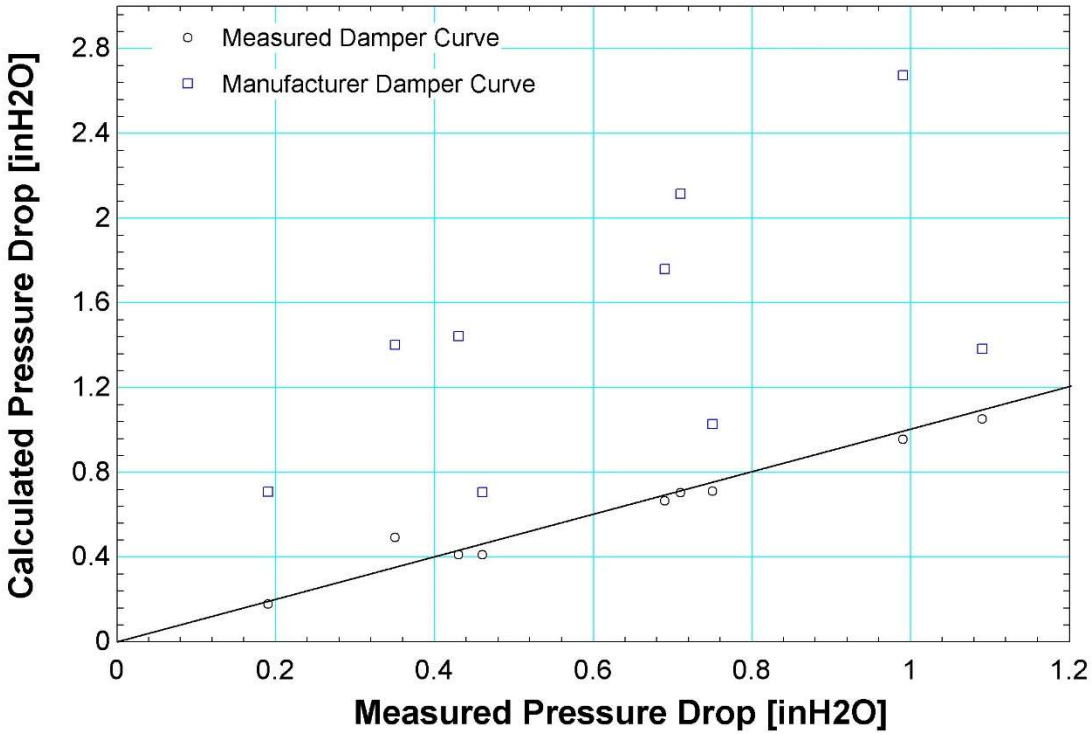

Figure 4. 6. 20: Measured D10 performance compared to data and manufacturer performance compared to data

Figure 4.6.20 shows that the measured damper curves perform markedly better than the manufacturer curves relative to the available measured data. If possible, further tests should be run at damper positions below 25%WO to provide the most accurate representation possible across all damper positions.

4.6.c (iv) Measured D5 Curves

The third damper analyzed is the RA damper (D5). To quantify the pressure drop across the damper, the instrumentation shown in Figure 4.6.21 was used.

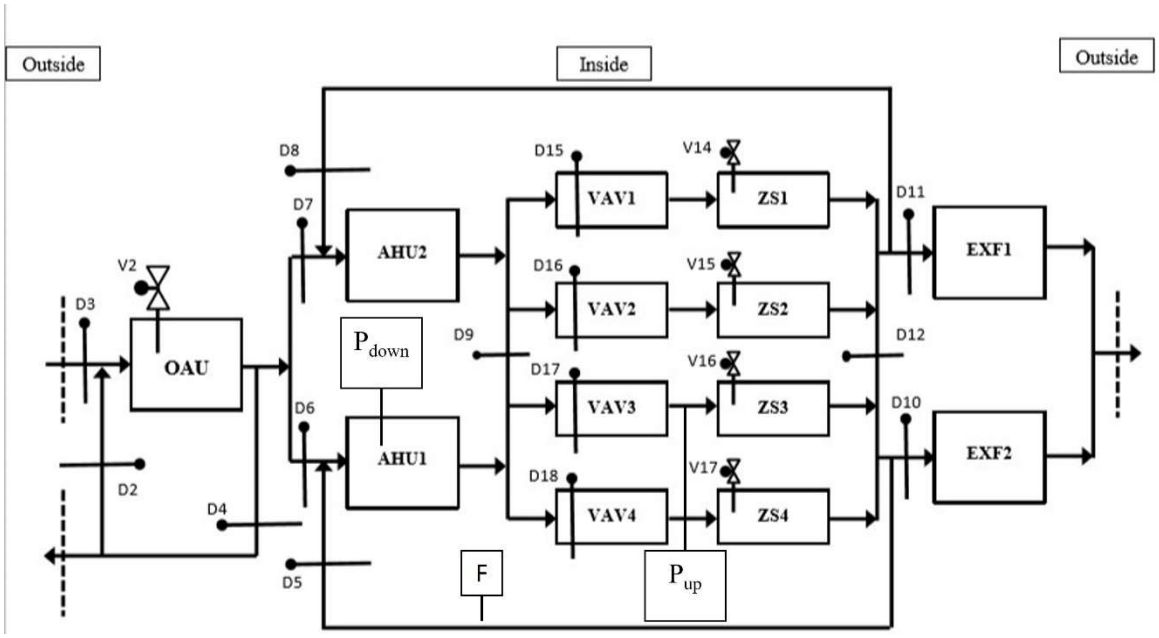

Figure 4. 6. 21: Sensors used to measure the performance of D5

In terms of pressure sensors, P_{up} is the temporary pressure sensor installed by NIST personnel downstream of VAV3 and P_{down} is the upstream pressure sensor located in AHU1. The flow measurement across D5 is in the RA branch. When collecting data for D5, D17 and D18 were fully opened while D6 and D10 were fully closed. The data collected to characterize the damper consisted of measuring the pressure drop defined by $P_{down} - P_{up}$ along with the flow at a range of 6 different damper inputs ranging between 0 %WO-90%WO. At each damper position 4 different AHU1 fan speeds from 30 Hz-60 Hz were utilized to generate various flow rates for each damper position. The measured performance for this damper is shown in Figure 4.6.22

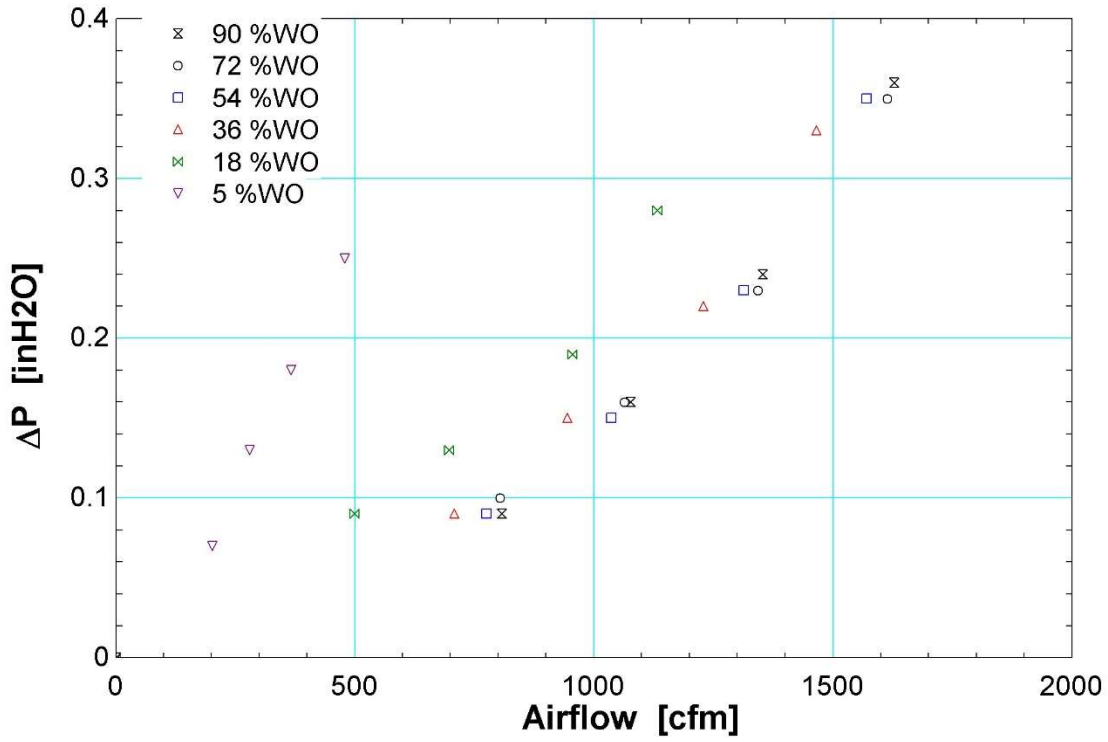

Figure 4. 6. 22: Measured performance curves for D5

The first noticeable feature in the Figure 4.6.22 is that the effective range of operation for D5 is approximately between 5% WO-54 %WO as evidenced by the data for 54%, 72%, and 90% WO positions all being clustered together. The maximum pressure drop and maximum flow curve fits based on this data are depicted in Figure 4.6.23.

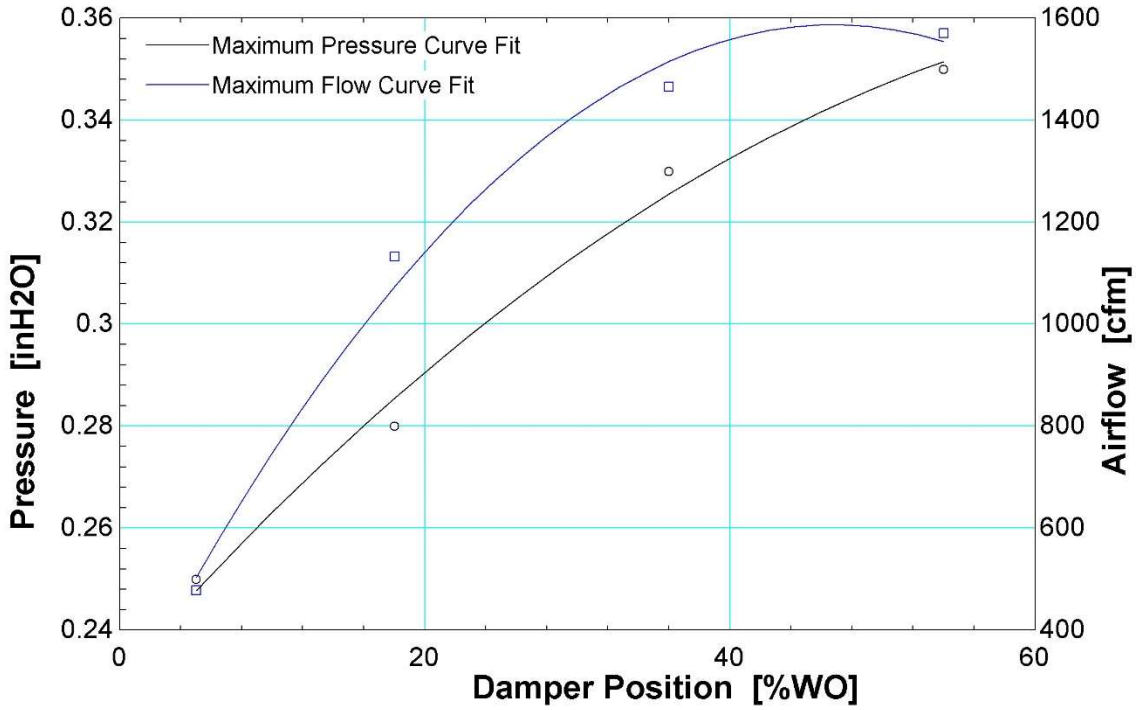

Figure 4. 6. 23: Maximum flow and maximum pressure drop as a function of D5

The resulting maximum airflow curves and maximum pressure drop are depicted by the following equations:

$$F_{\max,damper} = 228.37 + 58.09\ WO - 0.62\ WO^2 \tag{4.6.10}$$

$$P_{\max,damper} = 0.23 + 3.40E^{-3}\ WO - 2.18E^{-5}\ WO^2 \tag{4.6.11}$$

The data set presented by Figure 4.6.22 was normalized according to Eqs. (4.6.10)-(4.6.11) and a curve fit was applied. The result of this is depicted in Figure 4.6.24.

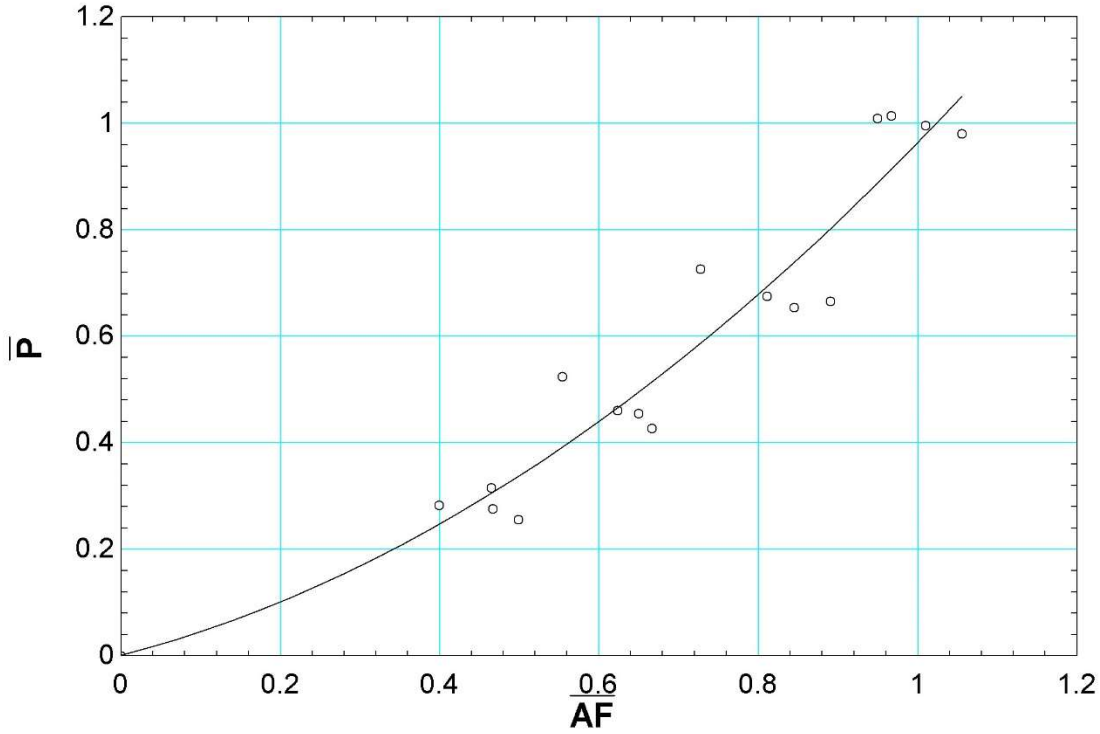

Figure 4. 6. 24: Normalized curve fit for D5 measured data

The equation that represents this curve fit is depicted by:

$$\overline{P} = 1.04E^{-3} + 0.39\ \overline{F} + 0.58\ \overline{F}^2 \qquad (4.6.12)$$

The normalized curve was then implemented and tested against the measured pressure drop from the data shown in Figure 4.6.22 within the effective damper range. The results of this are shown in Figure 4.6.25.

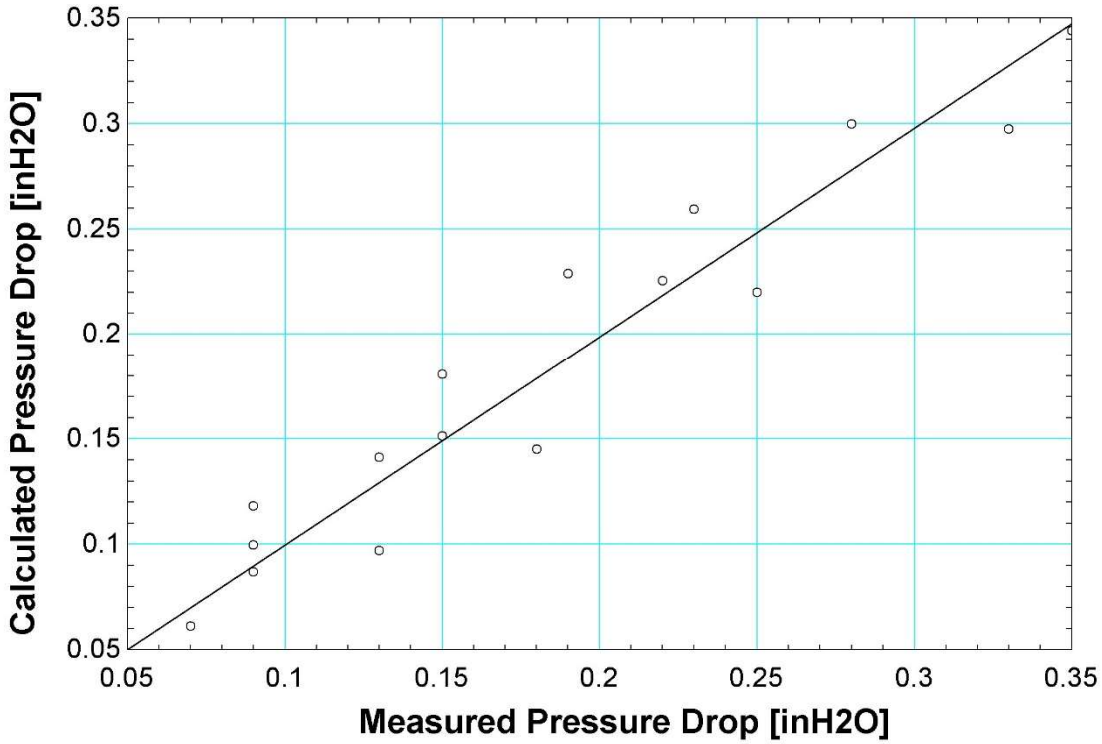

Figure 4. 6. 25: Measured D5 performance curves compared to the measured data

Overall, the measured performance curve for D5 is very consistent. The only question that remains about this damper is whether the scale of the measured pressure drop is reliable. It seems that the amount of pressure drop measured across the damper is on a relatively small scale considering the wide range of airflows recorded. This could indicate that D5 is rather large or that there may be some issues with the pressure measurements. Thus, these potential explanations will need to be explored in the future to validate the derivation of D5 above.

4.6.c (v) Measured Supply Air Damper Curves

The final damper characterization that was explored involved looking at the pressure drop versus flow across the supply air damper. The AHU2 supply air damper (D7) was examined as it was more convenient for the NIST technician, and the damper is identical to D6. The sensor layout used in this analysis is depicted in Figure 4.6.26.

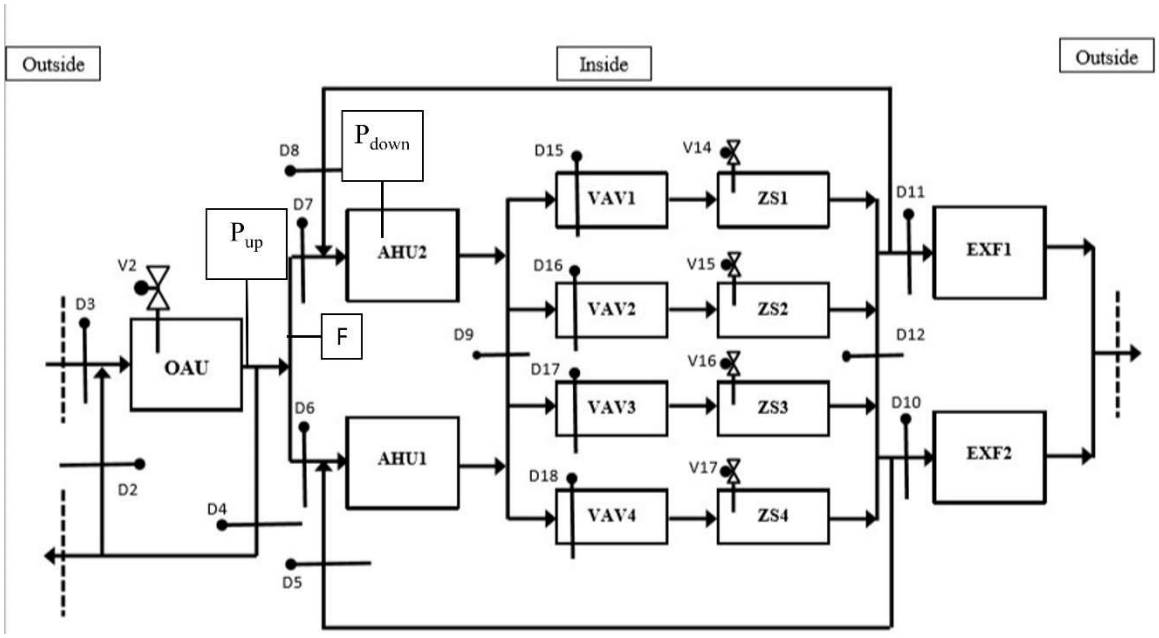

Figure 4. 6. 26: Sensors used to measure the performance of D7

P_{up} is measured by the pressure transducer located downstream of the OAU fan while P_{down} is measured upstream of the fan located in AHU2. The measurement for flow across D7 is located upstream of the damper. Measured data was collected at 10 damper positions ranging from 5 %WO-75 %WO. At each damper position, 3 OAU fan speeds were utilized to generate a range of airflow values. The results of these measurements are depicted in Figure 4.6.27.

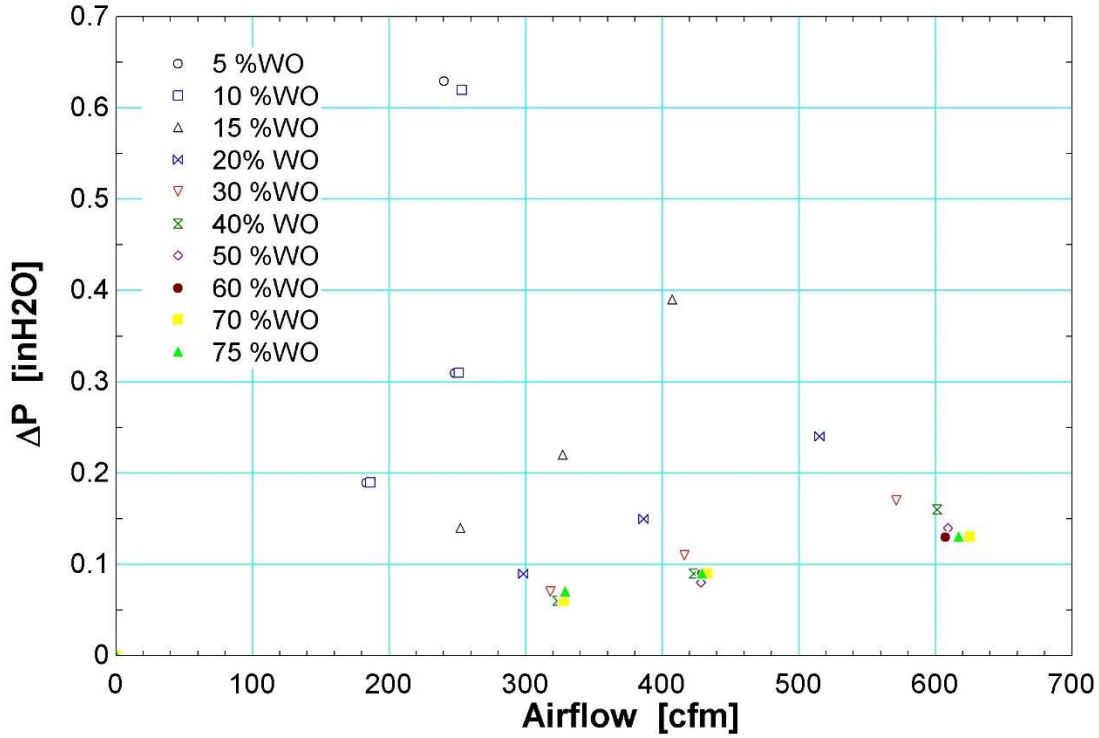

Figure 4. 6. 27: Measured performance curves for D7

Based on the measured data, the effective operating range of D7 appears to range between 5%WO - 40%WO. Above this range, there is a negligible difference between the performance curves. The curve fits for the maximum flow and maximum pressure rise based on Figure 4.6.27 is shown in Figure 4.6.28.

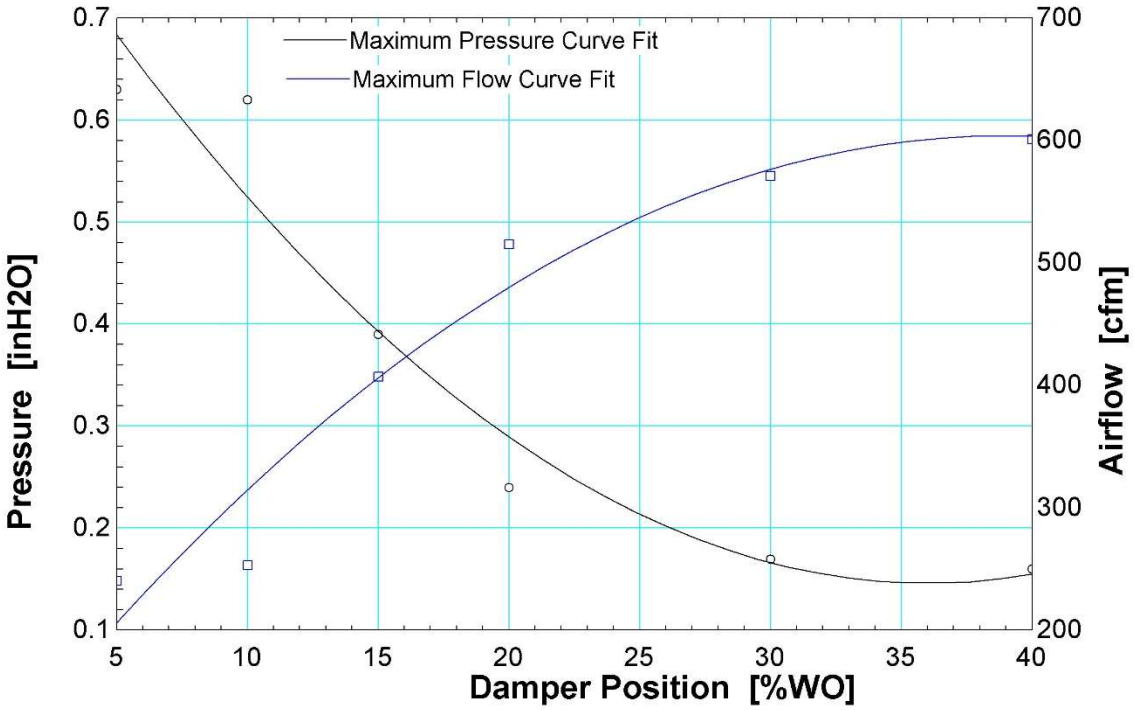

Figure 4. 6. 28: Maximum flow and maximum pressure drop as a function of D7 position

The equations of the curve fits above are:

$$F_{\max,damper} = 79.88 + 26.95\ WO - 0.35\ WO^2 \tag{4.6.13}$$

$$P_{\max,damper} = 0.87 - 4.03E^{-2}\ WO + 5.59E^{-4}\ WO^2 \tag{4.6.14}$$

Using the curve fits from above, measured data from Figure 4.6.27 was normalized as shown in Figure 4.6.29.

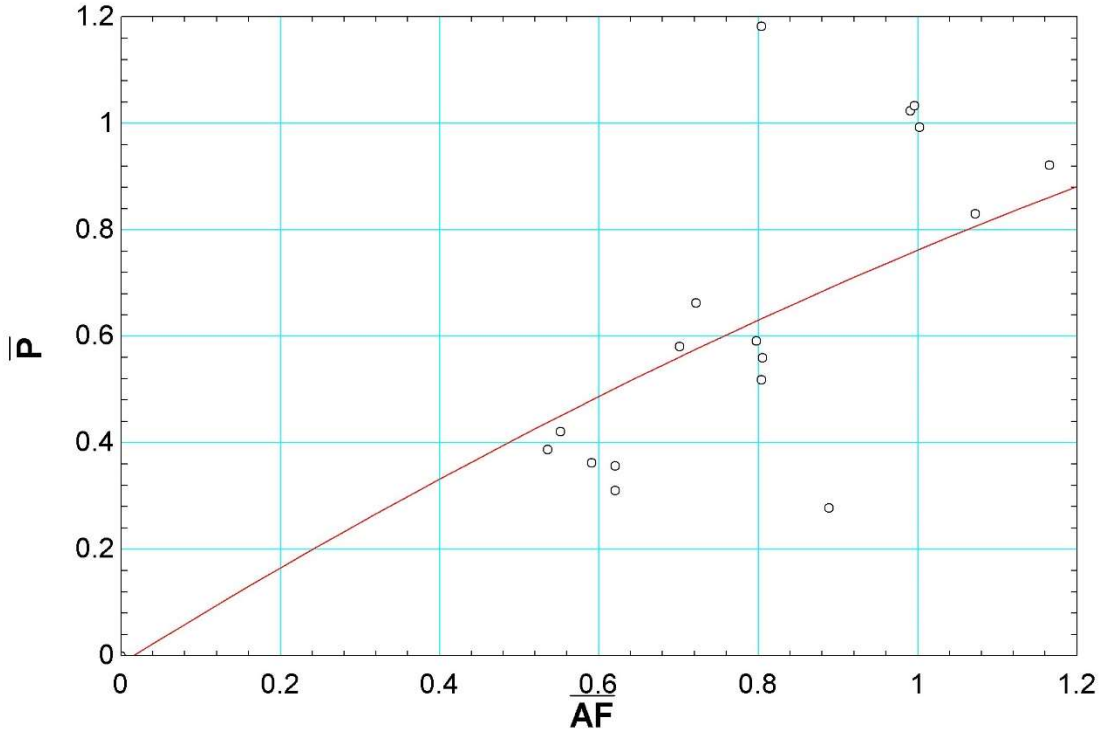

Figure 4. 6. 29: Normalized curve fit for D7 measured data

The normalized curve fit is expressed as:

$$\bar{P} = -1.42E^{-2} + 0.92\,\bar{F} - 0.15\,\bar{F}^2 \qquad (4.6.15)$$

This curve was then utilized in conjunction with the derived maximum airflow and maximum pressure curves to compare the measured fan curve performance to the measured data and is depicted in Figure 4.6.30a. Additionally, the manufacturer curve performance at the same airflow and damper position inputs is depicted in Figure 4.6.30b.

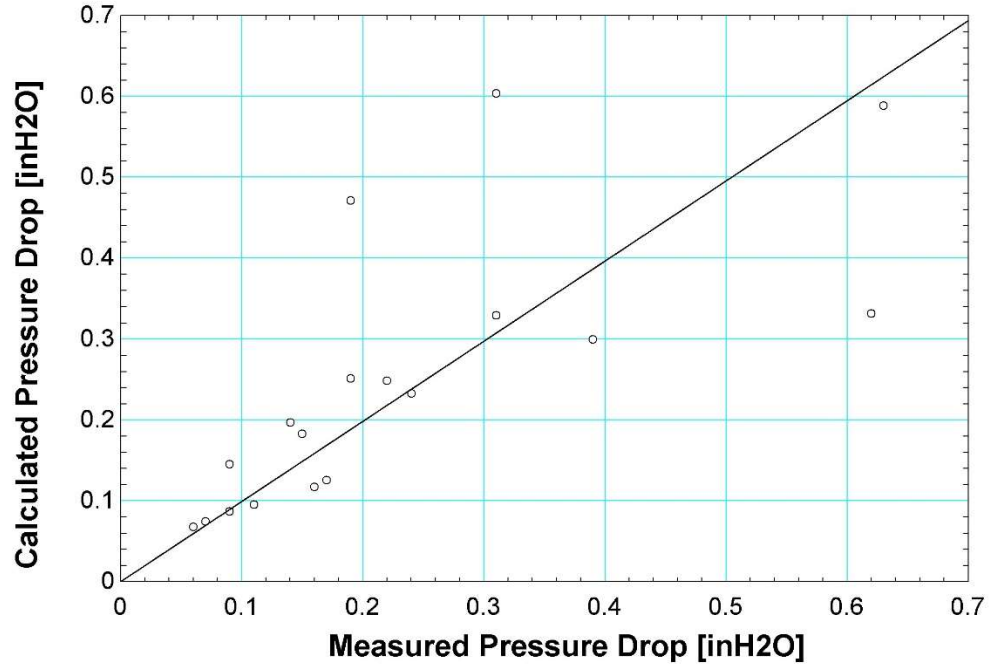

a)

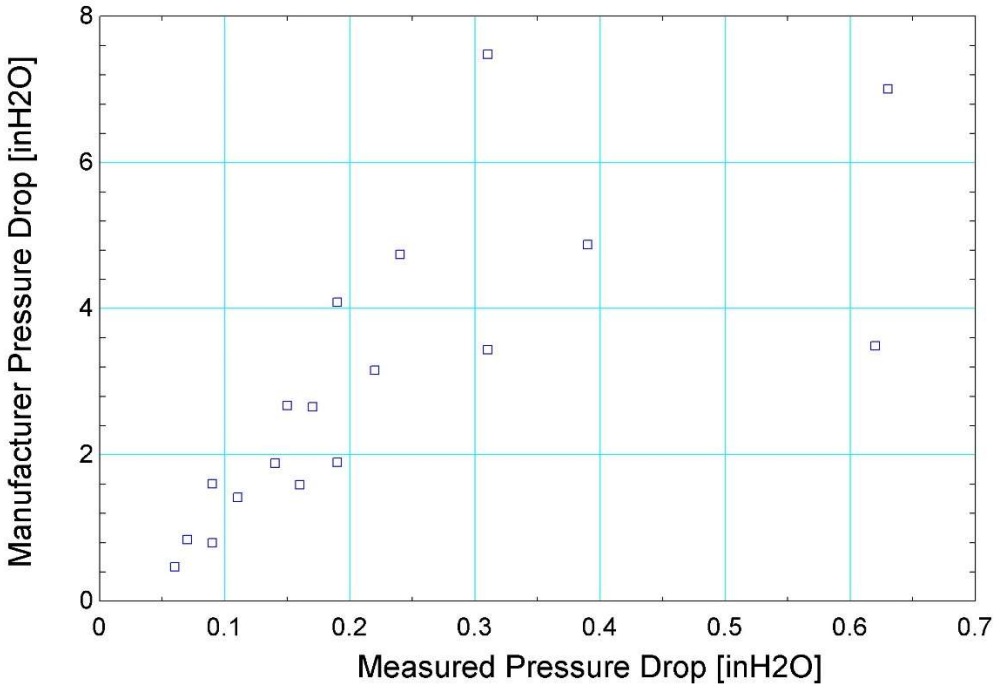

b)

Figure 4. 6. 30: a) Measured D7 performance curves compared to measured data b) Manufacturer performance curves compared to measured data

Figure 4.6.30a does a much better job of capturing the pressure drop across D7 as compared to the manufacturer performance curves. While the initial results are promising, future work may be needed to confirm performance at higher flow rates. The flow rates used in these tests were relatively low to avoid saturation of the OAU pressure sensor. Figure 4.6.30b emphasizes the importance of developing accurate damper curves as the measured data seems to show starkly different results in comparison.

CHAPTER V

Baseline Controllers

5.1 Introduction

The final aspect towards developing a self-contained model that can operate independent of direct human input, is the creation of controllers to generate signals that can independently manipulate components within the IBAL in a manner that resembles modern control methods and those incorporated into the actual IBAL system itself. To accomplish this, three independent controllers were developed to adjust various aspects of the IBAL model. One controller is responsible for opening and closing the VAV dampers along with activating the reheat coils. The second controller is responsible for adjusting the AHU fan speed to provide proper airflow. The third and final controller simulates the throttling of the cooling coil valve, determining how much coolant flows through the coil. After this baseline control system is implemented, it will provide a framework to allow updated control schemes to be implemented into the model with ease. So, while the baseline controllers may not actually be used in their initial state in IBAL testing, the ability to adapt and adjust the controllers demonstrates the feasibility of future iterations of the controller models.

5.2 VAV Controller

The first controller is responsible for adjusting air flow through the VAV boxes based upon the difference between the setpoint temperature for the respective zone and the

actual temperature of the air exiting the zone. Figure 5.2.1 shows the logic sequences that are implemented by the VAV controller model.

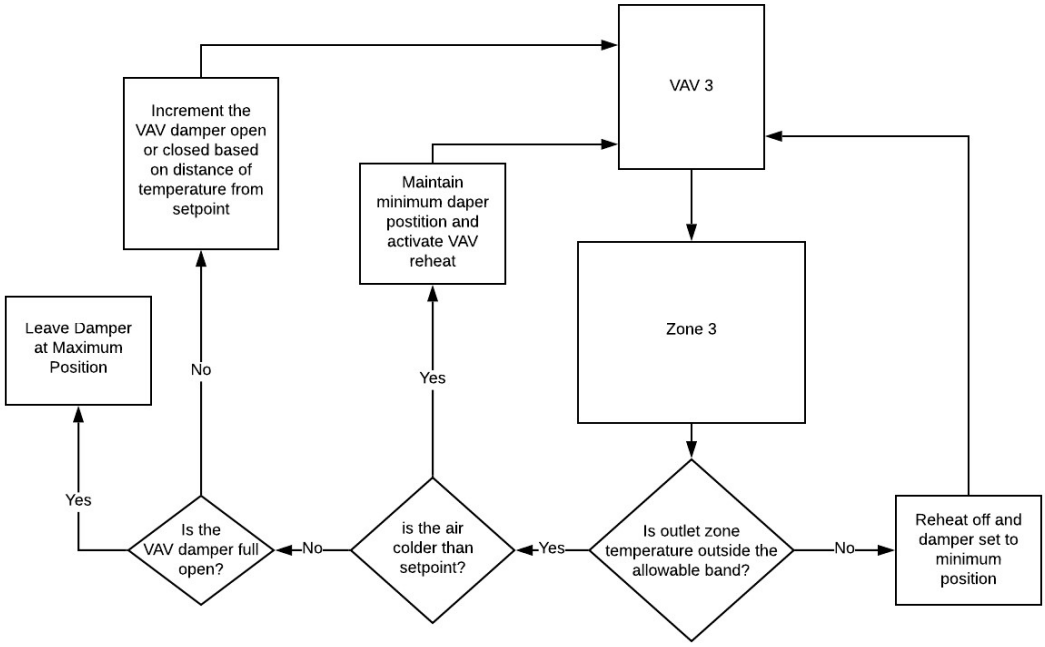

Figure 5. 2. 1: VAV Control Logic Sequence

The internal calculation begins by calculating the temperature difference according to:

$$T_{diff} = T_{zone} - \left(T_{set} + tol\right) \tag{5.2.1}$$

where T_{diff} is the temperature difference, T_{zone} is the temperature of the air leaving the zone, T_{set} is the setpoint temperature, and tol is the temperature dead band that the model allows. The model then uses a flag (sig) that indicates whether to use logic corresponding to heating or cooling. By default, $sig = 0$ at the start of the first time step. At the start of future time steps, *sig* is set equal to the previous value at the end of the function call that is stored by the model. When $sig = 0$ at the start of a time step, that means the model in the previous time step operated under a cooling mode. Thus, the

model first checks to see if the temperature difference still corresponds to that of a cooling situation. The first condition checked is:

$$T_{diff} \geq T_{diff,high} \tag{5.2.2}$$

where $T_{diff,high}$ is a user input to the controller that determines at what temperature difference above setpoint the VAV damper will be fully open. If the inequality is true, then T_{zone} must be outside of the maximum range of proportional control and therefore the damper position (D) is set to its fully open position. If this inequality is false, the following condition is checked:

$$T_{zone} \geq T_{set} + tol \tag{5.2.3}$$

The purpose of this inequality is to determine if T_{zone} lies beyond the upper end of the allowable range of temperature. If true, then the damper position, D , predicted using the following equations:

$$m = \frac{\left(T_{diff,high}\right)}{\left(D_{high} - D_{low}\right)} \tag{5.2.4}$$

$$b = -mD_{low} \tag{5.2.5}$$

$$D = \frac{T_{diff} - b}{m} \tag{5.2.6}$$

where Eq. (5.2.4) corresponds to the slope determined by the maxima and minima of both temperature difference and damper position, and Eq. (5.2.5) is the intercept of this line. Thus, Eq. (5.2.6) yields a proportional damper position between D_{high} and D_{low} based on the deviation from T_{set} that T_{zone} is. If neither Ineq. (5.2.2) or Ineq. (5.2.3) are true then no

cooling is required and the damper is set to D_{low}. Finally, the controller checks to see if the zone is too cold.

$$T_{zone} \leq T_{set} - tol \tag{5.2.7}$$

Ineq. (5.2.7) is used to determine if the zone temperature lies below the lower temperature tolerance. If false, then the zone is in the desired comfort range and no changes are made in the component. If true, the zone temperature must be too cold. To address this, the controller determines how far from setpoint the temperature is and proportionally generates the flag sig which is utilized by the reheat coil to determine how the degree to which it is energized. The value of *sig* is determined by the following equations:

$$m = -\frac{1}{T_{diff,high}} \tag{5.2.8}$$

$$b = -m\ \left(\mathrm{T}_{set} - tol\right) \tag{5.2.9}$$

$$sig = m\ T_{zone} + b \tag{5.2.10}$$

The result of these equations is a signal that can range from 0 to 1 that is proportional to how far away from the setpoint temperature the zone is. The reheat coil would then multiply its maximum power by *sig* to determine the energy supplied by the coil.

All the previous logic is only utilized if $sig = 0$ at the start of the time step. If the flag $sig > 0$ then the system must have been in heating mode in the previous time step. In these situations, the process for determining the output to the VAV is much simpler. Based on the above logic, the damper position is set at its minimum position (D_{low}) for all heating mode operation. A final inequality is used to determine the whether the system should remain in heating mode:

$$T_{zone} \geq T_{set} - \frac{tol}{2} \tag{5.2.11}$$

Ineq. (5.2.11) is used to determine whether the temperature of the zone has reached a point halfway between the setpoint and the lower end of the allowable temperatures. If true, *sig* is set to zero, as heating is no longer required. This is done to prevent the heater from turning on and off in rapid succession. Otherwise, no changes are made to *sig* . Finally, at the end of every timestep, *sig* is stored so that it can be used to determine the starting mode for the next timestep.

To verify that this controller behaves as expected, a test was developed in which the zone temperature varies with time as shown in Figure 5.2.2. In this test, the controller parameters were set as: $T_{set} = 20\,°\text{C}$, $T_{diff,high} = 5\,°\text{C}$, $D_{low} = 20\,\%\text{WO}$, $D_{high} = 100\%\text{WO}$, and $tol = 1\,°\text{C}$. The controller response based on this input is shown in Figure 5.2.3.

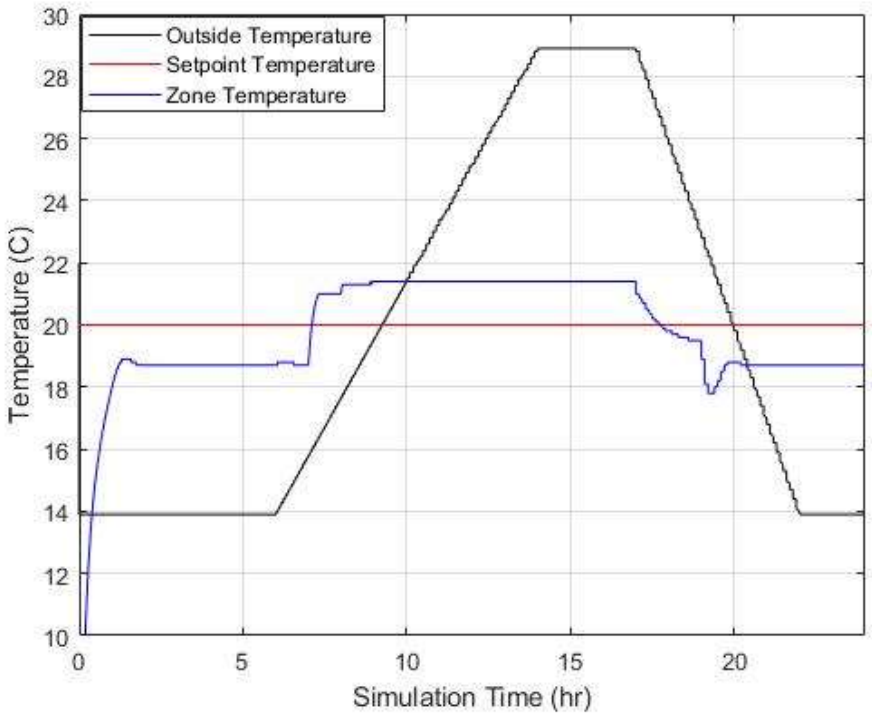

Figure 5. 2. 2: Outside, zone temperature, and setpoint temperature as a function of time

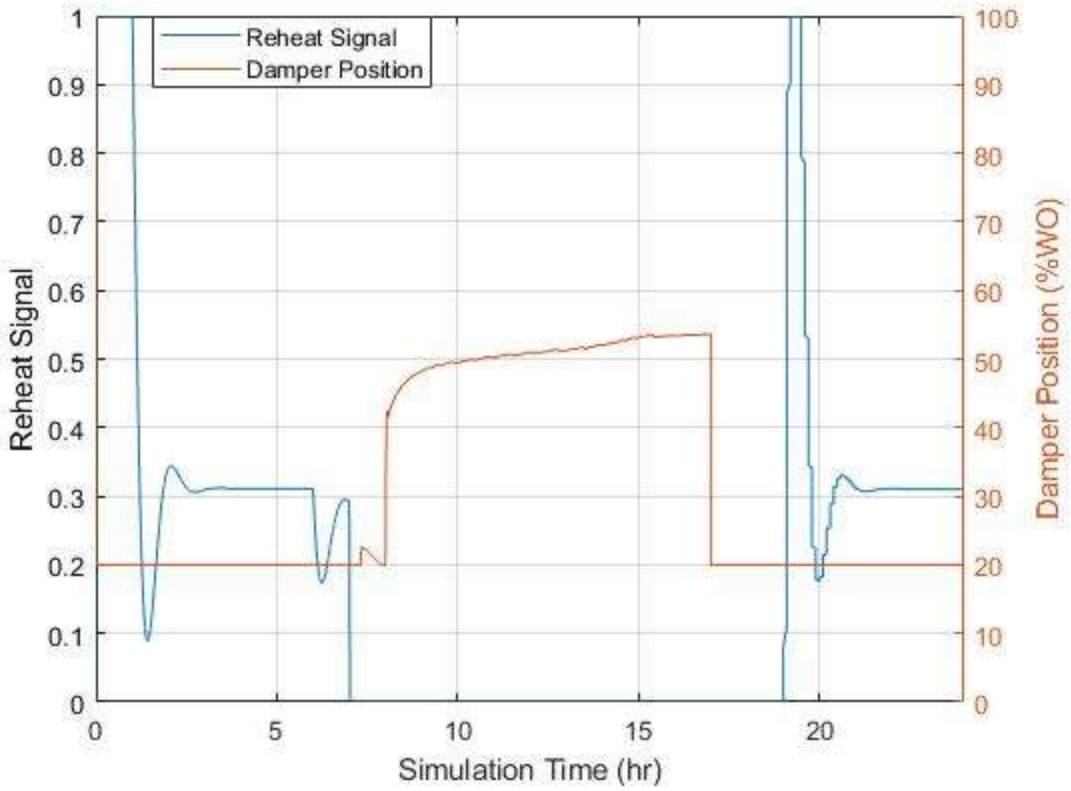

Figure 5. 2. 3: VAV controller response including damper position and reheat signal

Figure 5.2.3 shows that when the zone temperature is below the set point dead band in the early and late stages of the test, the damper is closed to its minimum position of 20 %WO. Additionally, the reheat signal comes on which energizes the reheat coil activation. In the middle portion of the simulated time period, the damper modulates the delivery of air flow into the zone as expected during cooling mode operation. The damper opens to a larger value as the zone temperature departs further the setpoint temperature. Since the zone temperature reaches the $T_{diff,high}$ criteria, the damper never fully opens. Overall, this test shows how the system behaves in a manner that is expected in a cooling scenario, including the use of reheat at low zone load conditions when the VAV box is at its minimum specified flow.

5.3 Fan Controller

The second controller is responsible for modulating the speed of the fan in the AHUs. This controller compares the static pressure in the duct to a setpoint pressure. If the measured duct static pressure is greater than the allowable dead band range the fan speed is decreased and if the duct pressure is below the setpoint then the fan speed will increase. This logic flow is presented in Figure 5.3.1.

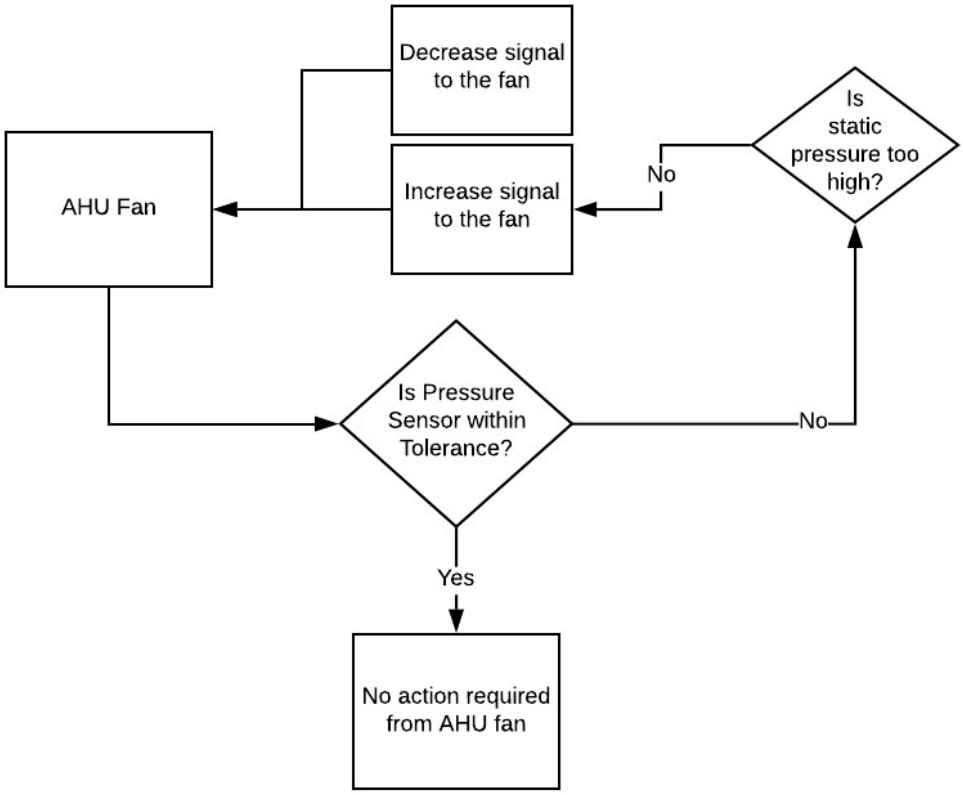

Figure 5. 3. 1: Fan controller logic flow chart

The controller requires parameters that specify the maximum and minimum operating RPM of the AHU fan ($f_{\max}, f_{\min}$). Additionally, the controller requires the setpoint pressure (P_{set}) as well as the measured pressure ($P_{measured}$) and fan speed (f_{in}). The TRNSYS component reads in the value of f from the previous timestep to enforce

constraints on the rate at which the fan speed can be changed by the controller. Next, the model establishes the difference in pressure between the measured value and the setpoint dead band:

$$P_{diff} = P_{measured} - \left(P_{set} + tol_p \right) \tag{5.3.1}$$

If P_{diff} is positive, the model uses Eq. (5.3.2) to determine how much the fan speed will change over the course of the timestep $\left(\frac{df}{dt} \right)$. Otherwise, Eq. (5.3.3) is used to determine $\frac{df}{dt}$.

$$\frac{df}{dt} = \begin{cases} -(df/dt)_{\max} & P_{diff} \geq 1 \text{ inH2O} \\ -0.75(df/dt)_{\max} & 1 \text{ inH2O} > P_{diff} \geq 0.5 \text{ inH2O} \\ -0.5(df/dt)_{\max} & 0.5 \text{ inH2O} > P_{diff} \geq 0.25 \text{ inH2O} \\ -0.25(df/dt)_{\max} & 0.25 \text{ inH2O} > P_{diff} \geq 0.15 \text{ inH2O} \\ 0 & 0.15 \text{ inH2O} > P_{diff} \geq 0 \text{ inH2O} \end{cases} \tag{5.3.2}$$

$$\frac{df}{dt} = \begin{cases} (df/dt)_{\max} & P_{diff} \leq -1 \text{ inH2O} \\ 0.75(df/dt)_{\max} & -1 \text{ inH2O} < P_{diff} \leq -0.5 \text{ inH2O} \\ 0.50(df/dt)_{\max} & -0.5 \text{ inH2O} < P_{diff} \leq -0.25 \text{ inH2O} \\ 0.25(df/dt)_{\max} & -0.25 \text{ inH2O} < P_{diff} \leq -0.15 \text{ inH2O} \\ 0 & -0.15 \text{ inH2O} < P_{diff} \leq 0 \text{ inH2O} \end{cases} \tag{5.3.3}$$

Where $(df/dt)_{\max}$ is a user established controller parameter that determines the maximum change in fan speed across a timestep. This method ensures that the fan speed will only adjust with a limited rate of change. Finally, the output value of f is calculated by the equation:

$$f = f_{in} + \frac{df}{dt}\tau \tag{5.3.4}$$

As seen in the tests performed in chapter 4, when the system resistance is increased (i.e. dampers are closed) at a constant fan speed, the pressure rise across the fan is increases. This shows that the driving mechanism to cause changes in static pressure is the actuation of the system dampers. As dampers are closed, the static pressure will increase. Figure 5.3.2a shows the actuation of the damper that occurs in Figure 5.2.3. Figure 5.3.2b highlights the effect this has on the pressure downstream of the AHU1 fan and the resulting control decisions made by the fan controller using parameters of $f_{\max} = 3600$ rpm, $f_{\min} = 1800$ rpm, $P_{set} = 2.5$ inH$_2$O, and $(df/dt)_{\max} = 0.5$ rpm/s.

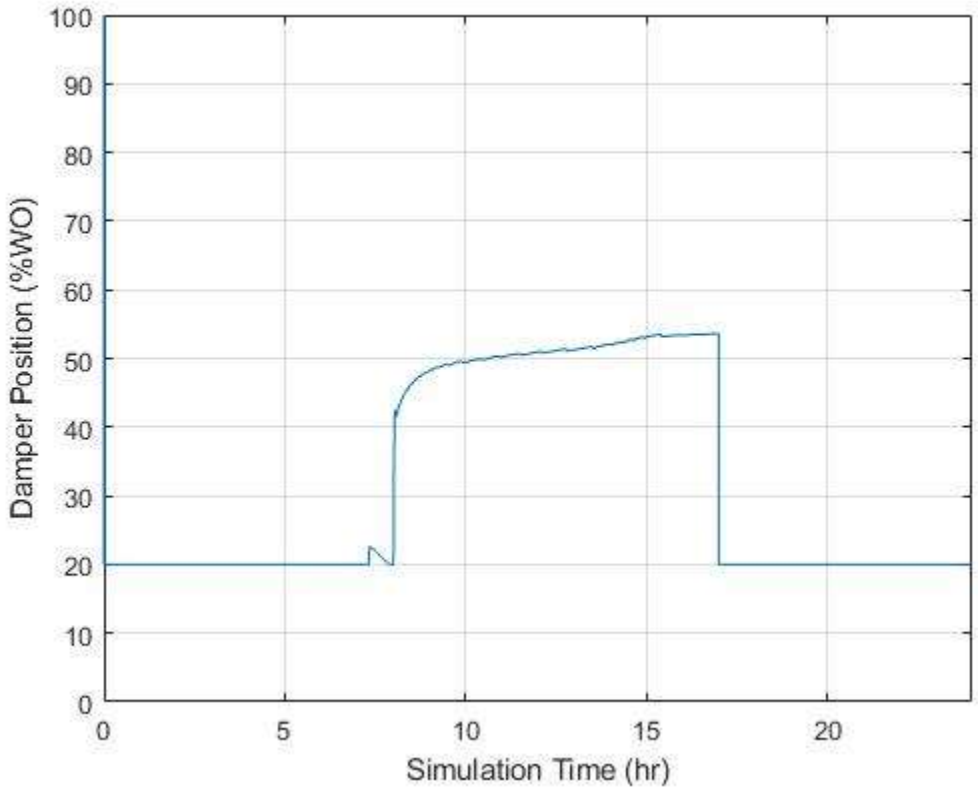

a)

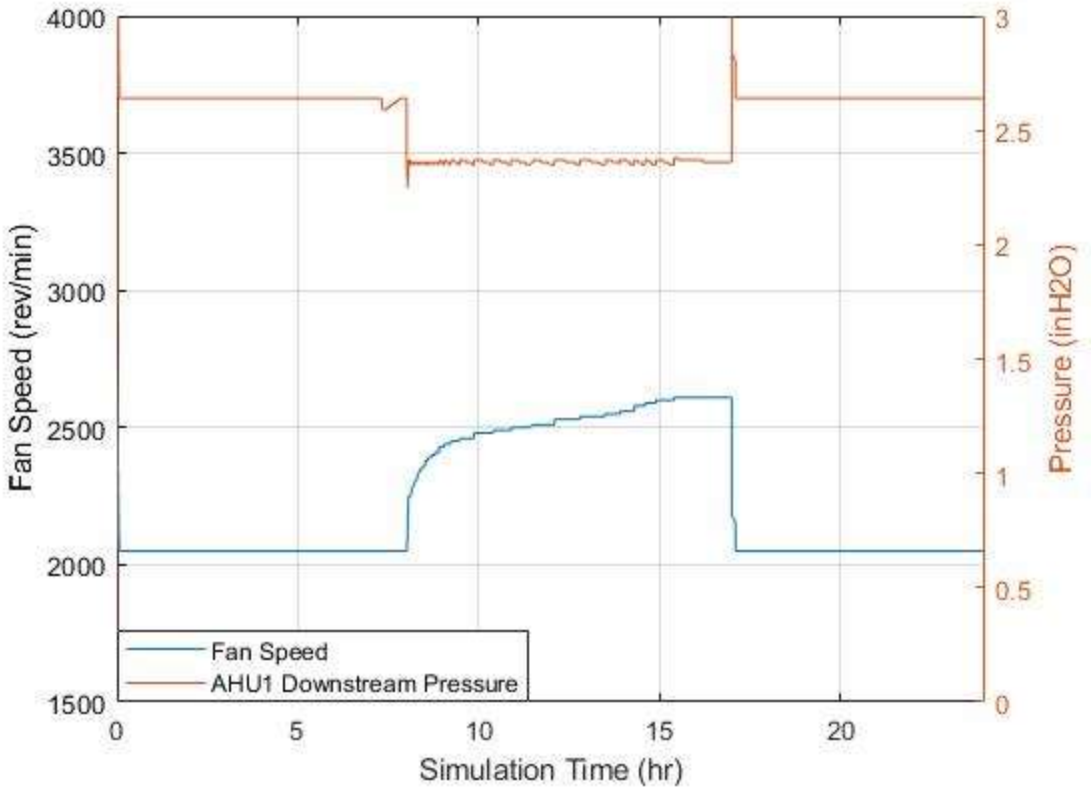

b)

Figure 5. 3. 2:a) Damper response b) AHU1 fan downstream pressure and resultant fan speed

The fan speed remains constant when the damper position is at its minimum value. As the damper opens in the middle portion of the test, the pressure within the system drops, causing the fan speed to increase, which provides a larger volume of cool air during the timeframe when the zone temperature is above the setpoint. Thus, the fan controller shows that it increases and decreased the fan speed based on the static pressure as determined by the actuation of the system dampers.

5.4 Cooling Coil Controller

The final controller is responsible for the adjustment of the amount of coolant that flow through the coiling coils in the AHUs to maintain the air leaving the cooling coil at the desired set temperature. Figure 5.4.1 depicts the logic flow that the controller uses.

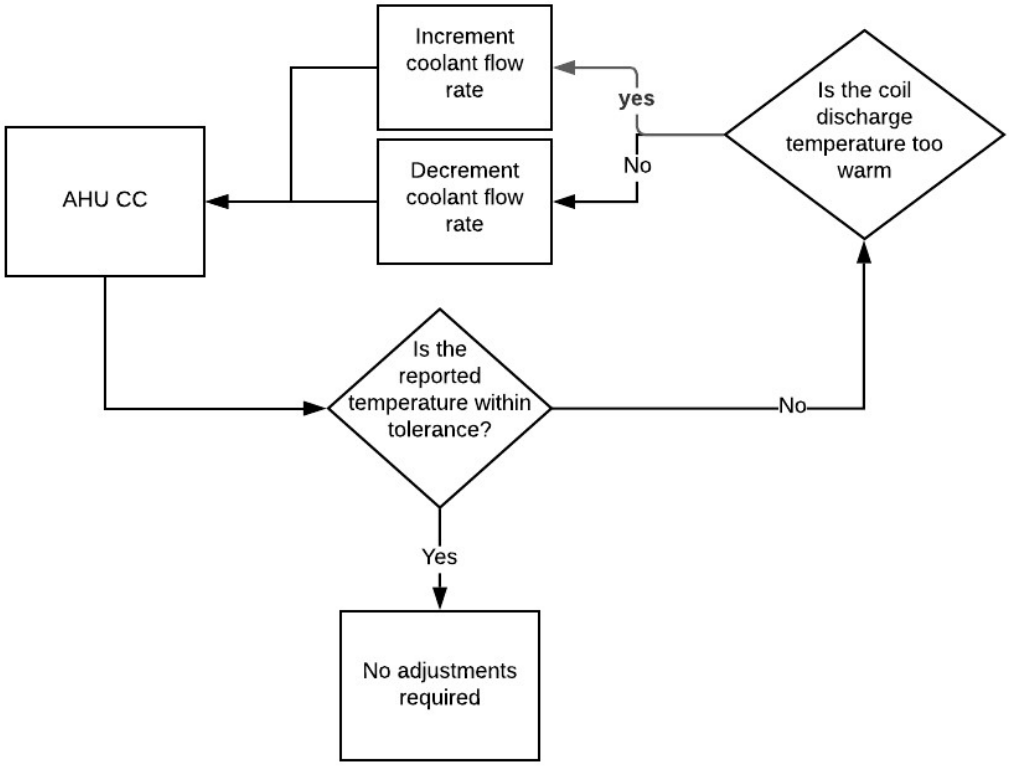

Figure 5. 4. 1: Cooling Coil Control Logic Flow

The cooling coil controller was designed in a similar fashion to the VAV controller. This controller uses parameters including the smallest allowable flow rate ($\dot{m}_{\min}$), the largest possible flow rate ($\dot{m}_{\max}$), and the temperature difference at which the largest mass flow rate is required ($T_{diff,high,cc}$). The model then uses inputs that include the air temperature leaving the cooling coil (T_a) along with the setpoint temperature of the air exiting the coil ($T_{set,cc}$). The controller logic starts by calculating the temperature difference compared to a dead band region surrounding the setpoint defined by:

$$T_{diff,cc} = T_a - (T_{set,cc} + tol_{cc}) \tag{5.4.1}$$

The component then checks to see if the temperature difference exceeds the upper limit defined by $T_{diff,high,cc}$ through the inequality:

$$T_{diff,cc} > T_{diff,high,cc} \tag{5.4.2}$$

If this inequality is true, then the output mass flow ($\dot{m}_{out}$) is set to $\dot{m}_{\max}$. Otherwise, a second inequality is used:

$$T_a \geq T_{set,cc} + tol \tag{5.4.3}$$

The purpose of Ineq. (5.4.3) is to determine if the air is warmer than the upper end of the allowable range given the setpoint. If this is true, the program uses slope-intercept form to calculate $\dot{m}_{out}$ as shown in Eqs. (5.4.4)-(5.4.6):

$$m_{cc} = \frac{T_{diff,high,cc} - T_{diff,low,cc}}{\dot{m}_{\max} - \dot{m}_{\min}} \tag{5.4.4}$$

$$b_{cc} = -m_{cc}\dot{m}_{\min} \tag{5.4.5}$$

$$\dot{m}_{out} = \frac{T_{diff,cc} - b_{cc}}{m_{cc}} \tag{5.4.6}$$

If Ineq. (5.4.3) is false then that means the temperature of the air is too cold relative to the setpoint. In that situation, $\dot{m}_{out}$ is set to $\dot{m}_{\min}$. The final step in the model is to ensure that the rate of change from the previous timestep is not too large. If this happens, then a limitation on the change is implemented that prevents the coolant from rapidly fluctuating.

To ensure that this component works operates correctly, the model was tested using the same conditions depicted in Figure 5.2.2. The temperature of the air exiting the cooling coil was prescribed and used to determine the mass flow of the coolant through the coil.

In this situation, the parameters were set to: $\dot{m}_{\min} = 200$ kg/hr, $\dot{m}_{\max} = 2000$ kg/hr, $T_{diff,high,cc} = 3$ °C, and $T_{set,cc} = 6$ °C. The response of the controller is depicted in Figure 5.4.2.

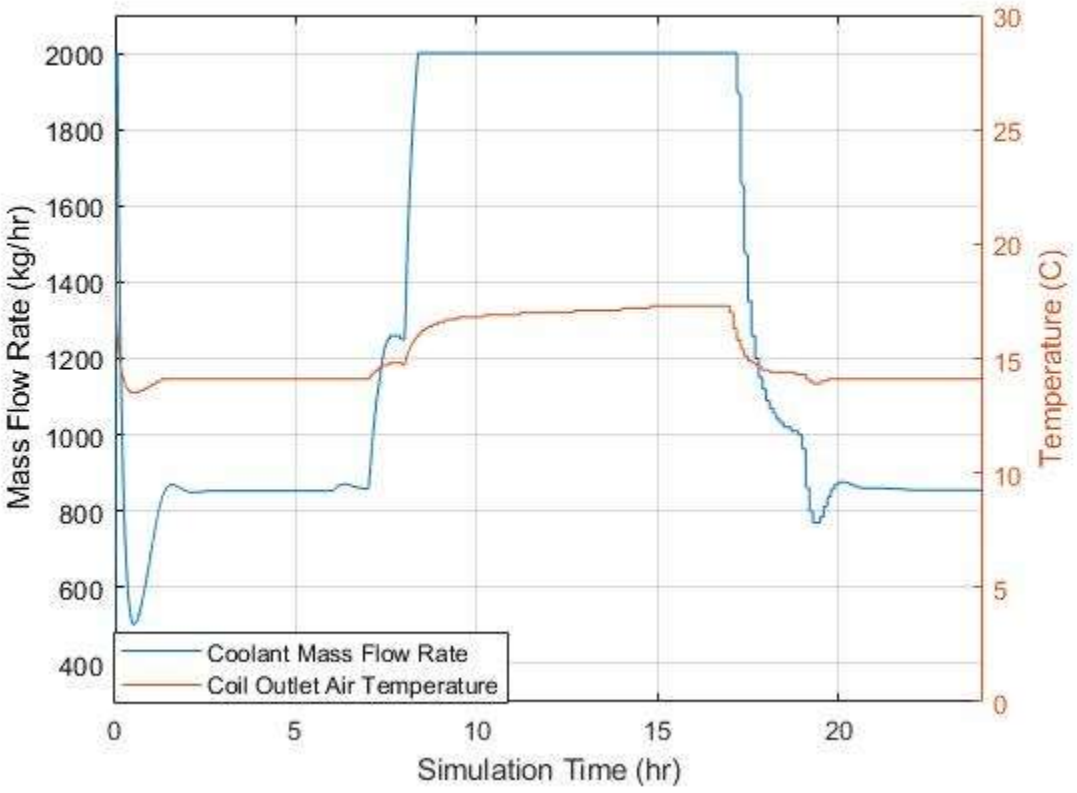

Figure 5. 4. 2: Cooling coil controller response

Over the first 8 hours and final 8 hours of the simulation, the mass flow through the coil is at its lowest values because cooling is not needed. In the middle of the simulation, the mass flow increases in response to the rising air temperature downstream of the coil as the AA temperature and the RA temperature from the zone increases.

5.5 Future Work

While all these controllers work to provide a method in which the model can make decisions and actuate changes to maintain the temperature of air within the zone based on

a variety of setpoints along with ensuring a minimum air flow rate, there are some limitations to these models. One of the major hinderances is the use of proportional controllers. There are several situations where the controllers have difficulty making control decisions that provide sufficient heating or cooling to the zones. An example of this is if the zone temperature is 2.5 °C above setpoint operating at the same parameters of *tol*, D_{low}, D_{high}, and $T_{diff,high}$ as shown in section 5.2. In this hypothetical scenario, the damper position will open to 44 %WO. While this may be enough action from the controller to bring prevent the zone from getting any warmer, the controller will not actuate further open to bring the zone back to setpoint. Even when the cooling coil is fully activated, the proportional nature of the damper controller often hinders the model from reaching the setpoint temperature. One workaround for this is to reduce *tol*. However, if this is done then there will be much more oscillation within some of the controllers, which can cause convergence errors. The better idea to solve this issue involves adapting each controller to replicate the controllers that are used at the IBAL. These initial baseline controllers are all proportional controllers, whereas the IBAL utilizes PI controllers. This will allow the controllers to reach their setpoints with smooth transient responses rather than instantaneously jumping to a new solution at each time step. In addition to simply improving each controller model, the implementation of the actual controllers used in the IBAL will allow NIST to test and develop control strategies in the model that can then be more easily adapted into the physical system.

5.6 Summary

Overall, three controllers were developed so that the aggregate model could operate autonomously. This consisted of controllers to make decisions regarding VAV damper

positions and reheat, fan speed, and coolant flow through the cooling coil. All the initial controllers were proportional controllers that were tested to ensure that they behaved properly. While this was sufficient for a baseline autonomous system, there is need for future work to improve the models so that the controllers become sufficiently complex to match the actual IBAL controllers.

CHAPTER VI

Ease of Use Developments

6.1 Introduction

The previous sections described the creation of the individual models that are used to simulate the IBAL. However, these sections do not cover some of the work that was done to enable the simulation user to adjust tunable parameters as needed to reflect future changes in the IBAL itself. The two developments that were carried out to simplify the user experience are the creation of a standard data format and an automatic signal generator. The standardized data format creates a baseline format for input data which reduces the potential for error when tuning models. The signal generator creates a signal that allows TRNOPT to understand what data should be included in the tuning process.

6.2 Standardized Data Format

To ensure that the heating coil models (preheat and reheat), and cooling coil model can be easily used by researchers at NIST, a standardized form of each component was created. TRNSYS data readers are limited to reading in up to 99 data columns. As the data from the IBAL includes information from almost 300 sensors, it is important to ensure that the IBAL data collected for subsequent input into the TRNSYS model is organized in a consistent manner that prevents confusion between components while adhering to the 99-column limit. Previously, there had been no consistency for how the data was organized between each component model; there was a different layout for the preheat coil model, the cooling coil model, and the reheat coil model. The standardized

input layout is shown in Table 6.2.1 and is consistent across all component models that require data.

Table 6.2.1 List of input positions in optimized layout

Input	1	2	3	4	5	6	7	8	9
	T_{AA}	RH_{AA}	F_{AA}	T_{RA}	RH_{RA}	F_{RA}	$T_{hc,in}$	$RH_{hc,in}$	$T_{hc,out}$
Input	10	11	12	13	14	15	16	17	18
	$\dot{q}_h$	$T_{coolant,in}$	$T_{coolant,out}$	$T_{cc,out}$	$\dot{m}_{coolant}$	$T_{ahu,out}$	$RH_{ahu,out}$	F_{VAV}	$\dot{q}_{VAV}$
Input	19	20	21	22	23	24	25	26	27
	$T_{VAV,out}$	F_{speed}	$\dot{q}_{fan}$	$D6$	$D5$	$D17$	$D18$	$D10$	F_{exf}

The data format was updated so that inputs corresponding to the supply air and return air branches occupy the first six inputs. Inputs 7-10 now correspond with the conditions surrounding the preheat coil. Inputs 11-14 correspond to the conditions of the Air Handling Unit (AHU) cooling coil. Inputs 15-19 are linked to the VAV box conditions. The last set of inputs that are currently in place pertain to the damper positions within the system along with the AHU fan inputs and the exfiltration air flow; these occupy inputs 20-27. As further components are developed requiring additional data, this information can also be integrated into this standardized format (up to 99 inputs).

6.3 Componential Parameter Tuning Tool

6.3.a Tuning Overview

The TRNSYS optimization routine, TRNOPT, is used for tuning parameters for a given component which allows TRNSYS to “calibrate” individual component model’s

parameters to match experimental data. To operate TRNOPT, an error term is defined and integrated over a corresponding data time period to obtain an average error. This error is typically defined as the difference between the measured data and the simulated data. The user then prescribes the parameters that TRNOPT can adjust or tune to reduce the overall error throughout the entirety of the data set being tested. An issue that can arise involves determining those parameters that reflect the steady state performance (such as overall heat transfer coefficient and bypass fraction) at the same time as those that affect the transient response, e.g. thermal capacitance. Figure 6.3.1 presents the temperature rise across a VAV reheat coil along with the power input to the coil with varying air flow rate.

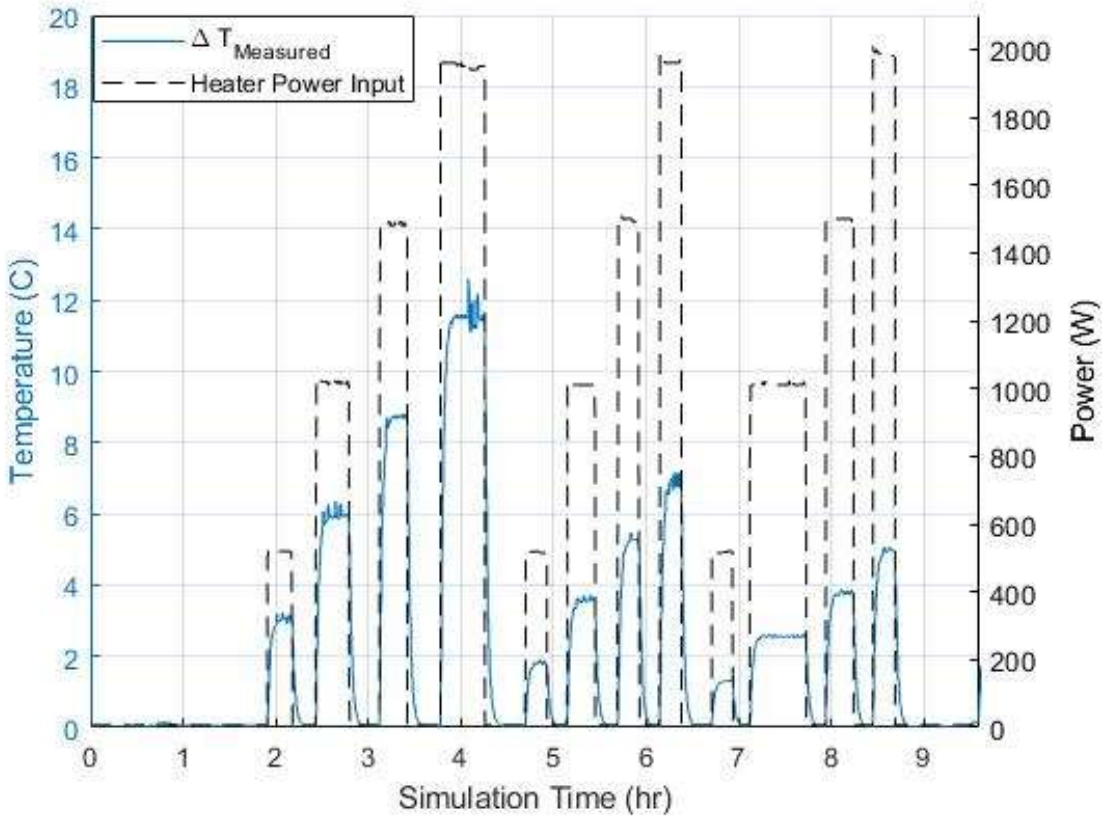

Figure 6. 3. 1: Example of typical data set used in tuning

By inspection, every time the power is changed, there is a short transient period and then the model reaches steady state until the power is adjusted again. This highlights the fact that in most test cases, there are significantly more data points for steady state behavior than there are for transient behavior. Since TRNOPT weights all data equally, this resulted in a greater emphasis on parameters being adjusted to match the steady state behavior while typically neglecting or de-emphasizing a good match to the transient behavior.

A workaround to this issue involved implementing user-defined forcing functions to direct TRNOPT to only optimize or tune model parameters focused on data during the transient periods. During periods of steady state, the output of this function would be '0', which indicates that the error term that TRNOPT wants to reduce is ignored. During transient periods, the function outputs '1' which directs TRNOPT to include the error in the optimization. In Figure 6.3.1 there are 12 different steady state periods of data. Since there is a transient state as the coil energizes and another as the coil de-energizes, the number of transient states is double the number of steady state periods of data. For the scenario presented in Figure 6.3.1, there are 24 transient periods of data to use for tuning. The number of points of that need to be generated to fully-define a forcing function that accounts for each interval is calculated by multiplying the total number of periods being analyzed and multiplying by 4. This value ('4') is used because that is the minimum number of points to define a forcing function that will characterize each section where power is activated and deactivated. Taking this number and adding two to account for the start and end points of the function yields the total number of points required in the forcing function. For Figure 6.3.1, this would require a total of 98 points to do a transient-

based tuning. To further show how this process is accomplished, Figure 6.3.2 provides a simplified example of this for a scenario where there is only one period of steady state behavior (2.2767 < Time < 2.5703), and thus for a transient analysis 2 periods of data are to be examined (from 2.2083-2.2767 and 2.5703-2.6528). To define all these periods of time while only weighting the transient states, there are ten points in the associated table that are used to define the entirety of the function, with eight of the points being associated with defining the beginning and end of the transient periods and two points for the beginning (0,0) and end (5.675,0) of the function.

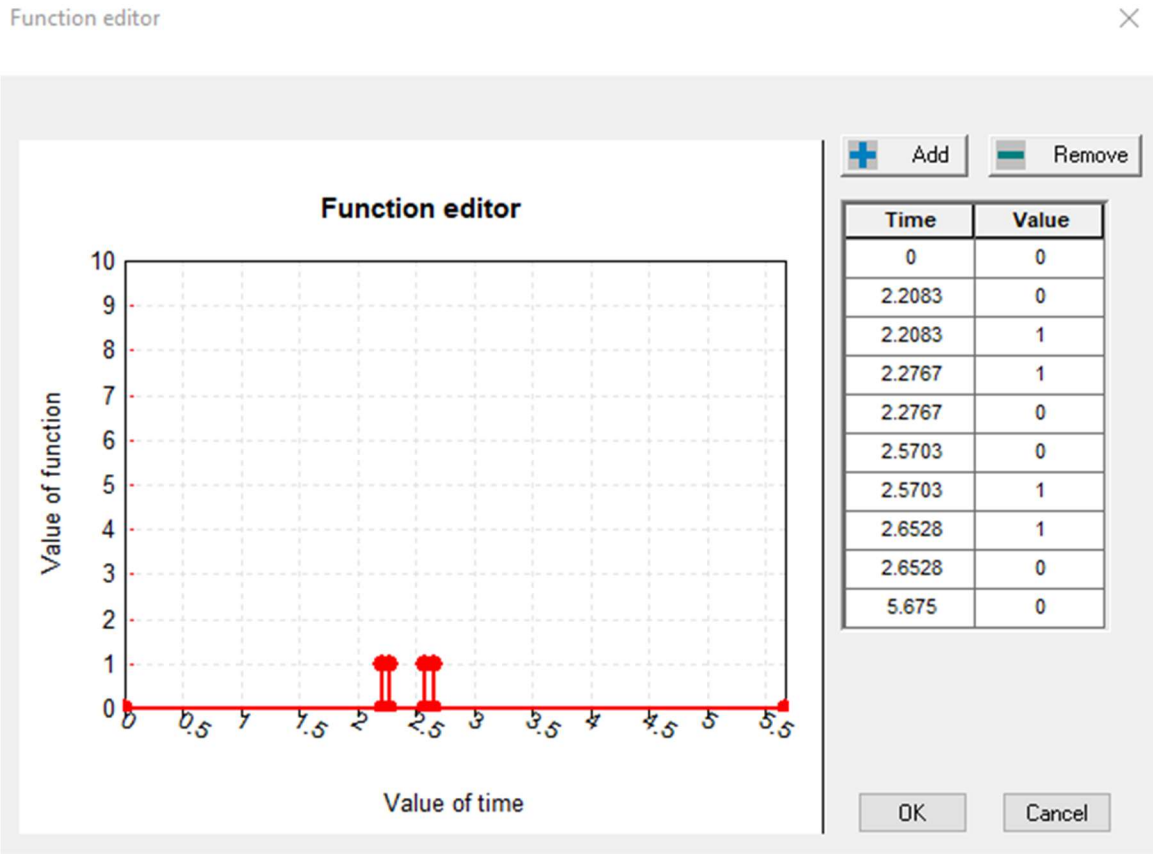

Figure 6. 3. 2: Example of the forcing function editor

After tuning to data over the entirety of data to obtain the steady state parameters, the optimized value for conductance would be provided as an input. Then the optimization would be performed again, this time using only the transient periods of data to determine

the capacitance that best allows the model to reflect the transient behavior. Using this process for the VAV heater scenario presented in Figure 6.3.1, the values for capacitance (C) and the conductance (UA) yields $1.2875\ \frac{\text{kJ}}{\text{K}}$ and $48.125\ \frac{\text{kJ}}{\text{hr K}}$, respectively. These are the parameters that were reported in section 2.4.c and thus the results of the model compared to the data for the manual optimization process are shown in Figure 2.4.6

To simplify and streamline the model parameter tuning process, a tool was created within TRNSYS to automatically generate the optimization signal based upon defined criteria. There are currently 3 different modes for the tool, these are particularly tailored towards tuning the heating coils. Each mode corresponds to a different purpose and use. In total, there are 5 parameters and inputs that may need to be specified for TRNOPT's optimization signal tool to work. These are: the mode, the maximum value of change in temperature for which the model will generate an off signal (val_{max}), the minimum difference criteria that can activate an 'on' signal ($diff_{min}$), the moving average of the temperature over a 12 timestep period which is used to operate the signal (avg), along with the actual temperature value at the current timestep (val). To ensure clarity, $diff_{min}$ is used to prevent small spikes in average temperature change between time steps from generating a false positive and activating the tuning signal. Additionally, val_{max} guarantees that the tuning signal is deactivated when the temperature change across the coil is miniscule.

6.3.b Mode 1

Mode 1 is designed to include both the transient states and the steady state behavior but only while the component is operational; it will exclude all the data during which there is no substantial temperature rise (as defined by the user input of val_{max}) across the coil. The

model begins by reading in the inputs and parameters for the current time step. Additionally, the model reads in values from the previous time step. These include the on/off tuning signal, moving average, and actual value. A term to define the current difference of the moving average was then made:

$$diff_{avg} = avg - avg_{last} \tag{6.3.1}$$

Where avg is the moving average including current time step and avg_{last} is the moving average up to the previous time step. The model then checks to see if the signal was activated in the previous time step. If the signal is off, then the following inequality examined:

$$\left|diff_{avg}\right| \geq diff_{\min} \tag{6.3.2}$$

If Ineq. (6.3.2) is true, then the signal is activated. If false, no change is made and the signal remains turned off. If the signal from the previous time step is on, then the signal will remain on until:

$$\left|val\right| \leq val_{\max} \tag{6.3.3}$$

Figure 6.3.3 depicts *avg* along with $diff_{avg}$ that corresponds with the data set from Figure 6.3.1. For use in the signal generator, the user inputs are $val_{\max} = 0.3$ °C and $diff_{\min} = 0.09$ °C. The user input for $diff_{min}$ is important in deciding how well the component ignores differences caused by noise in the data that may activate the signal.

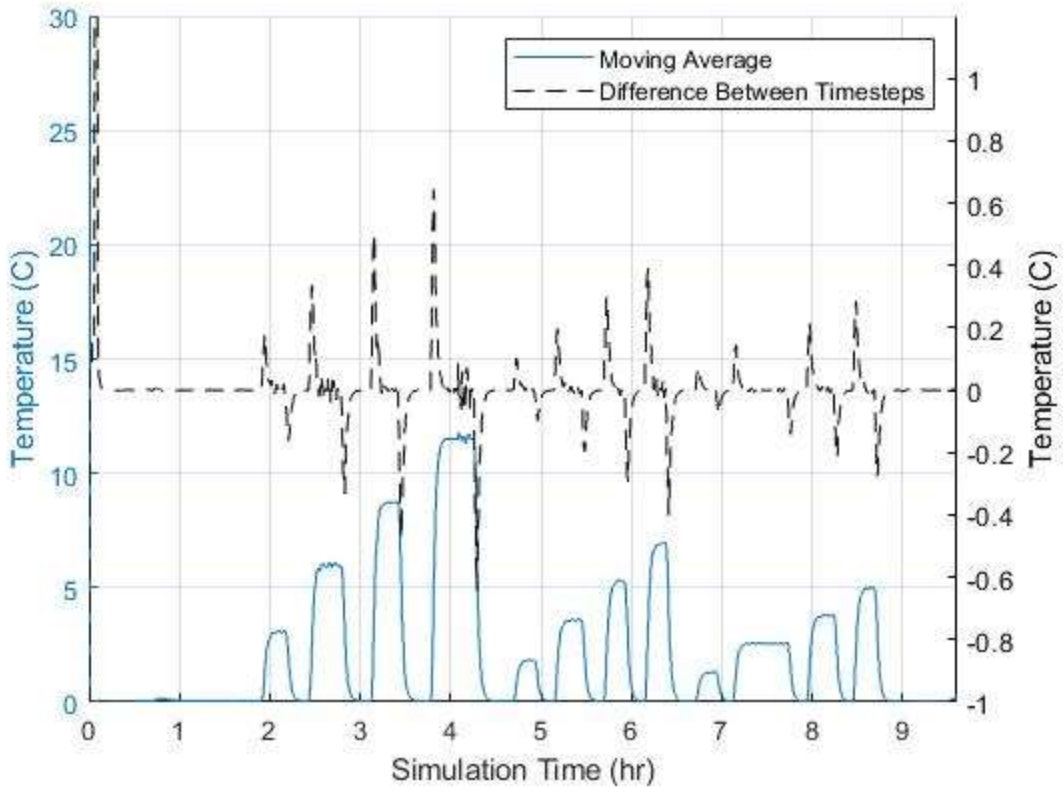

Figure 6. 3. 3: Moving average and its difference from the previous time step

Figure 6.3.4 depicts the result of mode 1 in terms of the actual signal that is generated based on the temperature rise from the measured data.

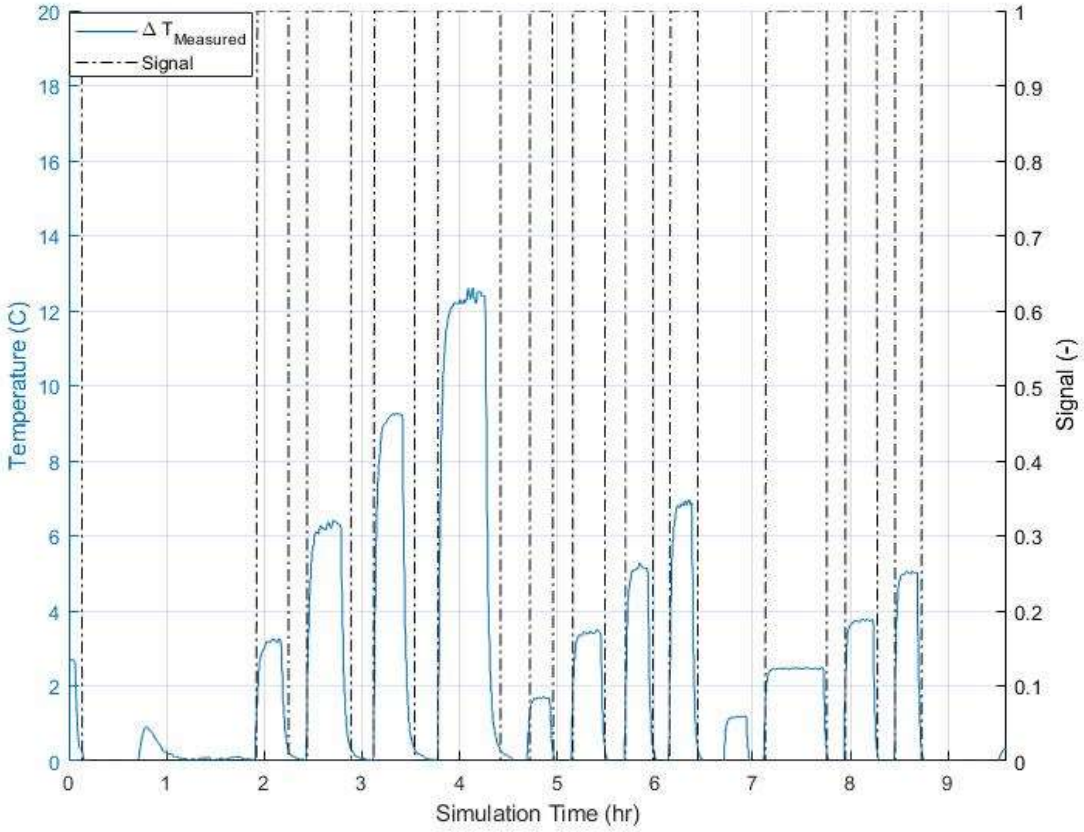

Figure 6. 3. 4: Mode 1 optimization signal

As expected, the signal activates over the periods of interest and de-activates when the temperature rise across the coil is very small. One period of steady state data is neglected due to its derivative being of the same magnitude as the noise that is being filtered out. When this mode is used in the optimization tool the resulting values of C and UA are $0.1094 \ \frac{\text{kJ}}{\text{K}}$ and $10.5 \ \frac{\text{kJ}}{\text{hr K}}$, respectively. The result of running the model using these estimated parameters is shown in figure 6.3.5.

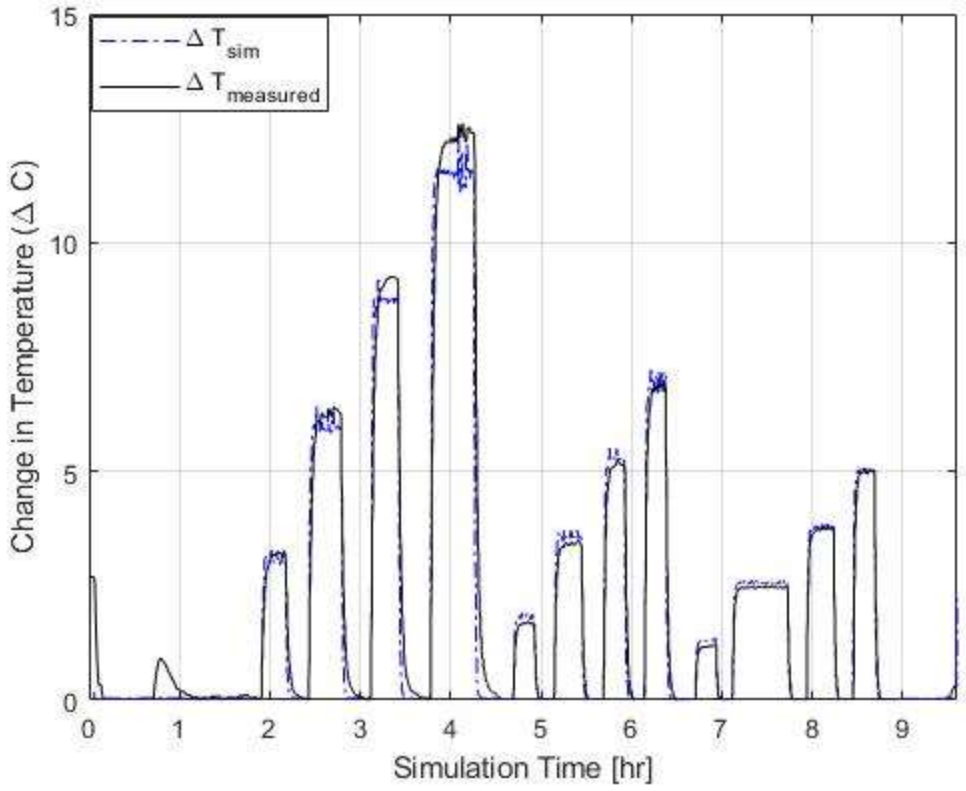

Figure 6. 3. 5: Mode 1 optimization result

As the optimization results in a small capacitance, the simulation is, essentially, performing a steady state energy balance on each timestep. This is clearly seen as the transient behavior of the measured data is not replicated well because the steady state data is over-emphasized. Thus, this mode is useful if the model capacitance has already been tuned and only the overall heat transfer coefficient needs to be tuned. To limit the need for separate runs to tune the capacitance and the overall heat transfer coefficient, mode 2 was created.

6.3.c Mode 2

Mode 2 differs from mode 1 in a few crucial ways. Under ideal circumstances, TRNOPT can be run one time with this mode and the tool will reach the optimal model parameters. Mode 1 adjusts the weight associated with the calculated error depending on whether the

system is operating in a transient or steady manner. This forces TRNOPT to tune in a balanced manner to account for the transient data and steady data more equally. This is accomplished by the incorporation of an exponentially decaying function that is high at the beginning of a transient event and then decays towards zero as the system approaches steady state. All the inputs are the same as mode 1 apart from one additional parameter that specifies the time constant of exponential function (τ_c) used for this purpose. Ideally, this time constant will be approximately equal to the half of the number of time steps required for the coil to reach steady state after it is energized. As the decaying function does not activate until steady state behavior begins, it is important to ensure that the function decays quickly as it will start at a high value initially. If the decay does not occur quickly, the steady state data may not be balanced properly in the tuning process.

Mode 2 begins under the assumption that the initial signal is off and proceeds with Eqs. (6.3.1)-(6.3.2). If Ineq. (6.3.2) is true, then the signal is activated and the counter is set to 0. If the inequality is false, then the signal remains off. If the signal is activated, then an alternate branch of logic is followed. It begins by checking Ineq. (6.3.3). If this statement is true, then the signal and counter are set to '0'. Otherwise, the following inequality is analyzed:

$$\left|diff_{avg}\right| < diff_{\min} \tag{6.3.4}$$

If Ineq. (6.3.4) is true, based on the previous criteria, then the data is in the steady state period. Thus, the counter is incremented by one and the signal is generated according to the following equation:

$$sig = 0.1 + 0.9e^{-counter/\tau_c} \tag{6.3.5}$$

As the model continues in the steady state period, *counter* will increase. This causes the signal to decay as *counter* increases relative to τ_c. This reduces the weight of the steady state periods allowing the model to balance between both states. If Ineq. (6.3.4) is false then the data must be in a transient state and the signal is set to '1'. Finally, at the end of the mode, Ineq. (6.3.3) is used to ensure that the signal is deactivated if the value of the current timestep is below the user defined number.

The result of this is a signal that is depicted by figure 6.3.6.

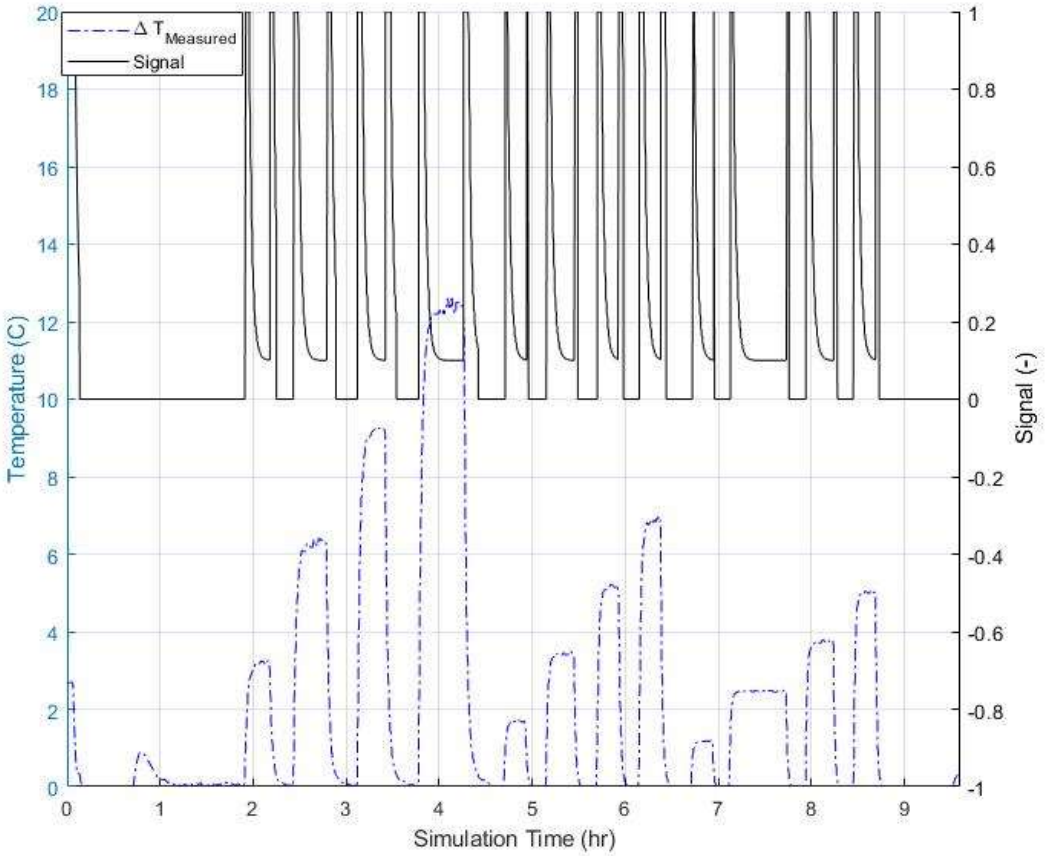

Figure 6. 3. 6: Mode 2 optimization signal

The behavior of the control signal shows how it is deactivated during periods where there is no temperature rise across the coil. During the transient states, the signal is at its

maximum value which then decays as it moves into the steady state periods of data. Using this mode, the TRNOPT optimmization found C and UA values that closely match those determined from the manual optimization ($C = 1.2875$ kJ/K and $UA = 48.125$ kJ/hr-K). Thus, the model vs data result would be identical to the results shown in Figure 2.4.6.

6.3.d Mode 3

Mode 3 was created to complement mode 1 for use in situations where mode 2 is not sufficient. This mode generates a signal to only optimize over transient periods of data. This is useful for finding the capacitance of the model. At the first time step, the code for this mode begins under the assumption that the signal is off. When the signal is off at the start of a time step, a series of inequalities are analyzed.

The code first checks to see if Ineq. (6.3.2) is satisfied. If true, it means the signal is activated as this indicates the beginning of the transient period. If the inequality fails, then the signal remains off as the model has not reached a transient state yet.

For time steps where the signal is previously on, the criteria for turning off the signal is based upon the following inequality:

$$\left|diff_{avg}\right| < \frac{diff_{\min}}{3} \tag{6.3.6}$$

The value of $diff_{min}$ is divided by three to capture more of the transient state. Without using a reduced value, the later portions of the transient states are disregarded by the model. An additional parameter may be added to future iterations of this mode which would allow the user to specify this number instead of arbitrarily reducing it. If Ineq.

(6.3.6) is true then the signal is de-activated. Otherwise, the signal remains on until the time step where this criterion is met.

The resulting signal that is generated by mode 3 is shown in figure 6.3.7.

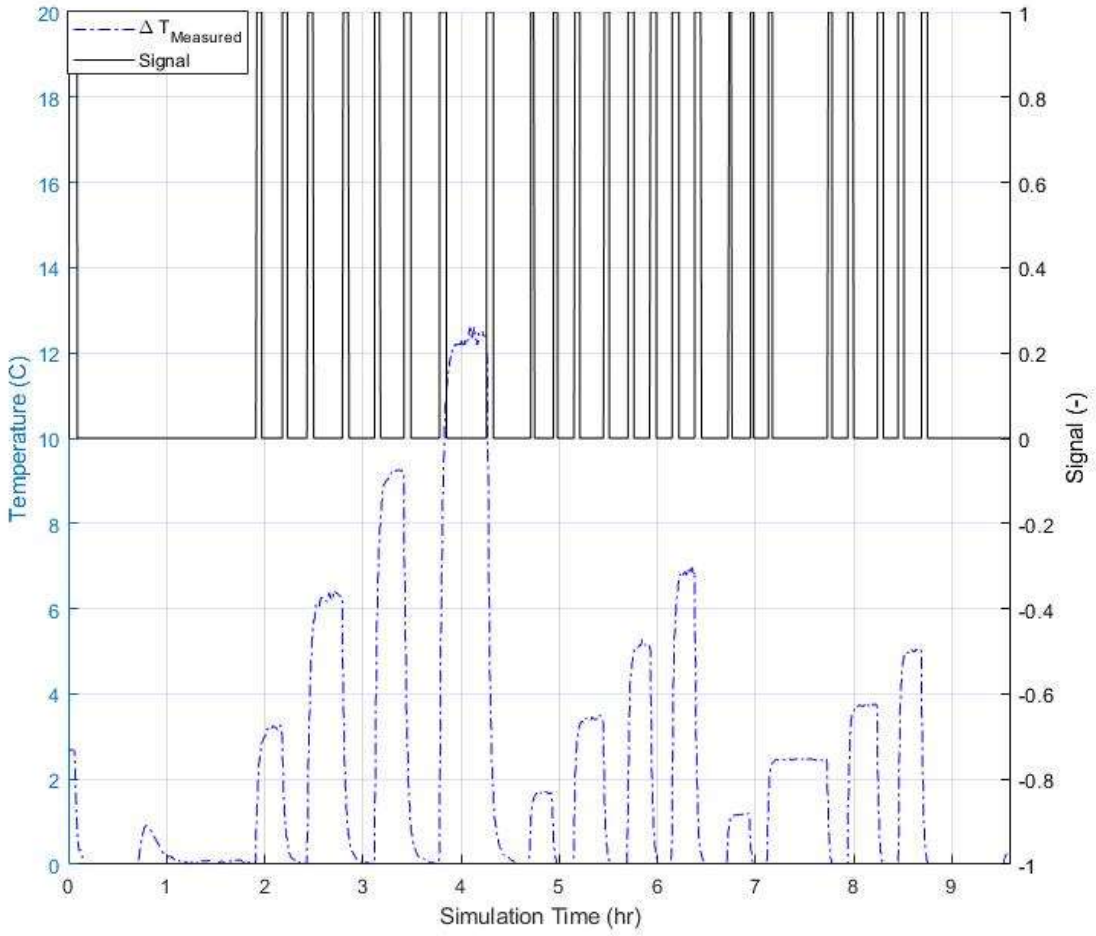

Figure 6. 3. 7: Mode 3 optimization signal

When TRNOPT operates under mode 3, the model determines the optimized values of C and UA to be 1.2875 kJ/K and 49.5 kJ/hr-K which is remarkably similar to the manually run and mode 2 values.

6.4 Summary

Overall, there were a few developments to mitigate potential for errors in the process of tuning components. The first improvement involved creating a standardized data format. This allows for the organization of data that is used in tuning that is more consistent than individualized formats for each component. The other major improvement from a user standpoint is the creation of a tool to determine the periods over which TRNOPT performs its tuning. In summary, mode 2 is designed to be the simplest solution to tuning parameters. Under tested conditions, this mode allowed for a simplified tuning process without requiring manually implemented forcing functions. If this mode does not achieve satisfactory results, a user can use mode 3 to find the optimal *UA* value for any model, and then run mode 1 at this fixed *UA* to find *C*. The process can be repeated if necessary. This replicates the manual process that a user would undergo without the tedious nature of defining the forcing functions.

Chapter VII

Summary and Future Work

7.1 Summary

Overall, several models and components have been designed with the end goal of creating a user-friendly simulation of the NIST IBAL. To accomplish this, heat exchanger models were developed and validated to simulate the transient performance for the preheat coil, the reheat coil, and the cooling coil. Both heating coils were shown to operate within 1°C of measured data from the with airflow ranges (1800 kg/hr-3000 kg/hr for preheat and 600 kg/hr-1500 kg/hr for reheat) at all operational powers for each heater. The model experienced the greatest difference from measured data at conditions that corresponded to high input power coincident with low airflow rates. In terms of the cooling coil, the model again operates within 1°C of measured data during typical operational flow rates. This conclusion was determined at coolant flow rates above 1000 kg/hr and airflow around 1800 kg/hr. During periods of low coolant flow, the model's predicted outlet temperatures deviate, particularly on the coolant side. An energy balance using the measurements from the IBAL showed that the uncertainty of the coolant mass flow instrumentation may be a predominant factor in the energy imbalance.

The next model that was developed was an airflow and pressure calculator. This was accomplished by using manufacturer fan and damper curves. However, these proved to ineffective at capturing the actual behavior of the IBAL. To refine the model's predictive capability, measured data from the IBAL that included airflow and static pressure were

collected for all the fan and damper components to generate in-situ performance curves. While the measured fan curves were a proven improvement in comparison to the manufacturer curve, the damper data was less consistent, resulting in curves that resulted in modest improvement.

Additionally, controllers were implemented to allow the aggregate model to operate independent of human inputs. Three controllers were developed to generate this base control strategy. The first controller was responsible for proportionally adjusting a damper based on a temperature difference relative to the controller setpoint temperature. The model also creates a reheat signal if heating is required during minimum zone airflow. The second controller changes the fan speed of the AHU fan based on the pressure difference relative to the controller setpoint pressure. As pressure decreases, an increase in fan speed is commanded and visa-versa. The final controller adjusts the mass flow of coolant through the cooling coil based on a temperature difference of the air leaving the cooling coil relative to the controller setpoint.

The final additions to the model include the standardization of data to be used in component tuning. This reduces the chance for human error when tuning components. The other addition is a component that generates as signal that effectively selects what data to use in the tuning process. Tests have shown that this component performs equally as well in tuning models relative to the time-consuming manual process.

7.2 Future Work

In addition to what has already been completed, there is plenty of work that can be accomplished to further improve the TRNSYS simulation of the IBAL. Regarding the component models, the heating coil may be improved by implementing a *UA* that is dependent on heater power or by adding a heat loss term to account for the heat loss

within the IBAL. Future work on the cooling coil includes the potential for additional testing at other low flow scenarios. Examples of this includes testing to determine the coil behavior when the AHU is experiences low airflow. Additionally, due to the results of the energy balance performed in section 3.6, work could be done to lessen the uncertainty within the measurements. Ensuring that the measurements balance energy is a crucial aspect towards tuning the model. An additional tunable parameter that could potentially address this issue is the addition of a heat loss term. If the IBAL sensor uncertainty is examined and there is still an imbalance of energy within the measurements, a calculated heat loss term could address that issue.

In addition, the model will benefit from more validation of the pressure/airflow component. Observing the totality of measured data from the IBAL, the pressure differentials across the fans are consistent relative to the airflow. However, as there are no dedicated pressure sensors across the dampers, the fan pressure sensors were used in conjunction with temporary pitot tubes to establish the damper performance. As the results from this process were mixed, more measured data that consistently depicts the performance for some of these dampers would benefit the model greatly. Once all the damper curves have been adjusted, then the aggregate model can be compared directly with the IBAL data based on the inputs of the fan speed and the damper positions.

A third aspect that can be improved is the controllers that were developed. While the controllers function properly according to their design (proportional controllers), these do not reflect the logic used within the IBAL. To remedy this, work has already begun beyond the scope of this project to implement the IBAL logic within TRNSYS controllers. Once completed, this can be implemented within the aggregate model to

better simulate the response that occurs within the IBAL. This is important as these controllers will be the backbone for the future research that NIST is interested in exploring.

APPENDIX A: Descriptions of Coil Tests Used in Tuning

Listed below are the names of each test used in the tuning of the various coil models, including a brief overview of the what the inputs were for each test.

A1: AHU1 Heating Coil Tests

2019_12_11_run1: Fan speed varies from 30 Hz-60 Hz, AHU1 heater power increments from 0-5 kW. 3872 time steps of useful data.

2019_10_09_run1: Fan speed is constant at 30 Hz, varying heater power from 0-10 kW. Heater cuts out at upper end of heater input during the test. 1404 time steps of useful data

2019_09_30_run1: Fan speed is constant at 60 Hz, varying heater power from 0-7kW. Heater cuts out halfway through the test. 500 time steps of useful data

2019_09_30_run2: Fan speed is constant at 60 Hz, varying heater power from 0-10 kW. 1450 time steps of useful data.

2019_10_01_run1: Fan speed held constant at 45 Hz, varying heater power from 0-10 kW. 2043 time steps of useful data.

Dynamic Tests: Fan speed held constant at 45 Hz, varying heater power from 0-4 kW. 1000 time steps of useful data.

2019_10_21_run1: Fan speed varies from 30 Hz-60 Hz, varying heater power from 0-3 kW. 1900 time steps of useful data.

A2: VAV4 Heating Coil Test

2020_10_13_run1: AHU1 fan speed held constant at 60 Hz. Damper 18 incremented between 40 %WO-100 %WO to generate three different flow rates across the reheat coil. Varying heater power from 0-1.5 kW. 3460 time steps of useful data.

A3: AHU1 Cooling Coil Tests

2020_10_19_run1: Inlet air temperature relatively constant at 29 °C, inlet coolant temperature held relatively constant at 8 °C in nominal flow configuration. Inlet airflow held constant around 1750 kg/hr. Coolant flow is varied between 2000 kg/hr-500 kg/hr. 3500 time steps of useful data.

2019_11_18_run1: Inlet air temperature varies between 20 °C-24 °C, inlet coolant temperature held relatively constant at 10 °C in nominal flow configuration. Inlet airflow held constant around 2000 kg/hr. Coolant flow is varied between 1500 kg/hr-350 kg/hr. 1685 time steps of useful data.

APPENDIX B: Propylene-Glycol Specific Heat Table

Propylene-Glycol 30% Specific Heat Table

1..21	1 T [C]	2 cp [kJ/kg-K]
Run 1	0	3.803
Run 2	1	3.805
Run 3	2	3.808
Run 4	3	3.811
Run 5	4	3.814
Run 6	5	3.816
Run 7	6	3.819
Run 8	7	3.822
Run 9	8	3.824
Run 10	9	3.827
Run 11	10	3.83
Run 12	11	3.833
Run 13	12	3.835
Run 14	13	3.838
Run 15	14	3.841
Run 16	15	3.843
Run 17	16	3.846
Run 18	17	3.849
Run 19	18	3.852
Run 20	19	3.854
Run 21	20	3.857

APPENDIX C: META DATA SAMPLE

This meta data sample depicts how the uncertainty of each instrument was determined.

measuren	card	physical_c	channel_r	measuren	signal_typ	subsysten	instrumer	instrumer	calibratio	accuracy_	unit_raw	unit_scale
ahu_dp	6345	PXI2Slot8/	531	Differenti	AI	Secondary	PX2300-25	0	0	0	V	psi
ahu1_cc_c	4357	PXI1Slot1	124	Temperat	RTD	AHU1	RAF185L28	NA	3/2/2020	0.197755	F	F
ahu1_cc_r	4357	PXI1Slot9/	75	Temperat	RTD	AHU1	Mamac TE	NA	########	0.201042	F	F
ahu1_f_cc	6238	PXI1Slot1	197	Flow	AI	AHU1	DTFXL2-JN	100714	########	0.23	mA	gpm
ahu1_f_ra	6363	PXI2Slot3/	325	Flow	AI	AHU1	Ebtron GT	708439	NA	NA	V	cfm
ahu1_f_sa	6363	PXI2Slot3/	326	Flow	AI	AHU1	Ebtron GT	707957	NA	NA	V	cfm
ahu1_fan_	4300	PXI1Slot7/	59	Power	AI	AHU1	AGW-006E	14090238	NA	2.47	V	W
ahu1_hea	6704	PXI2Slot6/	397	Control	AO	AHU1	NA	NA	NA	NA	V	V
ahu1_hea	4300	PXI1Slot7/	61	Power	AI	AHU1	AGW-006E	15040368;	NA	2.47	V	W
ahu1_hea	4357	PXI1Slot9/	74	Temperat	RTD	AHU1	Mamac TE	NA	########	0.199267	F	F
ahu1_in_r	4357	PXI1Slot9/	73	Temperat	RTD	AHU1	Mamac TE	NA	########	0.198462	F	F
ahu1_on	6363	PXI2Slot5/	395bw	Control	DO	AHU1	NA	NA	NA	NA	V	V
ahu1_out_	4357	PXI1Slot9/	76	Temperat	RTD	AHU1	Mamac TE	NA	########	0.197461	F	F
ahu1_p_d	4300	PXI1Slot2/	5	Pressure	AI	AHU1	Mamac PR	NA	########	0.007614	V	inH2O
ahu1_p_u	4300	PXI1Slot2/	4	Pressure	AI	AHU1	Mamac PR	NA	########	0.003122	V	inH2O
ahu1_rh_c	4300	PXI1Slot2/	6	Humidity	AI	AHU1	ACI A/RH2	NA	########	0.72	V	%
ahu1_rh_r	6345	PXI2Slot8/	527	Humidity	AI	OAU	HMD62	R2340291	########	0.16	V	%
ahu1_rh_s	6345	PXI2Slot8/	525	Humidity	AI	OAU	HMD62	R2340290	########	0.3	V	%
ahu1_rh_u	4300	PXI1Slot2/	3	Humidity	AI	AHU1	ACI A/RH2	NA	########	1.28	V	%
ahu1_t_ra	6363	PXI2Slot3/	325T	Temperat	AI	AHU1	Ebtron GT	708439	NA	NA	V	F
ahu1_t_sa	6363	PXI2Slot3/	326T	Temperat	AI	AHU1	Ebtron GT	707957	NA	NA	V	F
ahu1_tdb_	6345	PXI2Slot8/	528	Temperat	AI	OAU	HMD62	R2340291	########	0.06	V	F
ahu1_tdb_	6345	PXI2Slot8/	526	Temperat	AI	OAU	HMD62	R2340290	########	0.16	V	F
ahu1_vfd	6704	PXI2Slot7/	450	Control	AO	AHU1	NA	NA	NA	NA	Hz	V
ahu2_cc_c	4357	PXI1Slot1	125	Temperat	RTD	AHU2	RAF185L28	NA	3/2/2020	0.198281	F	F
ahu2_cc_r	4357	PXI1Slot9/	79	Temperat	RTD	AHU2	Mamac TE	NA	########	0.199869	F	F
ahu2_f_cc	6238	PXI1Slot1	198	Flow	AI	AHU2	DTFXL2-JN	100713	########	0.26	mA	gpm
ahu2_f_ra	6363	PXI2Slot3/	334	Flow	AI	AHU2	Ebtron GT	708382	NA	NA	V	fpm
ahu2_f_sa	6363	PXI2Slot3/	327	Flow	AI	AHU2	Ebtron GT	708329	NA	NA	V	cfm
ahu2_fan_	4300	PXI1Slot7/	60	Power	AI	AHU2	AGW-006E	14090246	NA	2.47	V	W
ahu2_hea	6704	PXI2Slot6/	405	Control	AO	AHU2	NA	NA	NA	NA	V	V
ahu2_hea	4300	PXI1Slot7/	62	Power	AI	AHU2	AGW-006E	15040369;	NA	2.47	V	W
ahu2_hea	4357	PXI1Slot9/	78	Temperat	RTD	AHU2	Mamac TE	NA	########	0.197786	F	F
ahu2_in_r	4357	PXI1Slot9/	77	Temperat	RTD	AHU2	Mamac TE	NA	########	0.199046	F	F
ahu2_on	6363	PXI2Slot5/	395gw	Control	DO	AHU2	NA	NA	NA	NA	V	V
ahu2_out_	4357	PXI1Slot9/	80	Temperat	RTD	AHU2	Mamac TE	NA	########	0.197847	F	F
ahu2_p_d	4300	PXI1Slot2/	9	Pressure	AI	AHU2	Mamac PR	NA	########	0.012183	V	inH2O
ahu2_p_u	4300	PXI1Slot2/	8	Pressure	AI	AHU2	Mamac PR	NA	########	0.003114	V	inH2O
ahu2_rh_c	4300	PXI1Slot2/	10	Humidity	AI	AHU2	ACI A/RH2	NA	########	0.89	V	%
ahu2_rh_r	6345	PXI2Slot8/	529	Humidity	AI	OAU	HMD62	R2340288	########	0.14	V	%
ahu2_rh_u	4300	PXI1Slot2/	7	Humidity	AI	AHU2	ACI A/RH2	NA	########	1.12	V	%
ahu2_t_ra	6363	PXI2Slot3/	334T	Temperat	AI	AHU2	Ebtron GT	708382	NA	NA	V	fpm
ahu2_t_sa	6363	PXI2Slot3/	327T	Temperat	AI	AHU2	Ebtron GT	708329	NA	NA	V	F
ahu2_tdb_	6345	PXI2Slot8/	530	Temperat	AI	OAU	HMD62	R2340288	########	0.03	V	F
ahu2_vfd	6704	PXI2Slot7/	451	Control	AO	AHU2	NA	NA	NA	NA	Hz	V
ch1_c_out	4357	PXI1Slot1	158	Temperat	RTD	Chiller1	RAF185L28	NA	3/4/2020	0.198217	F	F
ch1_e_in_	4357	PXI1Slot1	121	Temperat	RTD	Chiller1	RAF185L28	NA	########	0.208552	F	F
ch1_e_out	4357	PXI1Slot1	122	Temperat	RTD	Chiller1	RAF185L28	NA	########	0.196874	F	F
ch1_f_c	6238	PXI1Slot1	194	Flow	AI	Chiller1	DTFXL2-KN	100716	########	0.54	mA	gpm
ch1_f_e	6238	PXI1Slot1	193	Flow	AI	Chiller1	DTFXL2-KN	100718	########	0.6	mA	gpm
ch1_on	6704	PXI2Slot6/	442	Control	DO	Chiller1	0	0	0	0	V	V
ch1_powe	4300	PXI1Slot6/	52	Power	AI	Chiller1	AGW-006E	15040371;	NA	0.00247	V	W

REFERENCES

Energy Information Administration. (2020). *U.S. energy flow, 2020*. [Online]. Available: https://www.eia.gov/totalenergy/data/flow-graphs/total-energy.php. [Accessed 08-July-2021]

Energy Information Administration. (2020). *What is the United States' share of world energy consumption*. [Online]. Available: https://www.eia.gov/tools/faqs. [Accessed 10-July 2021]

GovTrack.us. (2021). S. 1298 — 117th Congress: Clean Energy for America Act. Retrieved from https://www.govtrack.us/congress/bills/117/s1298

National Renewable Energy Laboratory. (2009). *Advancing Net-Zero Energy Commercial Buildings*. [Online]. Available: https://www.nrel.gov/docs/fy10osti/46313.pdf. [Accessed 10-July 2021]

Pertzborn, A. J. (2016). *Intelligent Building Agents Laboratory: Hydronic System Design* (NIST Technical Note 1933). National Institute of Standards and Technology.

Kelly, G. & Bushby, S. (2012). Are intelligent agents the key to optimizing building HVAC system performance? *HVAC R Res*., *18*(4), 750–759.

Pertzborn, A. J. & Veronica D. A. (2018). *Intelligent Building Agents Laboratory: Air System Design* (NIST Technical Note 2025). National Institute of Standards and Technology.

NIST IBAL data obtained from Amanda Pertzborn, personal communication (2021)

Stanke, D. (2000). Dehumidify with Constant-Volume Systems: It May Take More than You Think. *Trane Engineers Newsletter*, *29*(4), 4-5.

Klein, S.A. et al. (2020). *EES*(v10.833). WI Solar Energy Laboratory, University of Wisconsin.

Trane. (2014). *Submittal Data, Air Handling Units#1 & #2, 237313 1-14*. 37.